# Galaxy Formation and Evolution:
## the Local Galaxy Population as a Cosmological Probe

Dissertation der Fakultät für Physik
der
Ludwig-Maximilians-Universität München

vorgelegt von Darren J. Croton
aus Melbourne, Australia

Datum der mündlichen Prüfung: 3. November 2005

1. Gutachter:   Prof. Dr. Simon D. M. White
2. Gutachter:   Prof. Dr. Andreas Burkert

# Contents

# Summary

We take a multi-faceted approach to study galaxy populations in the local universe, using the completed *Two Degree Field Galaxy Redshift Survey* (2dFGRS), the "Millennium Run" $\Lambda$CDM N-body simulation, and a semi-analytic model of galaxy formation. Our investigation covers both small and large scale aspects of the galaxy distribution. This work can be broken into three sections, outlined below.

Using the 2dFGRS we explore the higher-order clustering properties of local galaxies to quantify both (i) the linear and non-linear bias of the distribution relative to the underlying matter field, and (ii) the nature of hierarchical scaling in the clustering moments of the galaxy distribution. This last point is the expected signature of an initially Gaussian distribution of matter density fluctuations that evolved under the action of gravitational instability. We show in Chapters 2, 3, and 4 that the 2dFGRS higher-order clustering moments are indeed hierarchical, which we measure up to sixth order for galaxies brighter than $M_{b_J} - 5 \log_{10} h = -17$ and which sample the survey volume out to $z \approx 0.3$. The moments are found to be well described by the negative binomial probability distribution function, and we rule out, at high significance, other models of galaxy clustering, such as the lognormal distribution. This result holds in redshift space on all scales where we obtain a good statistical signal, typically $0.5 < R \, (h^{-1}\mathrm{Mpc}) < 30$ (i.e. from strongly non-linear to quasi-linear regimes). Interestingly, we find that the moments on larger scales can be significantly altered by two massive superclusters present in the 2dFGRS. The skewness of the galaxy distribution is found to have a weak dependence on galaxy luminosity. We show that a simple linear biasing model provides an inadequate description of the higher order results, suggesting that non-linear biasing is present in the clustering moments of the 2dFGRS.

The large-scale distribution of structure within the 2dFGRS allows us to study the properties of the galaxy population as a function of local environment. In Chapter 5 we measure the luminosity function of early and late-types galaxies in survey regions ranging from sparse voids to dense clusters to reveal the dominant population in each. Fitting each luminosity function with a Schechter function allows us to quantify how the bright and faint populations transform with changing density contrast. We find that (i) the population in voids is dominated by late types, with a noticeable deficit of intermediate and bright galaxies relative to the mean, and (ii) cluster regions have an excess of very bright early-type galaxies relative to the mean. When directly comparing faint early and late type galaxies in void and cluster regions, the cluster population shows comparable abundances of both types, whereas in voids the late types dominate by almost an order of magnitude. Of interest to many galaxy formation models is our measurement that reveals that the faint-end

slope of the overall luminosity function depends at most weakly on density environment.

Finally, in Chapter 6, we develop a self-consistent model of galaxy formation and couple this to the Millennium Run $\Lambda$CDM N-body simulation. This simulation represents a significant step forward in both size and resolution, allowing us to follow the the complete evolutionary histories of approximately 20 million galaxies down to luminosities as faint as the Small Magellanic Cloud in a volume comparable to that sampled by the 2dFGRS. In our galaxy formation model we supplement previous treatments of the growth and activity of central black holes with a new model for 'radio' feedback from those active galactic nuclei that lie at the centre of a quasistatic X-ray emitting atmosphere in a galaxy group or cluster. With this we can simultaneously explain (i) the low observed mass drop-out rate in cooling flows, (ii) the exponential cut-off at the bright end of the galaxy luminosity function, and (iii) the fact that the most massive galaxies tend to be bulge-dominated systems in clusters and contain systematically older stars than lower mass galaxies. This success occurs because static hot atmospheres form only in the most massive structures, and radio feedback (in contrast, for example, to supernova or starburst feedback) can suppress further cooling and thus star formation without itself requiring star formation. Matching galaxy formation models with such observations has previously proved quite challenging.

2

# 1 Introduction

## 1.1 Motivation

Much of my work as a PhD student has centred on an attempt to understand two important aspects of the nature of galaxies in the local universe. The first considers a *larger scale* perspective of the galaxy population: (i) How are galaxies distributed across the billions of light years that we currently observe? (ii) How do these galaxies reflect the underlying dark matter density field? (iii) What does this tell us about the initial conditions of the universe, before all the structure that we currently see came into being? On the other hand, the second aspect of interest can be considered, by comparison, a rather *small scale* perspective of the galaxy population: (i) Can we explain the rich diversity of individual galaxies and galaxy associations seen in the local universe? (ii) Are there key aspects to our understanding of galaxy formation and evolution that we are missing? (iii) How important is the environment around a galaxy in determining its final properties, the so called nature or nurture question. This thesis represents a culmination from the past three years of my work on these problems. Perhaps not surprisingly, with such a broad range of questions to be investigated, this research remains ongoing and includes numerous collaborations, both locally and internationally. Extensions beyond this thesis are discussed in the final chapter.

Any study of the large scale structure of the galaxy distribution and the evolution of galaxy populations inside this distribution must begin with an understanding of the interplay between matter and gravity. Below I provide a brief overview of basic cosmology theory and the equations which govern it. The evidence for dark matter is presented along with its place in the larger scheme of structure formation. I give a short introduction to galaxy clustering and bias, followed by a discussion of the Two Degree Field Galaxy Redshift Survey and a basic overview of the state of current models of galaxy formation. Finally, I finish with a outline of the scientific objectives of each chapter in this thesis.

## 1.2 Essential cosmology

On large enough scales, the universe appears to be statistically homogeneous and isotropic. In reality, this means that the universe does not possess any privileged positions or directions. The idea of homogeneity and isotropy is fundamental and forms a basic axiom of cosmology known as the Cosmological Principle. It is supported by much observational evidence (e.g. Smoot et al. 1977), and has been the focus of much study and philosophical interpretation over the last 80 or so years.

The strongest force by far in the universe on large scales is gravity, and any study of large scale behaviour must begin with an understanding of it. To formalise the mathematical theory of gravity, one is required to introduce the concept of a space-time interval between two events, $ds$, and look for stationary values of $\int ds$, which correspond to the shortest distance between any two points being a straight line. This space-time interval defines the metric, and in general relativity it describes the space-time geometry in which particles naturally move.

The most general space-time metric describing a universe in which the cosmological principal is obeyed is the Robertson-Walker metric (Coles & Lucchin 1995):

$$ds^2 = c^2dt^2 - a(t)^2\left[\frac{dr^2}{1-kr^2} + r^2(d\theta^2 + sin^2\theta\, d\phi^2)\right], \tag{1.1}$$

where we have used standard spherical polar coordinates r, $\theta$, $\phi$ (all co-moving), $t$ is the proper-time, $a(t)$ is the cosmic scale factor, and the constant $k$ is the curvature parameter, which can be scaled to only take on the values -1, 0 or 1. This metric defines a metric tensor, $g_{ij}$, with which the Robertson-Walker metric takes the form:

$$ds^2 = g_{ij}dx^idx^j, \tag{1.2}$$

where the Einstein summation convention is implied.

Having the Robertson-Walker metric tensor allows us to use general relativity to obtain equations for the time evolution of the scale factor $a(t)$. The basic Einstein field equations of general relativity are differential equations which relate the geometry of space-time (the metric) to the distribution of energy and momentum within it (the source terms for gravity). These equations can be written as:

$$R_{ij} - \frac{1}{2}Rg_{ij} = -\frac{8\pi G}{c^2}T_{ij} - \Lambda g_{ij}, \tag{1.3}$$

where $T_{ij}$ is the total energy-momentum tensor, $R_{ij}$ is the Ricci tensor (a function of the metric $g_{ij}$), $R = R_{ii}$ is a measure if the curvature of space-time, and $\Lambda$ is Einstein's famous cosmological constant, which has become very important in recent years. If the Robertson-Walker metric tensor is substituted into the Einstein field equations, along with $T_{ij} = diag(\rho, -p, -p, -p)$ assuming the simplest case of a perfect fluid, one obtains the following equations for the time evolution of the scale factor $a$:

$$\frac{\ddot{a}}{a} = -\frac{4\pi G}{3}\left(\rho + \frac{3p}{c^2}\right) + \frac{\Lambda}{3}, \tag{1.4}$$

$$\left(\frac{\dot{a}}{a}\right)^2 = \frac{8\pi G}{3}\rho + \frac{\Lambda}{3} - \frac{k}{a^2}. \tag{1.5}$$

These are the famous Friedmann equations. If, for the moment, we assume no cosmological constant ($\Lambda = 0$), and using $H = \dot{a}/a$ (the Hubble parameter) and $\Omega_{tot} = \rho/\rho_{crit}$ (the

density parameter) where $\rho_{\text{crit}} = 3H^2/8\pi G$ (the critical density), the second Friedmann equation can be recast as:

$$\frac{k}{H^2 a^2} = \Omega_{\text{tot}} - 1 \ . \tag{1.6}$$

In this form, it is easy to see that, since $H^2 a^2$ is always greater than zero, there is a correspondence between the sign of the curvature parameter $k$ and the sign of $\Omega_{\text{tot}} - 1$. If $k$ equals 1, the density of the universe must exceed the critical density, and its ultimate fate is for gravity to win and for it to collapse back in on itself. On the other hand, if $k$ equals $-1$, the density must be less than critical, and then the expansion must win. The case of $k = 0$ corresponds to an equilibrium between gravity and expansion, implying that the geometry of the universe is flat.

In this way, we see that the energy density of the universe describes its underlying geometry, which in turn has a direct effect on its ultimate fate: expand forever in a big freeze or collapse back in on itself in a big crunch. The cosmological constant, $\Lambda$, adds an extra element that decelerates or accelerates the expansion, depending on its sign. Current observations suggest that the universe is flat. We will discuss this and the effects of the cosmological constant shortly.

## 1.3 The "dark" universe

Given the importance of $\Omega_{\text{tot}}$ in understanding the global nature and ultimate fate of the universe, it is only natural that its accurate measurement is high on the priority list of astronomers. Numerous methods have been developed to do this, and their conclusions were as interesting as they were profound. We summarise a few of these below, and refer the reader to Longair (1998) and Peebles (1980) for a more detailed account.

Possibly the simplest way to determine $\Omega_{\text{tot}}$ comes from calculating the mean mass density of galaxies in the universe, $\rho_{\text{gal}}$:

$$\rho_{\text{gal}} = \mathcal{L}_{\rho_{\text{gal}}} \left\langle \frac{M}{L} \right\rangle , \tag{1.7}$$

where $\mathcal{L}_{\rho_{\text{gal}}}$ is the mean luminosity density of galaxies, and $< M/L >$ is the mean galaxy mass-to-light ratio. A value of $\mathcal{L}_{\rho_{\text{gal}}}$ is obtainable from the galaxy luminosity function, while $< M/L >$ can be determined directly from the rotation curves of spiral galaxies. From $\Omega_{\text{gal}} = \rho_{\text{gal}}/\rho_{\text{crit}}$, the result follows. Putting these measurements together, one finds that $\Omega_{\text{gal}} \approx 0.01 - 0.03$ for varying galaxy samples, which is a very low result if we have any reason to expect a critical density universe.

A second method to determine $\Omega_{\text{tot}}$ utilises observations of galaxy clusters. To measure the mass of a galaxy cluster, one firstly requires the velocity dispersion $\langle \sigma^2 \rangle$ of the galaxies within the cluster. If we assume that the cluster is gravitationally bound, then the mass of the cluster follows from the cosmic virial theorem:

$$2KE + PE = \frac{3}{2} \langle \sigma^2 \rangle M_{\text{vir}} - \frac{GM_{\text{vir}}}{R_{\text{vir}}} = 0 \ . \tag{1.8}$$

An estimate of $\rho_{\mathrm{vir}}$, and hence $\Omega_{\mathrm{vir}}$, can thus be obtained by simply summing the masses of a number of large clusters within some set distance. By this technique, the value of the density parameter is found to be $\Omega_{\mathrm{vir}} \approx 0.1 - 0.3$, an order of magnitude higher than $\Omega_{\mathrm{gal}}$, but still 3 to 10 times smaller than what is required for a flat universe.

Adding up the luminous matter in galaxies and balancing the energy equation for clusters are not the only indicators of a discrepancy in our accounting of the mass content of the universe. Strong evidence came in the late 1970's when the rotation curves of spiral galaxies were accurately measured (e.g. Freeman 1970) for the first time. Interestingly, it was found that at large radii from the galactic centre the rotational velocity seemed to flatten, and by the measurement of gas surrounding the galaxy at radio wavelengths, this rotational flattening extendeds to greater radii than the visible mass of the galaxy. This is in contrast to the simplified expected Keplerian behaviour of the visible component, for which the velocity decreases as the inverse square root of the radius. Such rotation curve measurements indicate that virtually all spiral galaxies have a dark, diffuse halo associated with them that contributes at least 3 to 10 times the mass of the visible matter (Kormendy 1982). This conclusion is in line with that found by measuring the mass content of clusters.

Two interesting conclusions follow from these results. First, it indicates that there is a large dark component dominating cluster and galaxy masses. Understanding the nature of this "dark matter" has spawned a whole new subfield of cosmology. Second, by the fact that we're still a long way short of $\Omega_{\mathrm{tot}} \approx 1$, either the above measurements suggest that much more mass is hidden somewhere else in the universe away from groups and clusters, up to 10 times more, or it hints at the existence of a cosmological constant which acts such that the sum of $\Omega_{\mathrm{m}} + \Omega_{\Lambda} \approx 1$. There is much theoretical motivation (e.g. inflation), as well as detailed CMB observations (Spergel et al. 2003) and supernovae distance measurements (Riess et al. 1998), which all indicate that the universe is very nearly flat. This suggests that some form of "dark energy," in addition to the dark matter, is required in order to fit the measured properties of the observable universe.

The theory for cold dark matter was worked out in response to these problems, and more generally to understand structure formation in the universe. The standard model for cold dark matter (CDM) typically includes: a cosmological component of dark matter with negligible thermal velocity, a scale free power spectrum of initial adiabatic density fluctuations, and a dark energy or cosmological constant component, chosen so as to make $\Omega_{\mathrm{tot}} \simeq 1$. According to our current best observations, $\Omega_{\mathrm{tot}}$ can be broken up as $\Omega_{\mathrm{m}} \simeq 0.25$ and $\Omega_{\Lambda} \simeq 0.75$ (Spergel et al. 2003; Seljak et al. 2004). $\Lambda$CDM appears to be in agreement with the available data on large scales, but issues have arisen on smaller scales, such as the centres of dark matter halos (Flores & Primack 1994) and the number of small satellites (Kauffmann et al. 1993) . The solution to these problems appears to lie in a greater understanding of the non-linear galaxy-scale physics. Despite such issues, however, as a basis for a cosmological model, CDM has survived the last 20 years or so surprisingly well, given its simplicity. Thus, an investigation into the density distribution of matter within the universe has lead to a much greater understanding of its contents, global properties, and initial and final states.

## 1.4 Large scale structure, galaxy clustering and bias

Given the above standard model of cosmology, one can investigate the effects of gravitational instability and the evolution of large scale structure in the universe. This is achieved by tracing the time evolution of the initial matter density perturbation field, $\delta_I(x)$. Under the influence of its own gravity, an initial Gaussian density field will evolve into a strongly non-Gaussian one, resulting in a rich diversity of form that is characteristic of a highly evolved distribution of matter. In the favoured $\Lambda$CDM scenario discussed above, the formation of structure is expected to proceed hierarchically from the initial density perturbations, with galaxies forming first and larger structures following later from the merging of galaxies. The most striking feature revealed in all large-scale galaxy redshift surveys has been the way that galaxies are typically distributed along sheets and filaments, with empty voids between them. These structures have been seen to be as large as 50 to 100 Mpc. Understanding how such structures came to be is one of the primary goals of modern cosmology.

The observed structure in the universe can be characterised by the clustering moments of the distribution of density fluctuations, $\delta(x)$. Here we model the spatial distribution of galaxies as realizations of statistically homogeneous and isotropic random point processes. The 2-point correlation function, or second moment of the distribution, $\xi_2(R)$, is defined by the conditional probability of finding a galaxy in the volume element $dV$ at a distance $R$ from a galaxy, beyond that expected for a Poisson distribution (Peebles 1993):

$$dP = \bar{N} \left[ 1 + \xi_2(R) \right] dV , \tag{1.9}$$

where $\bar{N}$ is the mean density of galaxies. The 2-point correlation function can also be understood as the Fourier transform of the power spectrum, $P(k) = \langle |\delta(k)|^2 \rangle$. Note that the 2-point function is a complete description of the field only in the case of a Gaussian distribution. For more realistic cases, one requires the higher order $p$-point moments, $\xi_p(R)$. We explore the higher order correlation function of the observed galaxy distribution in detail in Chapters 2, 3, and 4.

Interestingly, it was quickly realised that galaxies had to be a *biased* tracer of the underlying density field. This can be seen by comparing the 2-point galaxy-galaxy correlation function and cluster-cluster correlation function. Such observations reveal that, although both correlation functions have the same power law slope, the cluster-cluster correlation function has an amplitude approximately 20 times larger. If both galaxies and clusters arise from the same gravitational instability and amplification of the initial density field, then this observation indicates that distinct samples of galaxies must trace the underlying mass distribution in different ways. This phenomenon is generally known as galaxy bias.

The bias of galaxies relative to the mass can be understood from the statistics of Gaussian random fields (Kaiser 1984). Consider that a massive cluster is expected to form at the centre of a rare high $\sigma$ density peak in the background matter field and that such peaks collapse early and tend to occur near other peaks. Because of this, even a relatively weak correlation on large scales can be amplified with respect to the background by a factor of $\nu^2$, where $\nu$ is the number of $\sigma$ that corresponds to the density fluctuation. For $\nu^2 = 20$ above,

the most massive clusters can correspond to $\sim 4\sigma$ fluctuations, explaining the very low spatial density of such rare objects. Density fluctuations of lower amplitude, such as those which represent isolated galaxies, will collapse on longer timescales and be distributed in a way that is more representative of the overall mass distribution.

In the simplest picture, bias is usually quantified as the relative clustering strength of galaxies with respect to the underlying dark matter through the 2-point correlation function:

$$\xi_2^{\text{gal}} = b^2 \, \xi_2^{\text{DM}} \, , \tag{1.10}$$

where $b$ is the ubiquitous linear biasing term. As always, the true picture is not quite this simple, however. Both linear and non-linear bias are possible in the galaxy distribution, and this is an effect we will explore using both the low and higher order clustering moments of the observed galaxy distribution.

## 1.5 Observed and mock galaxy populations

In this thesis we will exploit both observed and simulated galaxy catalogues. Both are of such quality that we can undertake statistical analyses of unprecedented accuracy. We now give a brief description of both.

### The Two Degree Field Galaxy Redshift Survey

The Two Degree Field Galaxy Redshift Survey (2dFGRS) is an international collaboration which has had the ambitious aim of measuring the redshifts of approximately 250,000 galaxies in the local universe (Colless et al. 2001, 2003). This has been made possible with the use of the 2dF multi-fibre spectrograph on the Anglo-Australian Telescope, which is capable of observing 400 objects simultaneously over a 2 degree field. The catalogue is sourced from a revisited and extended version of the APM galaxy catalogue (Maddox et al. 1990), and the targets are galaxies with extinction corrected magnitudes brighter than $b_J$=19.45.

The main survey area covers approximately 2000 deg$^2$ and has a median depth of $z = 0.11$. The area is centred on two declination strips, one in the southern galactic hemisphere spanning $80° \times 15°$ close to the south galactic pole, and the other in the northern galactic hemisphere spanning $75° \times 10°$ along the celestial equator (Fig. 1.1). In this thesis, catalogues will be built with galaxies from both regions. At the effective limit of the survey, $z \approx 0.3$, the strips contain an approximate volume of $10^8 h^{-1} \text{Mpc}^3$ (for $\Omega_m = 0.3$, $\Omega_\Lambda = 0.7$). An additional 99 random fields are distributed around the southern galactic cap but are not used in this work.

Due to clustering variations across the observed fields, adaptive tiling was adopted to make efficient use of the 2dF spectrograph. This resulted in field sampling at a near uniform rate of 93% across the whole survey region. Redshifts were measured from spectra covering 3600-8000Å by both cross-correlation with a range of template spectra and by fitting strong spectral features. All redshifts were visually checked and assigned a quality
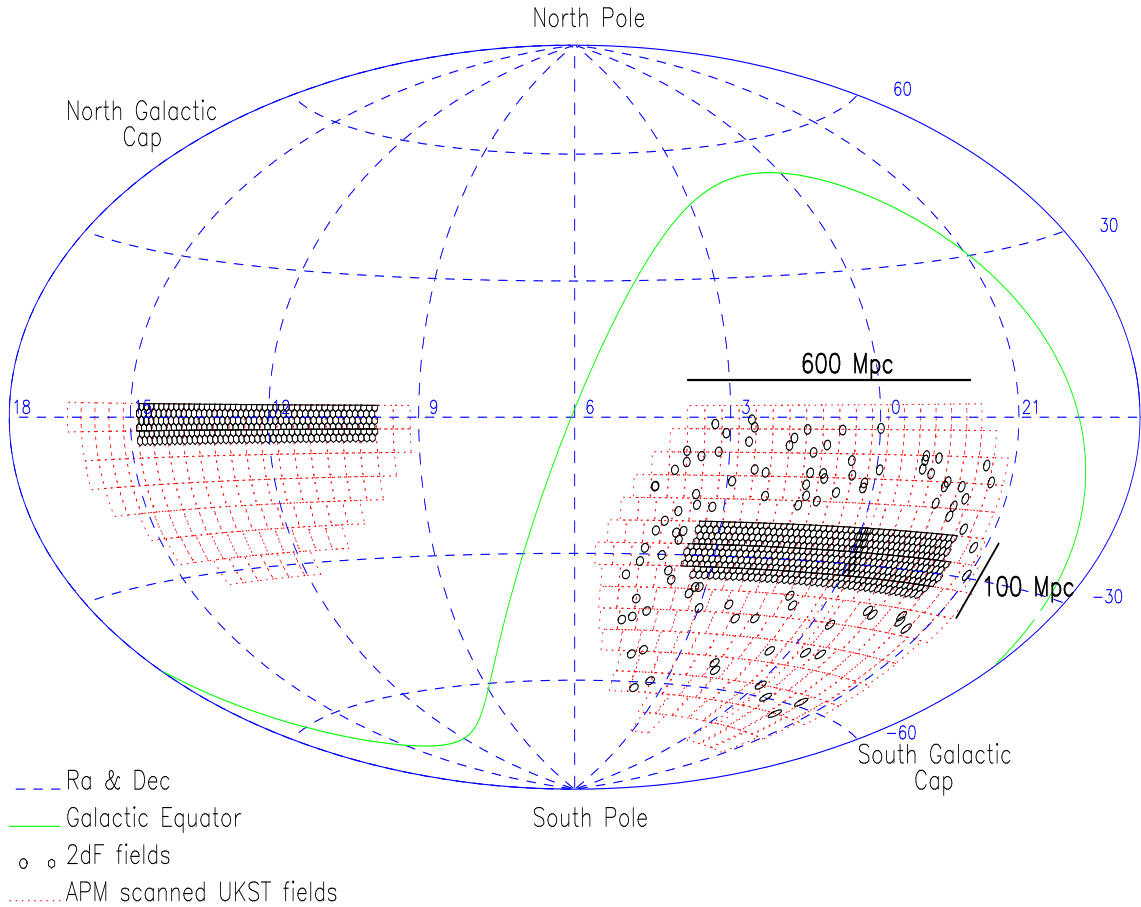
**Figure 1.1:** An all sky plot of the APM/2dFGRS survey area. The individual 2dFGRS fields are marked as small circles, with the larger south galactic pole region lying to the right of the figure, and the smaller more north galactic pole region on the left.

parameter $Q$ in the range of 1-5, with 5 being of highest quality and 1 being the poorest. An accurate statistical analysis of the final galaxy catalogue required spatial and magnitude incompleteness to be compensated for. This was achieved in the standard way by defining three masks through which the data was processed: (1) a magnitude limit mask giving an extinction corrected apparent magnitude limit as a function of position on the sky, (2) a redshift completeness mask providing the fraction of measured redshifts at each position, and (3) a magnitude completeness mask linking redshift success rate with apparent magnitude. These masks also include holes, which define the excluded regions from the survey area due to effects such as foreground stars and plate flaws, for example. The overall average redshift completeness of the parent catalogue is found to be 91.8%.

Using the masks we pre-filter the 2dFGRS parent catalogue in order to remove any un-

wanted objects and badly sampled galaxies. To do this, we choose only galaxies with apparent magnitudes in the range $14.0 < m < m_{\mathrm{lim}}$, where $m_{\mathrm{lim}}$ varies as a function of angle on the sky ($<m_{\mathrm{lim}}> = 19.37$), redshifts within the range $0.002 < z < 0.5$, to avoid selecting stray stars or quasars, and a redshift quality of at least $Q \geq 3$, to ensure accurate distance estimation. From the 221,414 unique redshifts obtained, the above constraints provide 194,407 quality redshifts with which to do our analysis – 113,895 in from the SGP region and 80,512 from the NGP region. This galaxy catalogue forms the basis with which we undertake our analyses in Chapters 2, 3, 4 and 5.

## Galaxy formation models

To understand many problems in astronomy, including those specific to galaxy formation and the galaxy population as a whole, astronomers have often turned to the exploration of potential solutions through computer simulations. In this field, two important and complimentary techniques have developed over the last 10 or so years. Hydrodynamic simulations follow the co-evolution of both gas and dark matter explicitly, and this approach has been integral to understanding many astrophysical phenomena. However, due to the heavy computational cost of hydrodynamic methods, they are usually limited in either size or resolution when compared with pure N-body techniques. To circumvent these shortcomings one can instead take a 'semi-analytic' approach (e.g. White & Frenk 1991) based on the galaxy formation paradiam outlined by White & Rees (1978). In the semi-analytic picture, the physics important to galaxy formation is modelled analytically in parallel to the numerical evolution of pure N-body dark matter. Its power lies in the relatively minor computational cost of implementation, and this allows for speedy exploration of parameter space around many different models relating to the question at hand. We will follow this second approach.

The galaxy formation model we use in Chapter 6 is implemented on top of a very large dark matter simulation of the concordance $\Lambda$CDM cosmology. We have dubbed this simulation the 'Millennium Run' because of its size and resolution (Springel et al. 2005 – see Fig. 1.2). The Millennium Run follows the dynamical evolution of $2160^3 \simeq 1.0078 \times 10^{10}$ dark matter particles in a periodic box of $500\,h^{-3}\mathrm{Mpc}^3$, which implies a mass resolution per particle of $8.6 \times 10^8\,h^{-1}\mathrm{M}_{\odot}$. We adopt cosmological parameter values consistent with a combined analysis of the 2dFGRS (Colless et al. 2001) and first year WMAP data (Spergel et al. 2003; Seljak et al. 2004). They are $\Omega_{\mathrm{m}} = \Omega_{\mathrm{dm}} + \Omega_{\mathrm{b}} = 0.25$, $\Omega_{\mathrm{b}} = 0.045$, $h = 0.73$, $\Omega_{\Lambda} = 0.75$, $n = 1$, and $\sigma_8 = 0.9$.

Friends-of-friends (FOF) halos are identified in the simulation using a linking length of 0.2 the mean particle separation, while sub-structure *within* each FOF halo is found with an improved and extended version of the SUBFIND algorithm of Springel et al. (2001). Having determined all halos and subhalos at all output snapshots, we then build the hierarchical merging trees that describe in detail how structures grow as the universe evolves. These trees form the backbone onto which we couple our model of galaxy formation.

Inside each tree, virialised dark matter halos at each redshift are assumed to attract ambient gas from the surrounding medium, from which galaxies form and evolve. Our model
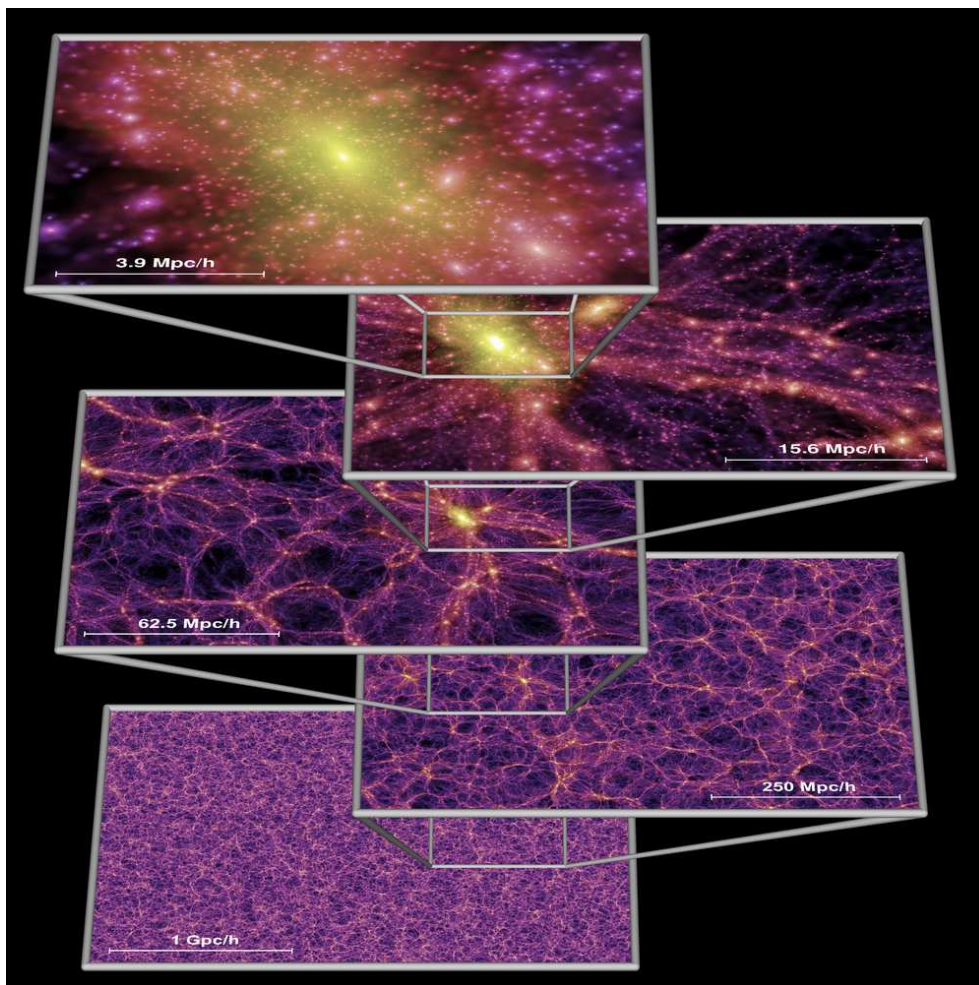
**Figure 1.2:** The Millennium Run ΛCDM N-body simulation. Each panel represents a magnification by factors of four, highlighting the rich structure the simulation can resolve. The colour coding is by local density and dark matter velocity dispersion.

effectively tracks a wide range of galaxy formation physics in each halo, including reionization of the inter-galactic medium at high redshift, star formation in the cold disk and the resulting supernova feedback, black hole growth and AGN feedback through the 'quasar' and 'radio' epochs of AGN evolution, metal enrichment of the inter-galactic and intracluster medium, and galaxy morphology shaped through mergers and merger induced starbursts. In Chapter 6 we describe this model and its application in detail.

## 1.6 Thesis overview

This thesis is a collection of five papers, four of which are published in the Monthly Notices of the Royal Astronomical Society (MNRAS, Chapters 2–5), and the last of which has recently been submitted to the MNRAS. In this body of work we cover three main areas of research: (i) the higher order clustering of the large scale distribution of the local galaxy population (Chapters 2–4), (ii) the environmental dependence of the luminosity function for early and late type galaxy populations (Chapter 5), and (iii) the way in which the suppression of cooling flows shape the properties of the massive galaxy population (Chapter 6). We now give a brief overview of each of these chapters in turn.

### Higher order clustering in the local universe

The first half of this thesis, Chapters 2, 3, and 4, describe a study of the higher-order clustering in the 2dFGRS. In Chapter 2 we measure the clustering moments of the local $L_*$ galaxy population using a volume limited sample contained a total of 44,931 galaxies within the magnitude range $-19 > M_{b_J} - 5\log_{10} h > -20$ and survey volume defined by $0.02 < z < 0.13$. Using this probe, we investigate if the $p$-point galaxy correlation functions, $\bar{\xi}_p$, can be written in terms of the two point correlation function or variance, $\bar{\xi}_p = S_p \bar{\xi}_2^{p-1}$, for some constant hierarchical scaling values, $S_p$. This is the so-called hierarchical scaling hypothesis, and is expected if an initially Gaussian distribution of density fluctuations evolves under the action of gravitational instability. The quality of our measurement is such that we can measure the moments up to sixth order across scales $0.3 < R\,(h^{-1}\mathrm{Mpc}) < 30$. We compare our results with those from the Hubble Volume $\Lambda$CDM N-body simulation to look for signatures of non-linear biasing between the galaxies and underlying dark matter halo density field. In this chapter, we also discuss the impact of two rare, massive superclusters in the 2dFGRS volume on the higher order clustering moments of the $L_*$ galaxy distribution.

In Chapter 3 we take this analysis one step further by measuring the higher order moments of the 2dFGRS galaxy distribution as a function of galaxy luminosity. We use the full survey, approximately 200,000 galaxies, and build volume limited catalogues in one magnitude bins covering the magnitude range $-17 > M_{b_J} - 5\log_{10} h > -22$, sampling the spatial distribution of galaxies out to scales of $z \approx 0.3$ ($\sim 750 h^{-1}\mathrm{Mpc}$). With these galaxy samples, we investigate how hierarchical scaling in the clustering distribution varies with galaxy luminosity, again up to sixth order. Past analyses have shown that the hierarchical scaling coefficients, $S_p = \bar{\xi}_p / \bar{\xi}_2^{p-1}$, are approximately independent of scale, and we look for this behaviour as well. As in Chapter 2, the influence of two massive superclusters in the 2dFGRS is quantified, especially on large scales where their presence is most likely to be seen. Chapter 3 also provides a comprehensive analysis of both linear and non-linear biasing in the galaxy distribution. We investigate the *relative* bias in the 2dFGRS, with respect to the $L_*$ population, as a function of luminosity using the clustering moments. The results of this chapter generalise those found in Chapter 2.

Chapter 4 concludes our study of higher order clustering in the 2dFGRS. We take a "re-

verse" approach to the previous method by measuring the *reduced void probability function* (VPF) of the galaxy distribution in volume limited catalogues covering magnitudes from $M_{b_J} - 5\log_{10} h = -18$ to $-22$. The VPF connects the distribution of voids to the moments of galaxy clustering of *all* orders. The reduced VPF can be used to both measure hierarchical scaling in the clustering moments and to discriminate between different clustering models that make predictions for how this scaling should arise. Such models include the lognormal distribution and the negative binomial model, which we show we can discriminate between at a high significance. Thus, the predictive power of the reduced VPF makes this chapter a valuable extension to the previous two. In addition, as the reduced VPF is weighted more by the lower and intermediate counts in the galaxy probability distribution function, we show that these results are insensitive to superclusters in the 2dFGRS volume, unlike the results of the previous two chapters. We also measure the reduced VPF for dark matter in a $\Lambda$CDM universe and compare to that found for the galaxy population.

## Environmental dependence of the galaxy luminosity function

In Chapter 5, we shift our focus from the spatial distribution of the local galaxy population to the properties of galaxies that lie within this distribution. Here we study the luminosity functions of galaxies in different large-scale density environments, from sparse voids to the densest cluster regions. To do this, we develop a new method to measure the environmental dependent luminosity function and demonstrate that it gives comparable results to previous methods but with the added bonus of simultaneously providing the luminosity function normalisation as well as shape. Our analysis includes the separation of the galaxy population into early and late spectral types. Using the Schechter function parameterisation of the luminosity function, we measure the characteristic luminosity and faint-end slope in each environment. This parametrisation allows us to demonstrate the smooth change in the galaxy population between extremes in density and, when examined as a function of spectral type, quantifies the differences between the galaxies in clusters, mean density, and void regions of the universe, for both early and late types. We finish with a discussion of our results in light of current galaxy formation models.

## Cooling flows and the properties of massive galaxies

Finally, in Chapter 6 we couple a self consistent model of galaxy formation to the Millennium Run $\Lambda$CDM N-body simulation to study the effect of cooling flow suppression on the local galaxy properties. The resolution of the Millennium Run is such that the detailed assembly history of each object in the simulation, as faint as galaxy luminosities approximately equal to the Small Magellanic Cloud, is accurately followed in a volume comparable to that of the 2dFGRS. In our galaxy formation model, we supplemented previous treatments of the growth and activity of central black holes with a new model for 'radio' feedback from those AGN that lie at the centre of a quasistatic X-ray emitting atmosphere in a galaxy group or cluster. We explore how such radio feedback modifies the drop-out rate in cooling flows and the effect this has on the properties of massive galaxies,

such as mean stellar ages and colours. More generally, we examine how cooling flow suppression changes the bright end of the galaxy luminosity function, which previous models of galaxy formation have had difficulty accounting for.

# 2 Hierarchical galaxy clustering in the 2dFGRS[1]

## Abstract

We use the two-degree field Galaxy Redshift Survey (2dFGRS) to test the hierarchical scaling hypothesis: namely, that the $p$-point galaxy correlation functions can be written in terms of the two point correlation function or variance. This scaling is expected if an initially Gaussian distribution of density fluctuations evolves under the action of gravitational instability. We measure the volume averaged $p$-point correlation functions using a counts-in-cells technique applied to a volume limited sample of 44,931 $L_*$ galaxies. We demonstrate that $L_*$ galaxies display hierarchical clustering up to order $p = 6$ in redshift space. The variance measured for $L_*$ galaxies is in excellent agreement with the predictions from a $\Lambda$-cold dark matter N-body simulation. This applies to all cell radii considered, $0.3 < (R/h^{-1}\mathrm{Mpc}) < 30$. However, the higher order correlation functions of $L_*$ galaxies have a significantly smaller amplitude than is predicted for the dark matter for $R < 10h^{-1}\mathrm{Mpc}$. This disagreement implies that a non-linear bias exists between the dark matter and $L_*$ galaxies on these scales. We also show that the presence of two rare, massive superclusters in the 2dFGRS has an impact on the higher-order clustering moments measured on large scales.

## 2.1 Introduction

Current theoretical models of structure formation in the Universe are based on the paradigm of gravitational instability. This process is believed to be responsible for driving the growth of small primordial density perturbations into the nonlinear collapsed structures such as galaxies and clusters that are evident in the Universe today.

The premise of gravitational instability has been tested indirectly by comparing the clustering predicted by numerical simulations of the formation of cosmic structures with the observed distribution of galaxies (e.g. Benson et al. 2001). A direct test of this fundamental ingredient of structure formation models was made using the 2dFGRS by Peacock et al. (2001). The size of the 2dFGRS allowed the first accurate measurement of the two-point

---

[1]C.M. Baugh, **D.J. Croton**, E. Gaztañaga, P. Norberg, M. Colless, et al. (the 2dFGRS Team), MNRAS, 351, 44, 2004

galaxy correlation function on large scales. Peacock et al. demonstrated that the two-point correlation function at large pair separations displays a form that is characteristic of the bulk motions of galaxies expected in the gravitational instability scenario.

We present an independent test of the gravitational instability paradigm. For a Gaussian distribution of density fluctuations, the volume averaged correlation functions, $\bar{\xi}_p$, are identically zero for $p > 2$; the density field is completely described by its variance, $\bar{\xi}_2$. The evolution of an initially Gaussian density field due to gravitational instability generates non-zero $\bar{\xi}_p$ (Peebles 1980). A basic test of the gravitational origin of the higher order moments is to determine their relation to the variance of the distribution. This is traditionally encapsulated in the hierarchical model:

$$\bar{\xi}_p = S_p \bar{\xi}_2^{p-1}. \tag{2.1}$$

This model applies to real space clustering; however, in redshift space the scaling still tends to hold even on small scales where the "fingers-of-God" effect is prominent (Lahav et al. 1993; Hoyle, Szapudi & Baugh 2000). Perturbation theory predicts that the hierarchical amplitudes for the mass distribution are independent of the cosmological density parameter, the cosmological constant and cosmic epoch (Bernardeau et al. 2002).

We use the 2dFGRS (Colless et al. 2001, 2003) to measure the higher order correlation functions of the galaxy distribution, focusing on the clustering of $L_*$ galaxies. The size of the 2dFGRS is exploited to extract a volume limited sample of $L_*$ galaxies, which greatly simplifies our analysis (Section 2.2). The results for the volume averaged correlation functions, up to sixth order, are presented in Section 2.3, in which we also test how well the hierarchical scaling model works. Our conclusions are given in Section 2.4.

## 2.2 Data and analysis

The density of galaxies is a strong function of radial distance in a magnitude limited survey. This needs to be compensated for in any clustering analysis by applying a suitable weighting scheme (e.g. Saunders et al. 1991). Alternatively, one may construct a volume limited sample by selecting certain galaxies from the full redshift survey. These galaxies are chosen so that they would appear inside the apparent magnitude range of the survey if displaced to any redshift within the interval defining the sample. The only radial variation in galaxy number density in a volume limited sample is due to large scale structure in the galaxy distribution. This makes volume limited samples much more straightforward to analyse than flux limited samples. However, only a fraction of the galaxies from the full redshift survey satisfy the selection criteria in redshift and absolute magnitude. This reduction in the density of galaxies has curtailed the utility of volume limited subsamples constructed from earlier redshift surveys.

We construct a volume limited sample of $L_*$ galaxies from the 2dFGRS. The motivation for the choice of a sample centred on $L_*$ is clear; this results in a volume limited sample with the largest possible number of galaxies for magnitude bins of a given size. As the luminosity used to define a sample increases, the selected galaxies can be seen out to
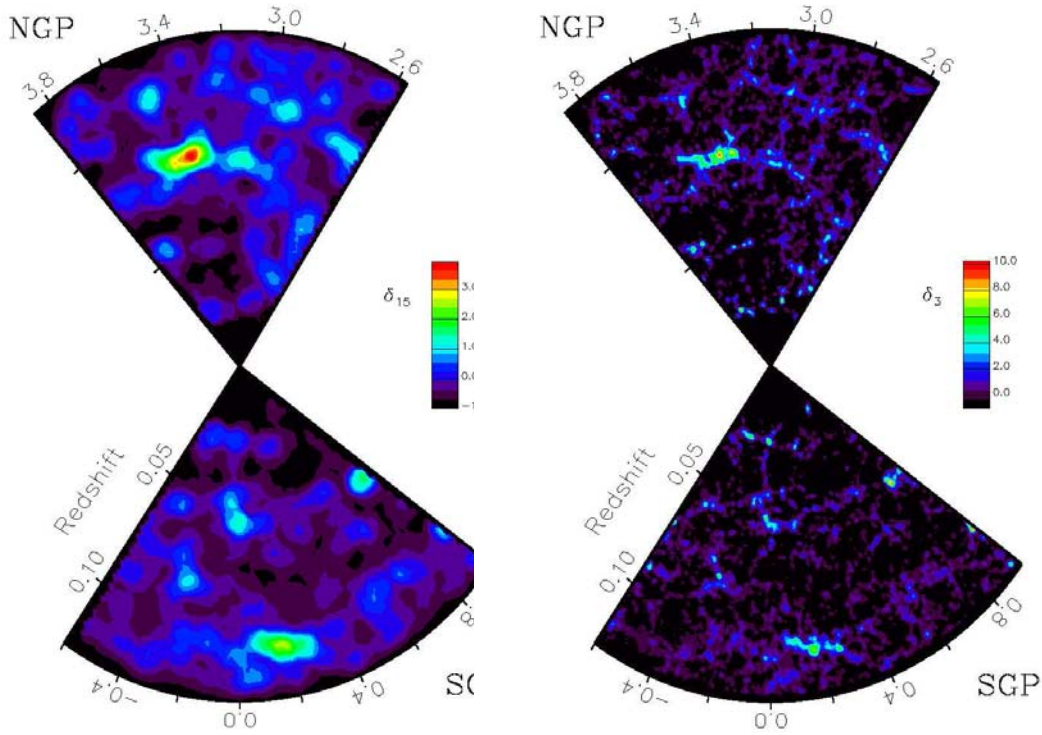
**Figure 2.1:** The projected galaxy density in the $L_*$ volume limited sample, smoothed on two different scales. The galaxy distribution is projected onto the right ascension–redshift plane and is then smoothed in circular cells of radius $15h^{-1}$Mpc (left) and $3h^{-1}$Mpc radius (right). Redder colours denote higher densities as indicated by the key that accompanies each panel. Two 'hotspots' stand out clearly, particularly in the left hand coneplots; one in the NGP at $z \approx 0.08$ and the other in the SGP at $z \approx 0.11$. Right ascension is given in radians.

larger redshifts and thus sample larger volumes. However, brighter than $L_*$, the space density of galaxies drops exponentially (e.g. Norberg et al. 2002b). Hence, the optimum balance between volume surveyed and intrinsic galaxy space density is achieved for $L_*$ galaxies. In addition, the higher order clustering of $L_*$ galaxies provides a benchmark or reference against which to compare trends in clustering strength with galaxy luminosity (see Norberg et al 2001; Croton et al. 2004b). We consider the two contiguous areas of the 2dFGRS, referred to as the NGP and SGP regions, which contain around 190,000 galaxies with redshifts and cover an effective area of approximately 1200 square degrees in total. After selecting galaxies with absolute magnitudes in the range $-19 > M_{b_J} - 5\log_{10} h > -20$ (corrected to $z = 0$ using the global $k + e$ correction quoted by Norberg et al. 2002b), the volume limited sample contains 44,931 galaxies. The redshift interval of the sample is

$z = 0.021$ to $0.130$, corresponding to a volume of $7.97 \times 10^6 h^{-3} \text{Mpc}^3$ for the combined NGP and SGP regions.

### 2.2.1 Counts-in-cells

The distribution of counts-in-cells is estimated by throwing down a large number of spherical cells, on the order of $10^7$ for each cell radius considered, within the $L_*$ volume limited 2dFGRS sample. Full details of how we deal with the spectroscopic incompleteness and the angular mask are given in Croton et al. (2004b); the corrections turn out to be small in any case (see figure 1 of Croton et al.).

The higher order correlation functions, $\bar{\xi}_p$, are the reduced $p^{\text{th}}$ order moments of the distribution of galaxy counts-in-cells. The estimation of the higher order correlation functions from the cell count probability distribution is explained in a number of papers (e.g. Gaztañaga 1994; Baugh, Gaztañaga & Efstathiou 1995; Croton et al. 2004b). The variance or width of the count distribution is given by the case $p = 2$. For $p > 2$, the correlation functions probe further out into the tail of the count probability distribution.

We use mock 2dFGRS catalogues to estimate the errors on the measured higher order correlation functions. Full details of the mocks can be found in Norberg et al. (2002b) and Croton et al. (2004b).

## 2.3 Results

The projected density of galaxies in the $L_*$ volume limited sample is shown in Fig. 2.1. The galaxy density projected onto the right ascension–redshift plane is smoothed using circular windows. Two different smoothing radii have been used to produce these maps; the left-hand panel shows the density after smoothing with a circular cell of radius $15h^{-1}\text{Mpc}$ and the right hand panel shows the distribution as sampled with a cell of radius $3h^{-1}\text{Mpc}$. The redder colours indicate higher galaxy densities, as shown by the scale that accompanies each cone plot. Two 'hot-spots' are readily apparent, particularly in the cone plot smoothed on the larger scale. These correspond to superclusters of galaxies that also appear in the 2dFGRS Percolation Inferred Galaxy Group catalogue (Eke et al. 2004) and in the reconstructed density field of the 2dFGRS (Erdogdu et al. 2004). The presence of these superclusters has an impact on the extreme event tail of the count probability distribution. Later in this section, we will investigate the influence of these structures on our measurement of the higher order correlation functions by excising the volumes that contain the superclusters from our analysis. The 'cosmic web' of filamentary structures and voids is apparent in the cone smoothed on the smaller scale.

The higher order correlation functions measured for $L_*$ galaxies are plotted in Fig. 2.2. The correlation functions are only plotted on scales for which a robust measurement is possible. The correlation functions show a dramatic steepening on small scales as the order $p$ increases. For example, the ratio $\bar{\xi}_6/\bar{\xi}_2$ is $10^5$ at $R = 1h^{-1}\text{Mpc}$, falling to $\sim 100$ at $R = 6.3h^{-1}\text{Mpc}$. We also plot the higher order correlation functions for the dark matter dis-
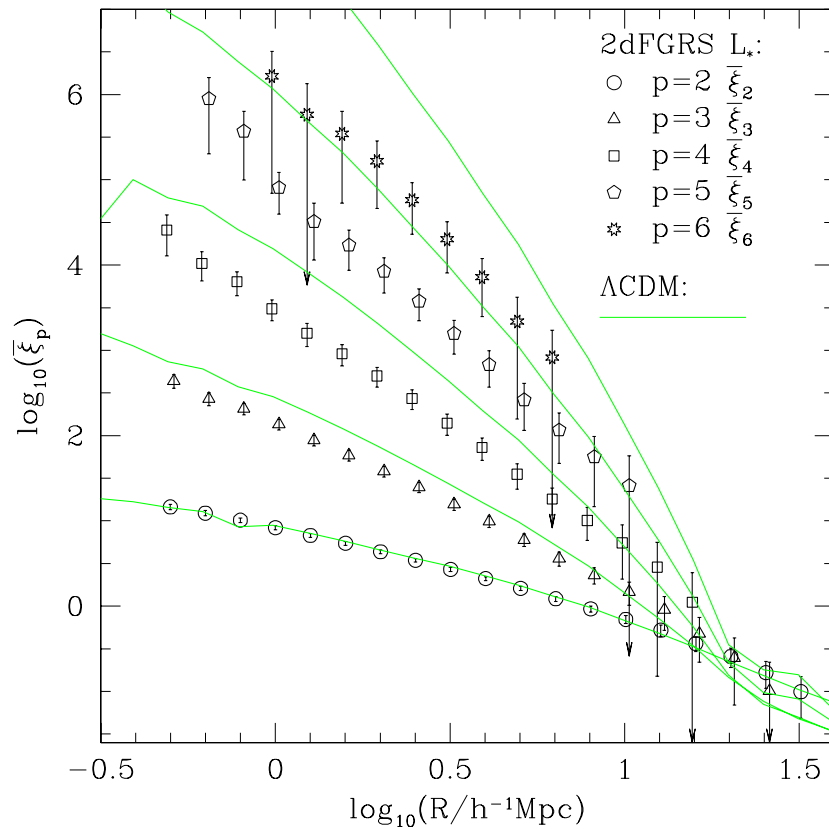
**Figure 2.2:** The higher order correlation functions $\bar{\xi}_p$ measured for $L_*$ galaxies in the 2dFGRS (symbols). The orders $p = 2$–6 are shown, as indicated by the key. The errorbars show the *rms* scatter estimated using mock 2dFGRS catalogues. The lines show the $\bar{\xi}_p$ measured for the dark matter in redshift space in the ΛCDM Hubble Volume simulation, for orders $p = 2$ to 6 in sequence of increasing amplitude for $R < 10h^{-1}$Mpc.

tribution in the ΛCDM Hubble Volume simulation (Evrard et al. 2002). These theoretical predictions include the effects of peculiar motions in the distant observer approximation. The variance of the dark matter in redshift space agrees spectacularly well with the measured $\bar{\xi}_2$ for $L_*$ galaxies. This confirms the conclusions reached in independent analyses of the clustering of $L_*$ galaxies in the 2dFGRS (Lahav et al. 2002; Verde et al. 2002). However, for the case of the ΛCDM Hubble Volume simulation, the $p > 2$ moments of the dark matter differ from the measurements for $L_*$ galaxies for $R < 10h^{-1}$Mpc.

The hierarchical amplitudes, $S_p$, obtained from the $\bar{\xi}_p$ by applying Eq. 2.1 are plotted as a function of cell radius for orders $p = 3$–5 in Fig. 2.3 ($p = 6$ is omitted for clarity).
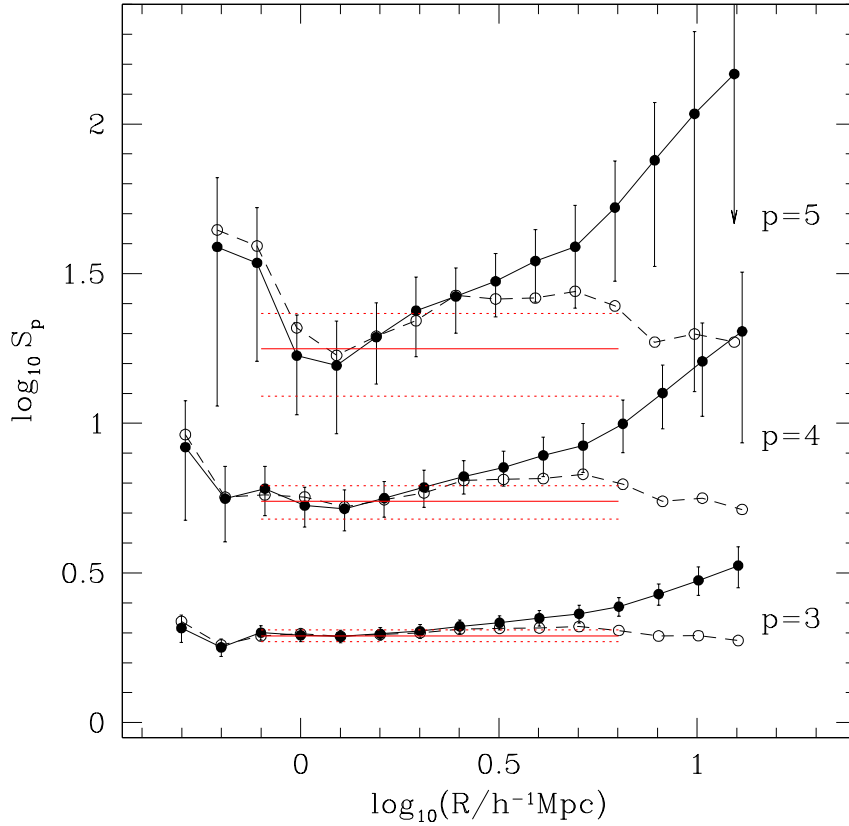
**Figure 2.3:** The hierarchical amplitudes, $S_p$, for $p = 3, 4$ and $5$, plotted as a function of cell radius for the $L_*$ volume limited sample. The filled symbols connected by solid lines show the results obtained using the full volume. The best fit constant values of $S_p$ are shown by the horizontal solid lines, which are plotted over the range of scales used in the fit. The dotted lines show the $1-\sigma$ error on the fit. The open symbols connected by dashed lines show the hierarchical amplitudes recovered when the two largest superclusters are masked out of the volume.

For $p = 3$, $S_3$ is approximately constant for cells with $R < 3h^{-1}$Mpc. At larger $R$, $S_3$ increases with radius. This behaviour is mirrored for $p > 3$, with the upturn in $S_p$ seen at progressively smaller radii as $p$ increases. Perturbation theory predicts that, on large scales, the $S_p$ should have only a weak dependence on scale for CDM-like power spectra (Juszkiewicz, Bouchet & Colombi 1993). In redshift space, the hierarchical amplitudes are expected to be approximately independent of scale over an even wider range of scales than those on which perturbation theory is applicable (Hoyle et al. 2000; Bernardeau et al.
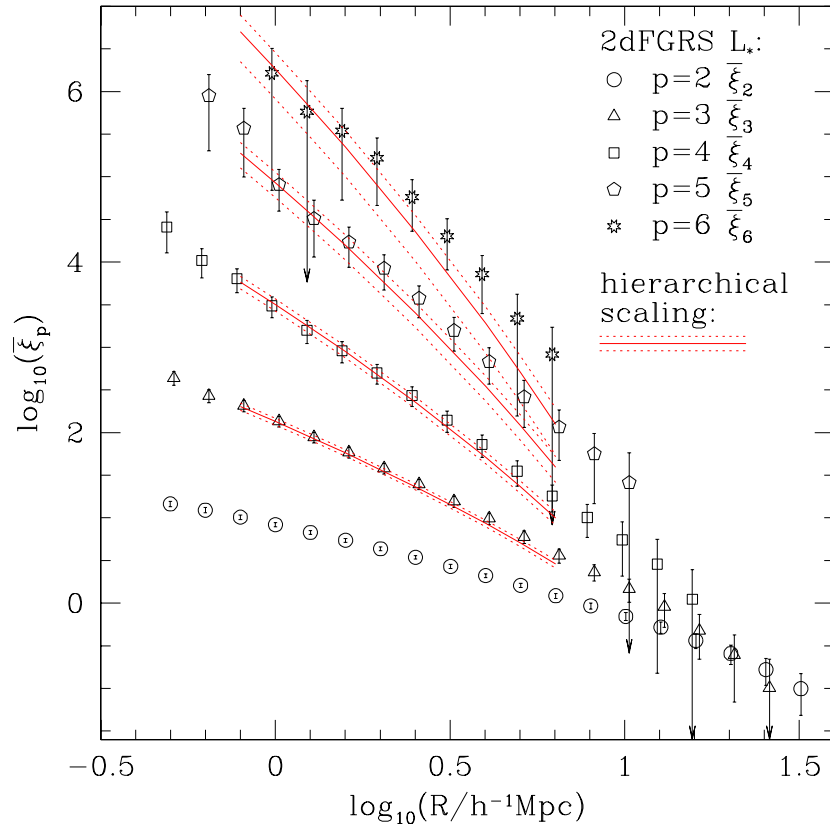
**Figure 2.4:** The higher order correlation functions, $\bar{\xi}_p$, measured for $L_*$ galaxies in the 2dFGRS (symbols, as in Fig. 2) compared with the predictions of the hierarchical model (Eq. 2.1; solid lines). The hierarchical predictions are plotted only on the scales used to fit $S_p$. The dotted lines indicate the errors on these predictions, with contributions from the error on the fitted value of $S_p$ and on the measured variance $\bar{\xi}_2$.

2002). We therefore attempt to fit a constant value of $S_p$ to the ratios plotted in Fig. 2.3. We use a principal component analysis to take into account the correlation between the $\bar{\xi}_p$ in neighbouring bins (e.g. Porciani & Givalisco 2002; for further details of our implementation see Croton et al. 2004b). The results of this analysis are given in Table 2.1. In Fig. 2.3, the horizontal lines show the best fit constant value for $S_p$, fitted over the scales $0.71 < (R/h^{-1}\mathrm{Mpc}) < 7.1$. The same range of scales is used to fit the $S_p$ for each order $p$. (The choice of scales is set by the cell radii for which a reliable measurement of $\bar{\xi}_6$ is possible.) The dotted lines indicate the $1\sigma$ uncertainty on the fit. The errorbars plotted in Fig. 2.3 show only the diagonal component of the full covariance matrix. The amplitudes

21

| order | $S_p$ | $\pm 2\sigma$ | $\chi^2$/ndof |
|:-----:|:-----:|:-------------:|:-------------:|
| 3 | 1.95 | 0.18 | 6.1 |
| 4 | 5.50 | 1.43 | 2.8 |
| 5 | 17.8 | 10.5 | 1.9 |
| 6 | 46.3 | 50 | 1.1 |

**Table 2.1:** The best fit values for $S_p$ and the $2-\sigma$ error ($\Delta\chi^2 = 4$), obtained using the measurements for cell radii in the range $0.71 \le (R/h^{-1}\text{Mpc}) \le 7.1$. The $2-\sigma$ errors are approximately twice the size of the $1-\sigma$ errors. The final column gives the reduced $\chi^2$ using the number of degrees of freedom derived from the principal component analysis.

$S_p$ are extremely correlated, with the principal component analysis showing that the first few eigenvectors contain the bulk of the variance, indicating that there are typically just 2 or 3 independent points. Sample variance leads to measurements which could be coherently shifted either low or high with respect to a fixed value. This therefore drives the best fit value of $S_p$ to lie either below or above a sizeable fraction of the data points. For the $L_*$ sample, we note that neither $S_3$ nor $S_4$ are particularly well described by a constant fit (see the reduced $\chi^2$ values in Table 2.1).

For purely illustrative purposes, we have carried out the experiment of removing the two superclusters from the $L_*$ volume limited sample and repeating our measurement of the higher order correlation functions. The corresponding results for the hierarchical amplitudes are plotted using open symbols in Fig. 2.3. The upturn in the $S_p$ values at large radii is no longer apparent. Rather than being considered as a correction, the results of this exercise simply serve to show the influence of the supercluster regions on our measurements of the $\bar{\xi}_p$. Where the difference matters, it effectively indicates that the volume of even the 2dFGRS is too small to yield a robust higher-order clustering measurement. A further discussion of this test is given by Croton et al. (2004b).

Armed with the best fit values of $S_p$, the hierarchical model stated in Eq. 2.1 can be used to make predictions for the form of the higher order correlation functions and compare these with the measurements from the 2dFGRS $L_*$ galaxy sample (symbols in Fig. 2.4, reproduced from Fig. 2.2). The solid lines in Fig. 2.4 show the $\bar{\xi}_p$ predicted from the hierarchical scaling relation (Eq. 2.1), assuming a constant value for the hierarchical amplitudes, $S_p$, and using the measured variance, $\bar{\xi}_2$. The dotted lines show the uncertainty in the theoretical predictions, derived from the $1-\sigma$ error in the fitted values of the $S_p$ and the error on the measured variance, $\bar{\xi}_2$. The theoretical predictions for the different orders agree spectacularly well with the measured higher order correlation functions over the range of scales for which the $S_p$ are fitted.

## 2.4 Conclusions

We have measured the higher order correlation functions of $L_*$ galaxies up to sixth order in the 2dFGRS. Previous studies of galaxy clustering in redshift space have been limited to fourth order (e.g. for optically selected samples: Gaztañaga 1992; Benoist et al. 1999; Hoyle et al. 2000: for infra-red selected samples: Bouchet et al. 1993; Szapudi et al. 2000). The volume limited sample of $L_*$ galaxies analysed here contains 100 times more galaxies and covers 10 times the volume of the previous best measurements from an optically selected galaxy redshift survey (Hoyle et al. 2000). The measured correlation functions have a form that is in remarkably good agreement with the predictions of hierarchical scaling, and extend to smaller scales than those for which the perturbation theory predictions are expected to be valid (Bernardeau et al. 2002). A similar conclusion was reached by Croton et al. (2004a), who found hierarchical scaling in the reduced void probability function measured in the 2dFGRS.

On scales larger than about $4h^{-1}$Mpc, there is an upturn in the values of $S_p$, which we have demonstrated is influenced by the presence of two large superclusters in the 2dFGRS (see Fig. 2.3). This suggests that finite sampling affects our measurements on these scales. A similar feature was found in the angular Edinburgh-Durham Southern Galaxy Catalogue (EDSGC). Szapudi & Gaztañaga (1998) found that the projected $S_p$ measured from the EDSGC displayed an up-turn for scales larger than 0.5 degrees, which corresponds to $\approx 4h^{-1}$Mpc at the characteristic depth of the survey. The EDSGC covers a similar part of the sky to the 2dFGRS. This feature in $S_p$ was not found, however, in the APM Survey, which covers a four times larger solid angle than the EDSGC (Gaztañaga 1994). This behaviour is not seen in the mock catalogues drawn from the $\Lambda$CDM Hubble Volume simulation. Intriguingly, an upturn in the hierarchical amplitudes on large scales is expected in structure formation models with non-Gaussian initial density fields (Gaztañaga & Fosalba 1998; Bernardeau et al. 2002).

Finally, we note that the variance of the distribution of cell counts for $L_*$ galaxies is in excellent agreement with the predictions for CDM, obtained from the Hubble Volume $\Lambda$CDM simulation, which includes the effects of peculiar motions on the clustering pattern. However, for cells with radii $R < 10h^{-1}$Mpc the higher order correlation functions of $L_*$ galaxies have significantly lower amplitudes than the dark matter. This implies that the relation between the distribution of galaxies and the underlying dark matter may be more complicated than the popular linear bias model, suggesting that nonlinear contributions to the bias may be important on small and intermediate scales (Fry & Gaztañaga 1993; see also the analyses by Conway et al. 2005 and Wild et al. 2005). We note that on large scales ($R > 10h^{-1}$Mpc), the $\bar{\xi}_p$ measured for $L_*$ galaxies agree better with the $\Lambda$CDM predictions, supporting the conclusion reached previously, that on these scales, $L_*$ galaxies approximately trace the mass distribution (Gaztañaga & Frieman 1994; Lahav et al. 2002; Verde et al. 2002).

We explore the distribution of galaxy counts-in-cells for the 2dFGRS in more detail in Croton et al. (2004b), where we study the dependence of the correlation functions on luminosity.

# 3 Higher order clustering in the 2dFGRS[1]

## Abstract

We measure moments of the galaxy count probability distribution function in the two-degree field galaxy redshift survey (2dFGRS). The survey is divided into volume limited subsamples in order to examine the dependence of the higher order clustering on galaxy luminosity. We demonstrate the hierarchical scaling of the averaged $p$-point galaxy correlation functions, $\bar{\xi}_p$, up to $p = 6$. The hierarchical amplitudes, $S_p = \bar{\xi}_p / \bar{\xi}_2^{p-1}$, are approximately independent of the cell radius used to smooth the galaxy distribution on small to medium scales. On larger scales we find the higher order moments can be strongly affected by the presence of rare, massive superstructures in the galaxy distribution. The skewness $S_3$ has a weak dependence on luminosity, approximated by a linear dependence on log luminosity. We discuss the implications of our results for simple models of linear and non-linear bias that relate the galaxy distribution to the underlying mass.

## 3.1 Introduction

The pattern of galaxy clustering can be quantified by measuring the galaxy count probability distribution function (CPDF) on a range of smoothing scales. The CPDF gives the probability that a randomly chosen region of the universe will contain a particular number of galaxies, and is typically expressed as a function of both the size of the region smoothed over and the galaxy number within that volume. Traditionally, most effort has been directed at measuring the second moment of the count distribution, the variance, $\bar{\xi}_2$, through the autocorrelation function or, equivalently, its Fourier transform, the power spectrum (e.g. Percival et al. 2001; Padilla & Baugh 2003; Tegmark et al. 2004). The higher order moments of the CPDF, expressed as volume averaged correlation functions, $\bar{\xi}_p$ ($p = 2, 3, \dots$), provide a much more detailed description of galaxy clustering, probing the shape of the low and high count tails of the distribution.

The higher order moments of the dark matter distribution are known to display a hierarchical scaling in which the $p$-point volume averaged correlation functions, $\bar{\xi}_p$, can be written in terms of the variance of the count distribution, $\bar{\xi}_2$: $\bar{\xi}_p = S_p \bar{\xi}_2^{p-1}$ (e.g. see Peebles 1980, Juszkiewicz, Bouchet & Colombi 1993, Bernardeau 1994, Baugh, Gaztañaga

---

& Efstathiou 1995, Gaztañaga & Baugh 1995, Fosalba & Gaztañaga 1998). This scaling is a signature of the evolution under gravitational instability of an initially Gaussian distribution of density fluctuations. A remarkable feature of the scaling is that the values of the hierarchical amplitudes, $S_p$, on scales for which the density field evolves linearly or in a quasi-linear fashion, are insensitive to cosmic epoch and essentially independent of the cosmological density parameter or the value of the cosmological constant. For a comprehensive review of such results see Bernardeau et al. (2002) and references therein.

Departures from the hierarchical scaling of the higher order moments could conceivably arise in three ways:

(i) A strongly non-Gaussian distribution of primordial density waves as could arise, for instance, due to a seed non-linear fluctuation such as a global texture (see Gaztañaga & Mahonen 1996, Gaztañaga & Fosalba 1998, Scoccimarro, Sefusatti & Zaldarriaga 2004 for examples of how the $S_p$ scale in this case). This avenue now seems unlikely, following the clear detection of multiple acoustic peaks in the power spectrum of cosmic microwave background temperature fluctuations (Netterfield et al. 2002; Hinshaw et al. 2003; Mason et al. 2003; Scott et al. 2003; Kuo et al. 2004); such peaks are difficult to reconcile with models that include cosmological defects (Kamionkowski & Kowsowsky 1999). Moreover strongly non-Gaussian primordial fluctuations are ruled out by the first year WMAP results (Komatsu et al. 2003; Gaztañaga & Wagg 2003)

(ii) A weakly non-Gaussian distributed primordial density field, resulting from a non-linear perturbation to a Gaussian density field. This scenario is difficult to distinguish from the evolution of an initially Gaussian field under gravitational instability, because the perturbation can introduce a shift to the amplitudes $S_p$ that is also hierarchical. This can happen even in the case where the non-linear perturbation produces a negligible effect on the power spectrum (Bernardeau et al. 2002).

(iii) The spatial bias between the galaxy distribution and the underlying distribution of dark matter. Fry & Gaztañaga (1993) demonstrated that, under a local biasing prescription, the hierarchical scaling of the higher order moments is preserved but the amplitudes $S_p$ can change as a function of time or luminosity. This conclusion is also reached using more sophisticated, physically motivated semi-analytic models of galaxy formation (Kauffmann et al. 1999; Benson et al. 2000; Scoccimarro et al. 2001).

Previous attempts to measure the higher order correlation functions have been hamstrung by the small size of the available redshift surveys, a shortcoming that is exacerbated once volume limited subsamples are constructed (Hui & Gaztañaga 1999). Nevertheless, early counts-in-cells studies established that the first few higher order moments of the galaxy distribution displayed the hierarchical scaling expected in the gravitational instability framework (Groth & Peebles 1977; Peebles 1980; Gaztañaga 1992; Bouchet et al. 1993; Fry

& Gaztañaga 1994, Ghigna et al. 1996, Feldman et al. 2001). Such analyses were typically limited to measuring the three and four point correlation functions. The nature of the dependence of the hierarchical amplitudes on luminosity has not been convincingly established. Recent work to investigate this in the optical (Hoyle et al. 2000) and in the far infrared (Szapudi et al. 2000) was restricted to probing fairly narrow ranges of luminosity due to the size of the redshift surveys then available.

The advent of multi-fibre spectrographs exploited by sustained observing campaigns has led to a new generation of redshift survey which represents order of magnitude advances over surveys completed in the last millennium. The Sloan Digital Sky Survey (York et al. 2000) and the Two-degree Field Galaxy Redshift Survey (2dFGRS, Colless et al. 2001) have provided maps of the clustering pattern of galaxies with unprecedented detail. Analysis of the 2dFGRS clustering has suggested that the flux limited sample could be an essentially unbiased tracer of the dark matter in the Universe (Lahav et al. 2002; Verde et al. 2002) [2]. These results confirmed previous deductions about galaxy bias (e.g. Gaztañaga 1994, Frieman & Gaztañaga 1999, Gaztañaga & Juszkiewicz 2001) reached using the parent angular catalogue of the 2dFGRS, the APM Galaxy Survey (Maddox et al. 1990, 1996). The 2dFGRS covers a volume that is an appreciable fraction of that sampled by the APM Survey, with full redshift coverage (modulo the relatively small redshift incompleteness that still remains). This means that for the first time, a measurement of the higher order moments is possible in three dimensions with comparable accuracy to that attainable in two dimensions, but without the added complication of the effects of projection (Gaztañaga & Bernardeau 1998; Szapudi & Gaztañaga 1998).

The sheer number of galaxies in the 2dFGRS allows it to be subdivided in order to probe the dependence of the clustering signal on intrinsic galaxy properties in more detail. Norberg et al. (2001) found that the amplitude of the projected two point correlation function scales with luminosity, and characterised this trend using a relative bias factor with a linear dependence on luminosity. In this paper we extend the work of Norberg et al. to study the higher order clustering of galaxies in the 2dFGRS and its dependence on luminosity. Our approach is the same as that followed in Baugh et al. (2004), who measured the higher order correlation functions of a sample of $L_*$ galaxies and found that they follow a hierarchical scaling.

We provide a brief review of the measurement of the moments of the CPDF in Section 3.2. In Section 3.3, we discuss the specific application of this method to the 2dFGRS; an important feature of our analysis is the use of mock catalogues to estimate the errors on our measurements (see Section 3.3.3). Our results for the higher order correlation functions and the hierarchical amplitudes are given in Section 3.4. We quantify the variation of the higher order moments with luminosity in Section 3.5, and discuss the interpretation of these results in terms of a simple relative bias model. Our conclusions are set out in Section 3.6. Throughout, we adopt standard present day values of the cosmological parameters to compute comoving distance from redshift: a density parameter $\Omega_m = 0.3$

---

[2]Note that with the weighting scheme adopted to compensate for the radial selection function, the characteristic luminosity of the flux limited 2dFGRS used in these studies is $\approx 2L_*$.

and a cosmological constant $\Omega_\Lambda = 0.7$.

## 3.2 Counts-in-cells statistics

The count probability distribution function (CPDF) and its moments have been used extensively to quantify the clustering pattern of galaxies (e.g. White 1979; Peebles 1980). In this Section we give an outline of the counts-in-cells approach, explaining how the volume averaged $p$-point correlations are derived from the CPDF and give a brief theoretical background. A more comprehensive discussion of the counts-in-cells approach can be found in Bernardeau et al. (2002).

### 3.2.1 Estimating the $p$-point volume averaged correlation functions

The $p$-point moment, or (un-reduced) correlation function, $m_3(r_1, r_2, r_3) \equiv\; <\delta(r_1)...\delta(r_p)>$, can be used to fully characterise the clustering of a fluctuating field $\delta(r)$. The reduced $p$-point correlation function, $\xi_p(r_1, ..., r_p)$, is defined as the connected part of the above $p$-point correlation in such a way that for $p > 2$: $\xi_p = 0$ for a Gaussian field (see Bernardeau et al. 2002 for more details). Following the standard convention, for the remainder of this paper when we talk about correlations we will always assume they are "reduced" correlations.

The $p$-point *volume averaged* galaxy correlation function, $\bar{\xi}_p(V)$, can be written as the integral of the $p$-point correlation function, $\xi_p$, over the sampling volume, $V$ (Peebles 1980):

$$\bar{\xi}_p(V) = \frac{1}{V^p} \int_V \mathrm{d}^3 r_1 \; \ldots \; \mathrm{d}^3 r_p \, \xi_p(\mathbf{r_1}, \, \ldots \,, \mathbf{r_p}) \, . \tag{3.1}$$

A practical way in which to estimate $\bar{\xi}_p(V)$ is to randomly throw cells down within the galaxy distribution, recording the number of times a cell contains $N$ galaxies so as to build up the galaxy CPDF, $P_N(V)$. Since we adopt spherical cells, the CPDF is a function of the sphere radius, $R$,

$$P_N(R) = \frac{N_N}{N_T} \, , \tag{3.2}$$

where $N_N$ is the number of cells that contain $N$ galaxies out of a total number of cells thrown down, $N_T$. The volume averaged correlation functions $\bar{\xi}_p(V)$ are then related to the moments of the CPDF, $m_p$:

$$m_p(R) = \langle (N - \bar{N})^p \rangle = \sum_{N=0}^{\infty} P_N(R)(N - \bar{N})^p \, , \tag{3.3}$$

where $\bar{N}$ is the mean number of galaxies in a cell of volume $V$ and is calculated directly from the CPDF

$$\bar{N} = \sum_{N=0}^{\infty} N P_N \, . \tag{3.4}$$

For the case of a continuous distribution, $\bar{\xi}_p$ is related to the corresponding cumulant, $\mu_p$, through $\bar{N}^p \bar{\xi}_p = \mu_p$, where the cumulants are defined as (see Gaztañaga 1994 for details):

$$\mu_2 = m_2 \quad ; \quad \mu_3 = m_3 \,,$$

$$\mu_4 = m_4 - 3m_2^2 \quad ; \quad \mu_5 = m_5 - 10m_3m_2 \,. \tag{3.5}$$

If instead we are dealing with a discrete distribution, these relations must be corrected. A Poisson shot noise model is adopted (see Baugh et al. 1995 for a discussion of this point), to give corrected estimates of the moments, $k_p$:

$$k_2 = \mu_2 - \bar{N} \quad ; \quad k_3 = \mu_3 - 3k_2 - \bar{N} \,,$$

$$k_4 = \mu_4 - 7k_2 - 6k_3 - \bar{N} \,,$$

$$k_5 = \mu_5 - 15k_2 - 25k_3 - 10k_4 - \bar{N} \,. \tag{3.6}$$

The volume-averaged correlation functions, calculated from the galaxy CPDF, follow directly from the relation $\bar{\xi}_p = k_p / \bar{N}^p$.

## 3.2.2 Scaling of the higher order moments

In the hierarchical model of clustering, all higher-order correlations can be expressed in terms of the 2-point function, $\bar{\xi}_2$, and dimensionless scaling coefficients, $S_p$:

$$\bar{\xi}_p = S_p \, \bar{\xi}_2^{p-1} \,. \tag{3.7}$$

Traditionally, $S_3 = \bar{\xi}_3 / \bar{\xi}_2^2$ is referred to as the *skewness* of the distribution and $S_4 = \bar{\xi}_4 / \bar{\xi}_2^3$ as the *kurtosis*. The hierarchical scaling of the higher order moments arises from the evolution due to gravitational instability of an initially Gaussian distribution of density fluctuations (see Bernardeau et al. 2002 and references therein).

## 3.2.3 Systematic effects: biased estimators

In addition to sampling errors (see Section 3.3.3 below), the estimation of the hierarchical amplitudes can be compromised by systematic effects, as discussed in some detail by Hui & Gaztañaga (1999). These authors identified two sources of error that could lead to a systematic bias in the inferred values of $S_p$. The first effect arises from biases in the estimates of the higher order correlation functions themselves, known as the "integral constraint bias" (see e.g. Bernstein 1994). The second effect originates in the nonlinear combination of $\bar{\xi}_p$ and $\bar{\xi}_2$ to form $S_p$; this is called the "ratio bias". The latter effect dominates on large scales and tends to cause the inferred values of the $S_p$ to be biased low. Hui & Gaztañaga wrote down expressions for these biases which accurately reproduce the systematic effects seen upon estimating the hierarchical amplitudes from sub-volumes extracted from N-body simulations.

As mentioned above, we will use different volume limited samples to study the luminosity dependence of the hierarchical amplitudes, $S_p$. As the luminosity that defines a sample

is made brighter, the volume of the sample increases. Thus the estimation biases tend to cause the $S_p$ to increase with sample luminosity. This spurious tendency has already been reported in the literature (see Hui & Gaztañaga 1999). For volumes of the size used in our analysis, it turns out that the predicted biases are smaller than the corresponding sampling errors (e.g. see figure 3 in Hui & Gaztañaga 1999). This is the first time that a redshift survey has been available which is large enough to overcome such systematic biases.

### 3.2.4 Galaxy biasing

Galaxy samples constructed using different selection criteria display different clustering patterns. This leads one to the conclusion that distinct samples of galaxies must trace the underlying mass distribution in different ways, a phenomenon that is generally known as galaxy bias.

A simple, heuristic scheme describing the impact of a local bias on the scaling of the higher order moments was proposed by Fry & Gaztañaga (1993). These authors demonstrated that in this case, the scaling of the higher order moments of the galaxy distribution should mirror that of the dark matter, though possibly with different values for the hierarchical amplitudes $S_p$. Fry & Gaztañaga made the assumption that the density contrast in the galaxy distribution, $\delta^{\mathrm{G}}$, i.e. the fractional fluctuation around the mean density, could be written as a Taylor expansion of the density contrast of the dark matter, $\delta^{\mathrm{DM}}$:

$$\delta^{\mathrm{G}} = \sum_{k=0}^{\infty} \frac{b_k}{k!} (\delta^{\mathrm{DM}})^k. \tag{3.8}$$

On scales where the variance, $\bar{\xi}_2^{\mathrm{DM}}$, is small, the leading order contribution to the two-point volume averaged correlation function of galaxies has the form:

$$\bar{\xi}_2^{\mathrm{G}} = b_1^2 \, \bar{\xi}_2^{\mathrm{DM}}, \tag{3.9}$$

where $b_1$ is the ubiquitous linear bias $b$. The leading order forms for the hierarchical amplitudes, $S_p$, for the cases $p = 3$ and $p = 4$ are:

$$S_3^{\mathrm{G}} = \frac{1}{b_1} \left( S_3^{\mathrm{DM}} + 3c_2 \right) \tag{3.10}$$

$$S_4^{\mathrm{G}} = \frac{1}{b_1^2} \left( S_4^{\mathrm{DM}} + 12c_2 S_3^{\mathrm{DM}} + 4c_3 + 12c_2^2 \right), \tag{3.11}$$

where we use the notation $c_k = b_k/b_1$. Expressions for the hierarchical amplitudes are given up to $p = 7$ in Fry & Gaztañaga (1993).

Mo, Jing & White (1997) give theoretical predictions for the coefficients $b_k$ using the Press & Schechter (1974) formalism and exploiting the framework developed by Cole & Kaiser (1989) and Mo & White (1996). For halos of mass $M$, the first two bias factors

($k = 1$ and 2) are given by:

$$b_1 = 1 + \frac{v^2 - 1}{\delta_c} \tag{3.12}$$

$$b_2 = 2\left(1 - \frac{17}{21}\right)\frac{v^2 - 1}{\delta_c} + \frac{v^2}{\delta_c^2}(v^2 - 3) \tag{3.13}$$

where $v \equiv \delta_c/\sigma(M)$, $\delta_c$ is the linear theory overdensity at the time of collapse ($\delta_c = 1.686$ for $\Omega = 1$) and $\sigma(M)$ is the linear *rms* fluctuation on the mass scale of the halos. This is a simple model but nevertheless it shows some tendencies that are correct. For example, a typical mass halo corresponding to $v = 1$ displays an unbiased variance with $b_1 = 1$, but introduces a bias in the skewness, since $c_2 = b_2 = -0.7$. As a further illustration, consider massive halos defined by $v^2 > 3$; in this case the Mo, Jing & White theory predicts that $c_2 > 0$, while less massive halos could produce $c_2 < 0$. To get more realistic values of $b_k$ for galaxy bias, a prescription has to be adopted for populating dark matter halos of a given mass with galaxies of a given luminosity (Benson et al. 2001; Scoccimarro et al. 2001; Berlind et al. 2003).

In the interpretation of the higher order moments presented in this paper we will make use of a *relative* bias, which describes the change in clustering compared with that measured for a reference sample (Norberg et al. 2001, 2002a). Using Eq. 3.9 as a guide, we define the relative bias, $b_r = b_1/b_1^*$, of a sample as the square root of the ratio of the 2-point correlation function measured for the sample over that measured for the reference sample, denoted by an asterisk (the reference sample will be defined explicitly in Section 3.5):

$$b_r \equiv \frac{b_1}{b_1^*} = \left(\frac{\bar{\xi}_2^G}{\bar{\xi}_2^{G*}}\right)^{1/2}. \tag{3.14}$$

Thus, we can obtain an estimate of the relative bias from the ratio of the variances.

When the linear bias is a good approximation ($c_k \simeq 0$ for $k > 1$), we can relate $S_p^G$ in different galaxy samples regardless of the underlying DM value of $S_p$:

$$S_p^G = \frac{S_p^{G*}}{b_r^{p-2}}. \tag{3.15}$$

More generally, one can manipulate Eq. 3.10 to write down an expression comparing $S_p^G$ for two galaxy samples, eliminating $S_3^{DM}$ for the underlying dark matter (e.g. see Eq. 9 in Fry & Gaztañaga 1993). For the skewness:

$$S_3^{G*} = b_r S_3^G - 3\frac{(c_2 - c_2^*)}{b_1^*}, \tag{3.16}$$

where an asterisk denotes a quantity describing the reference sample, and $b_r = b_1/b_1^*$ is the relative bias defined above. Any second order relative bias effects are thus given by:

$$c_2' = \frac{(c_2 - c_2^*)}{b_1^*} = \frac{1}{3}\left(b_r S_3^G - S_3^{G*}\right). \tag{3.17}$$

As a special case, if the reference sample is un-biased (i.e. $b_1^* = 1$ and $c_p^* = 0$), we then have $c_2' = c_2$.

## 3.3 Application to the 2dFGRS

In this Section we describe the construction of volume limited samples from the 2dFGRS (Section 3.3.1) and outline how we deal with the small, remaining incompleteness of the survey when we measure the CPDF (Section 3.3.2). The estimation of errors on the measured higher order moments is described in Section 3.3.3. We use the full 2dFGRS as our starting point. The final spectra were taken in April 2002, giving a total of 221,414 galaxies with high quality redshifts (i.e. with quality flag $Q \geq 3$; see Colless et al. 2001). The median depth of the full survey, to a nominal magnitude limit of $b_J \sim 19.45$, is $z \sim 0.11$. We consider the two large contiguous survey regions, one near the south galactic pole (SGP) and the other towards the north galactic pole (NGP). After restricting attention to the high redshift completeness parts of the survey (see Colless et al. 2001; Norberg et al. 2002b), the effective solid angle covered by the NGP region is 469 square degrees and that of the SGP is 670 square degrees. Full details of the 2dFGRS and the construction and use of the mask quantifying the completeness of the survey can be found in Colless et al. (2001, 2003).

We make use of mock 2dFGRS catalogues to test our algorithm for dealing with the spectroscopic incompleteness of the survey and to estimate errors on the measured higher order correlation functions. The construction of the mocks is described in Norberg et al. (2002b). In short, catalogues are extracted from the Virgo Consortium's $\Lambda$CDM Hubble Volume simulation which covers a volume of $27\text{Gpc}^3$ (Evrard et al. 2002). A heuristic bias scheme is applied to the smoothed distribution of dark matter in the simulation to select 'galaxies' with a specified clustering pattern (Cole et al. 1998). The parameters of the biasing scheme are adjusted so that the extracted galaxies have the same projected correlation function as measured for the flux limited 2dFGRS by Hawkins et al. (2003). Observers are placed within the Hubble Volume simulation according to the criteria set out in Norberg et al. (2002b). Mock catalogues are then extracted by applying the radial and angular selection functions of the 2dFGRS. Finally, the mock is degraded from uniform coverage within the angular mask of the survey by applying the spectroscopic completeness mask of the 2dFGRS.

### 3.3.1 Construction of volume limited catalogues

In a flux limited sample the density of galaxies is a strong function of radial distance. This effect needs to be taken into account in clustering analyses (for an example of a technique appropriate to a counts-in-cells analysis, see Efstathiou et al. 1990). Alternatively, one may construct volume limited samples in which the radial selection function is constant and any variations in the density of galaxies are due only to large scale structure. This greatly simplifies the analysis at the expense of using a subset of the survey galaxies. The

| VLC ID | Mag. range $M_{b_J} - 5\log_{10}h$ | | Median lum. $L/L_*$ | $N_G$ | $\rho_{ave}$ $10^{-3}h^3\mathrm{Mpc}^{-3}$ | $d_{mean}$ $h^{-1}\mathrm{Mpc}$ | $z_{min}$ | $z_{max}$ | $D_{min}$ $h^{-1}\mathrm{Mpc}$ | $D_{max}$ $h^{-1}\mathrm{Mpc}$ | Volume $10^6 h^{-3}\mathrm{Mpc}^3$ |
|---|---|---|---|---|---|---|---|---|---|---|---|
| 1 | −17.0 | −18.0 | 0.13 | 8038 | 10.9 | 4.51 | 0.009 | 0.058 | 24.8 | 169.9 | 0.74 |
| 2 | −18.0 | −19.0 | 0.33 | 23290 | 9.26 | 4.76 | 0.014 | 0.088 | 39.0 | 255.6 | 2.52 |
| 3 | −19.0 | −20.0 | 0.78 | 44931 | 5.64 | 5.62 | 0.021 | 0.130 | 61.1 | 375.6 | 7.97 |
| 4 | −20.0 | −21.0 | 1.78 | 33997 | 1.46 | 8.82 | 0.033 | 0.188 | 95.1 | 537.2 | 23.3 |
| 5 | −21.0 | −22.0 | 3.98 | 6895 | 0.110 | 20.9 | 0.050 | 0.266 | 146.4 | 747.9 | 62.8 |

**Table 3.1:** Properties of the combined 2dFGRS SGP and NGP volume-limited catalogues (VLCs). Column 1 gives the numerical label of the sample. Columns 2 and 3 give the faint and bright absolute magnitude limits that define the sample. The fourth column gives the median luminosity of each volume limited sample in units of $L_*$, computed using the Schechter function parameters quoted by Norberg et al. (2002b). Columns 5, 6 and 7 give the number of galaxies, the mean number density and the mean inter-galaxy separation for each VLC, respectively. Columns 8 and 9 state the redshift boundaries of each sample for the nominal apparent magnitude limits of the survey; columns 10 and 11 give the corresponding comoving distances. Finally, column 12 gives the combined SGP and NGP volume. All distances are comoving and are calculated assuming standard cosmological parameters ($\Omega_m = 0.3$ and $\Omega_\Lambda = 0.7$).

2dFGRS contains enough galaxies and covers sufficient volume to permit the construction of volume limited samples corresponding to a wide baseline in luminosity from which robust measurements of the higher order correlation functions can be obtained.

We follow the approach taken by Norberg et al. (2001, 2002a) who measured the projected 2-point correlation function of 2dFGRS galaxies in volume limited samples corresponding to bins in absolute magnitude. The samples are defined by a specified absolute magnitude range, with absolute magnitudes corrected to zero redshift (this correction is made using the $k + e$ correction given by Norberg et al. 2002b). As any survey has, in practice, a bright as well as a faint flux limit, this implies that a selected galaxy should fall between a minimum ($z_{min}$) and a maximum ($z_{max}$) redshift. This then guarantees that all sample galaxies are visible within the flux limits of the survey when displaced to any depth within the volume of the sample. The properties of the combined NGP and SGP volume limited samples examined in this paper are given in Table 3.1.

### 3.3.2 Correcting for incompleteness

There are two possible sources of incompleteness that need to be considered when estimating the galaxy count within a cell. The first is volume incompleteness, which can arise when some fraction of the cell volume samples a region of space that is not part of the 2dFGRS. This situation can arise because the survey has a complicated boundary and also because it contains holes excised around bright stars and other interlopers in the parent APM galaxy catalogue (Maddox et al. 1990, 1996). The second source of incompleteness is spectroscopic incompleteness. The final 2dFGRS catalogue is much more homogeneous than the 100k release (contrast the completeness mask of the final survey shown in figure 1 of Hawkins et al. 2003 with the equivalent mask depicted in figure 15 of Colless et al. 2001.) However, the spectroscopic completeness still varies with position on the sky and needs to be incorporated into the counts-in-cells analysis.

It is therefore necessary to devise a strategy to compensate for the fact that a cell will sample regions that have varying spectroscopic completeness and which may even straddle the survey boundary or a hole. We project the volume enclosed by the cell onto the sky and estimate, using the survey masks, the mean combined spectroscopic and volume completeness, $f$, within the sphere. Rather than view the consequence of this incompleteness as missed galaxies, we instead consider it as missed *volume*. We compute a new radius for the sphere given by $R' = f^{-\frac{1}{3}}R$: such a sphere with radius $R'$ will have an incomplete volume equivalent to that of a fully complete sphere of radius $R$. Spheres for which $f$ is less than 50% are discarded. The galaxy count within the sphere of radius $R'$ then contributes to the CPDF at the effective radius $R$. Each sphere thrown down is individually scaled in this way according to its local incompleteness, as given by the survey masks. We note that, due to our chosen acceptable minimum completeness of 50%, the rescaling of the cell radius is always less than the width of the radial bins we use to plot the higher order correlation functions. Our results are insensitive to the precise choice of completeness threshold.

An alternative method to correct cell counts is described in Efstathiou et al. (1990). In

34
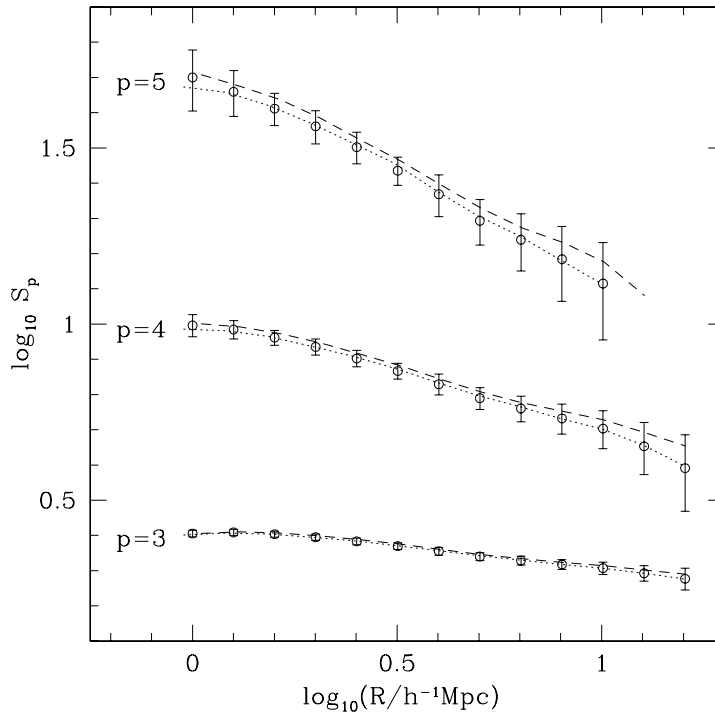
**Figure 3.1:** A test of the scheme used to correct the measured distribution of counts-in-cells for incompleteness in the 2dFGRS, using mock catalogues. The plot shows the hierarchical amplitudes, $S_p$, for orders $p = 3, 4$ and 5. The dotted lines show the results from fully sampled mocks that have no incompleteness. The dashed lines show how these results change when the completeness mask of the 2dFGRS is applied to the mocks and *no* compensation is made for the variable spectroscopic completeness. The circles show the $S_p$ recovered once the correction to the cell radius discussed in the text is made. The errorbars show the *rms* scatter estimated from the mock catalogues.

this commonly used approach it is the galaxy *counts* which are scaled up in proportion to the degree of incompleteness in the cell, as opposed to the cell volume as we have done. We have tried both correction methods when calculating the higher order moments and find the results are essentially identical (see Croton et al. 2004b for further discussion of the relative strengths and weaknesses of both methods).

A test of our method for dealing with incompleteness is shown in Fig. 3.1. This plot shows the $S_p$ estimated from the higher order correlation functions measured in mock 2dFGRS catalogues (Norberg et al. 2002b). The dotted lines show the results for complete mocks, with uniform sampling of the galaxy distribution within the full angular boundary of the 2dFGRS. The dashed lines show how these results change once the mocks are

degraded to mimic the spectroscopic incompleteness and irregular geometry of the 2dF-GRS, without applying any correction to compensate for this incompleteness. The circles show the values of $S_p$ recovered on application of the correction for incompleteness described above. These results are in excellent agreement with those from the fully sampled, 'perfect' mocks.

We have carried out two independent counts-in-cells analyses, using different algorithms to place cells within the survey volume. The results are insensitive to the details of the counts-in-cells algorithm. The CPDF is measured using $2.5 \times 10^7$ cells for each cell radius. We have further checked the counts in cells analysis by comparing the measured two point volume averaged correlation function with the integral of the measured spatial two point correlation function, given by Eq. 3.1; the integral of the spatial correlation function is in very good agreement with the direct estimate of the volume averaged correlation function.

### 3.3.3 Error estimation

We estimate the error on the higher order correlation functions and hierarchical amplitudes using the set of 22 mock 2dFGRS surveys described by Norberg et al. (2002b). The $1\sigma$ errors that we show on plots correspond to the *rms* scatter over the ensemble of mocks (see Norberg et al. 2001a). To recap, we consider one of the mocks as the "data" and compute the variance around this "mean" using the remaining mock catalogues. This process is repeated for each mock in turn, and the *rms* scatter is taken as the mean variance. We illustrate this approach in Fig. 3.2 for the case of $p = 3$, for a volume defined by the magnitude range $-19 > M_{b_J} - 5\log_{10} h > -20$. In the upper panel, the skewness or $S_3$ measured in each mock is shown by the dotted lines. The points show the mean skewness averaged over the ensemble of 22 mocks. The errorbars show the *rms* scatter on these measurements. The lower panel shows the fractional error that we expect on the measurement of $S_3$ for this particular volume limited sample. Beyond $20h^{-1}$Mpc, the fractional error increases rapidly. Our estimate of the fractional error automatically includes the contribution from sampling variance due to large scale structure (sometimes referred to as "cosmic variance"). To estimate the error on a measured correlation function, we simply compute the fractional *rms* scatter for the equivalent volume limited sample using the ensemble of mocks, and multiply the measured quantity by the fractional error.

We have compared the estimate of the *rms* scatter from the ensemble of mocks with an internal estimate using a jackknife technique (see, for example, Zehavi et al. 2002). In the jackknife approach, the survey is split into subsamples. The error is then the scatter between the measurements when each subsample is omitted in turn from the analysis. The jackknife gives comparable errors to the mock ensemble for low order moments. On large scales, the higher order moments are particularly sensitive to sample variance and, in these cases, the jackknife approach can only provide a lower bound to the true scatter.

A more formal error estimation procedure is adopted when computing the best fit values for the hierarchical amplitudes, $S_p$. In this case, we employ a principal component analysis to explicitly take into account the correlations between the $S_p$ inferred at different cell radii (see e.g. Porciani & Giavalisco 2002 and Section 6 of Bernardeau et al. 2002). The mock
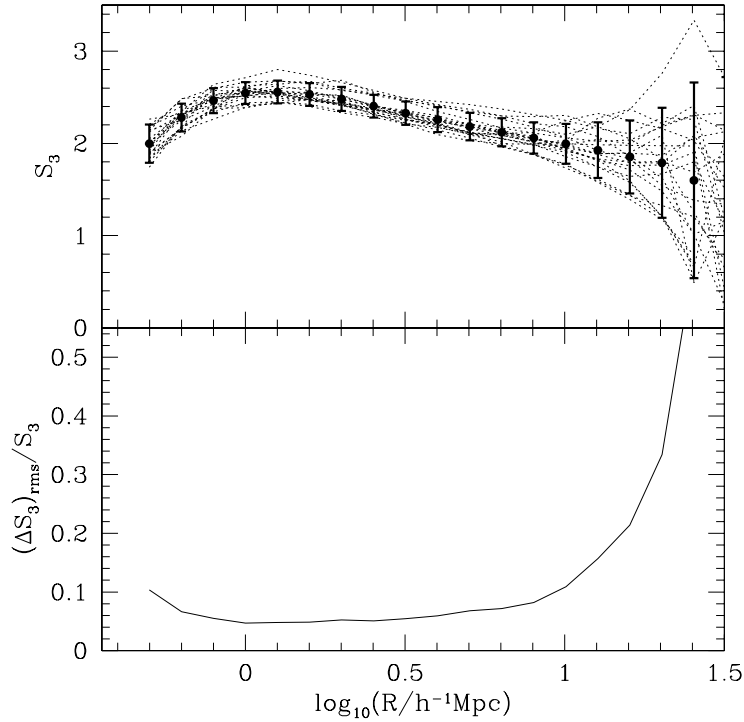
**Figure 3.2:** The upper panel shows the skewness, $S_3$, recovered from mock 2dFGRS
catalogues in volume limited samples defined by the magnitude range $-19 >$
$M_{b_J} - 5 \log_{10} h > -20$. The dotted lines show the skewness measured in each
catalogue. The points show the mean skewness. The errorbars show the
mean *rms* scatter averaged over 22 mocks, as described in the text in Section
3.3.3. The lower panel shows the fractional error as a function of cell radius.
This panel shows how well we can expect to measure the skewness in a
catalogue of this size extracted from the 2dFGRS, including the contribution
from sampling variance.

catalogues are used to compute the full covariance matrix of the $S_p$ data points to be fitted.
Next, the eigenvalues and eigenvectors of the covariance matrix are determined. We find
that, typically, the first few eigenvectors are responsible for over 90% of the variance.
Given the number of data points that we consider in the fits, this means that we have
around a factor of two to three times fewer independent points than data points fitted.
(Details of the range of scales used in the fits will be given in Section 3.4.2.) We note
that in most previous work, the $S_p$ measured at different cell radii were simply averaged
together ignoring *any* correlations between bins, resulting in unrealistically small errors in
the fitted values.

37
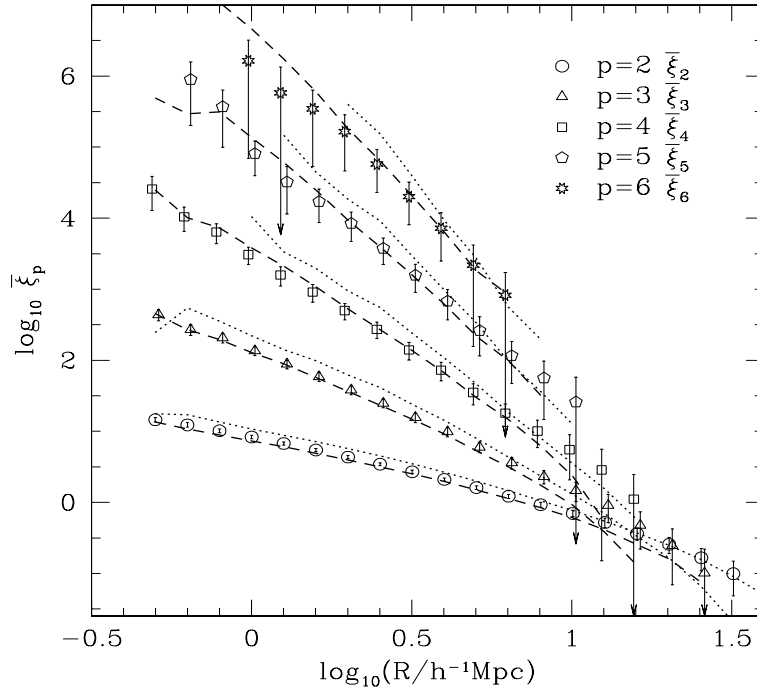
**Figure 3.3:** The higher order correlation functions measured for 2dFGRS galaxies. The symbols show the measurements for galaxies in the absolute magnitude range $-19 > M_{b_J} - 5\log_{10} h > -20$; the key gives the order $p$. The lines show the results for different luminosity samples; the dashed lines show the $\bar{\xi}_p$ for galaxies with $-18 > M_{b_J} - 5\log_{10} h > -19$ and the dotted lines show the results for galaxies with $-20 > M_{b_J} - 5\log_{10} h > -21$.

## 3.4  Results

### 3.4.1  Volume-averaged correlation functions

The volume averaged correlation functions estimated from the CPDF constructed from the combined NGP and SGP cell counts are plotted in Fig. 3.3. The symbols show the correlation functions for the $L_*$ sample with $-19 > M_{b_J} - 5\log_{10} h > -20$. The lines show the measurements made for galaxies in magnitude bins adjacent to $L_*$ (the dashed lines correspond to a sample that is one magnitude fainter and the dotted lines to a sample that is one magnitude brighter). The correlation functions steepen dramatically on small scales as the order $p$ increases.

To better quantify the dependence of the higher order correlation functions on luminosity, we plot the ratio of the $\bar{\xi}_p$ to the results for the $L_*$ reference sample in Fig. 3.4, for
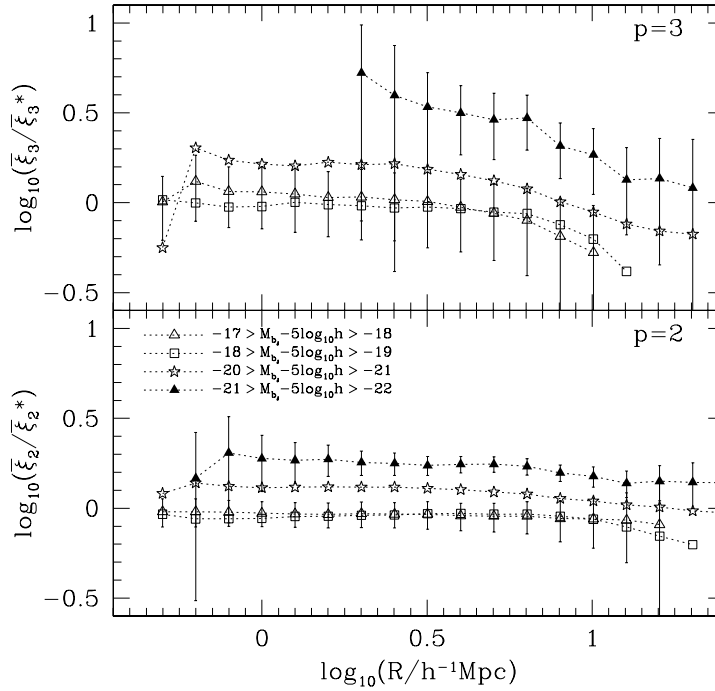
**Figure 3.4:** The dependence of the higher order correlation functions on luminosity. The orders $p = 3$ (top panel) and $p = 2$ (bottom panel) are shown. The correlation functions for samples of different luminosity are divided by the correlation function measured for $L_*$ galaxies, with $-19 > M_{b_J} - 5\log_{10} h > -20$.

the cases $p = 2$ and $p = 3$. The variance in the distribution of counts-in-cells on a given smoothing scale increases with the luminosity of the volume limited sample (see the bottom panel of Fig. 3.4). This effect is similar to that reported by Norberg et al. (2001, 2002a), who measured the dependence of the strength of galaxy clustering on luminosity in real space, whereas our results are in redshift space. This behaviour is broadly seen to extend to the higher order clustering, however the ranking of the amplitude of the higher order correlation functions with luminosity is not always preserved on large scales. This issue is investigated further in Section 3.4.3.

## 3.4.2 Hierarchical clustering

We use the measured volume averaged correlation functions from Fig. 3.3 to test the hierarchical clustering model set out in Section 3.2.2 and Eq. 3.7. In Fig. 3.5, we plot the $p = 3$–6 point volume averaged correlation functions as a function of the variance (or two-point function) measured on the same scale. Small values of the moments correspond
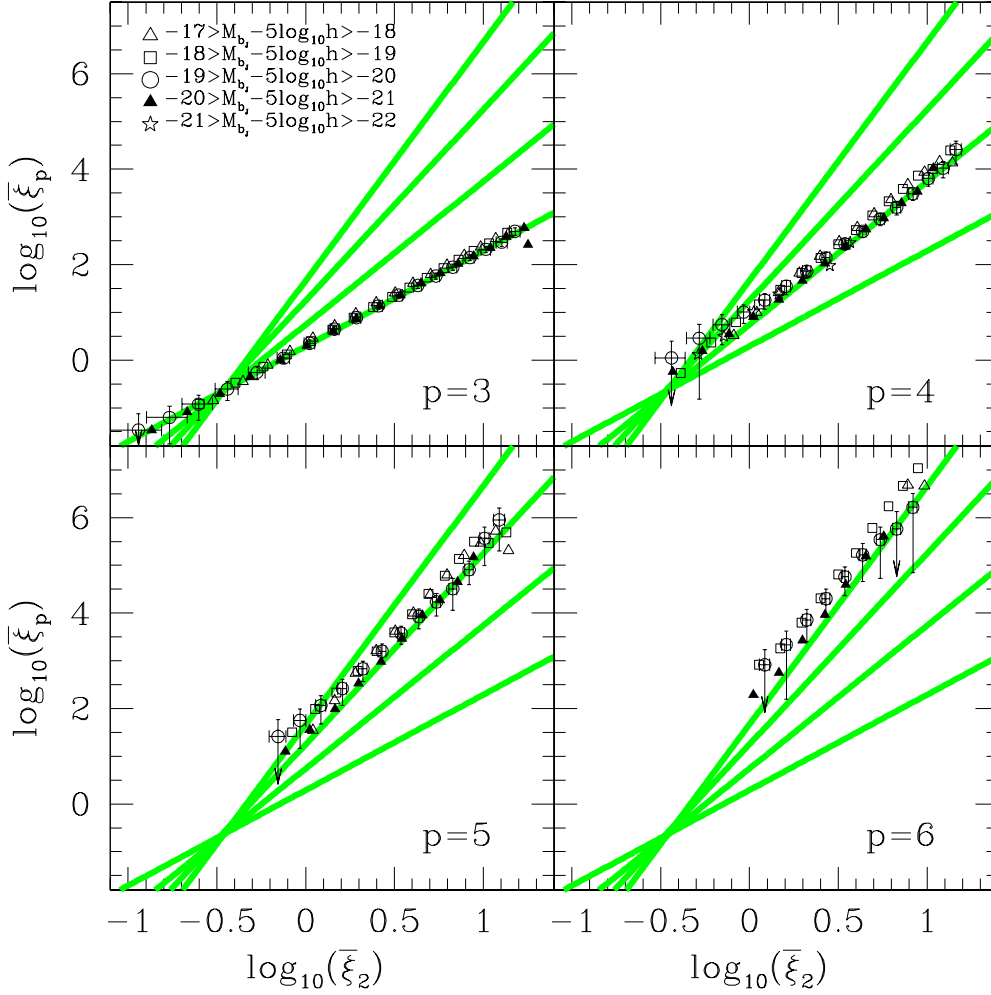
**Figure 3.5:** The volume averaged correlation functions, $\bar{\xi}_p$, for $p$ = 3 to 6, plotted as a function of the variance, $\bar{\xi}_2$. Each panel corresponds to a different order plotted on the ordinate, as indicated by the legend. (Note that $\bar{\xi}_5$ and $\bar{\xi}_6$ are not plotted for the brightest sample, as they are too noisy.) The symbols refer to different magnitude ranges as given by the key in the first panel. The line styles denote the results for different absolute magnitude ranges, as indicated by legend. The thick grey lines show power-laws with slopes of 2, 3, 4 and 5 in order of increasing amplitude, which are intended to act as a reference.
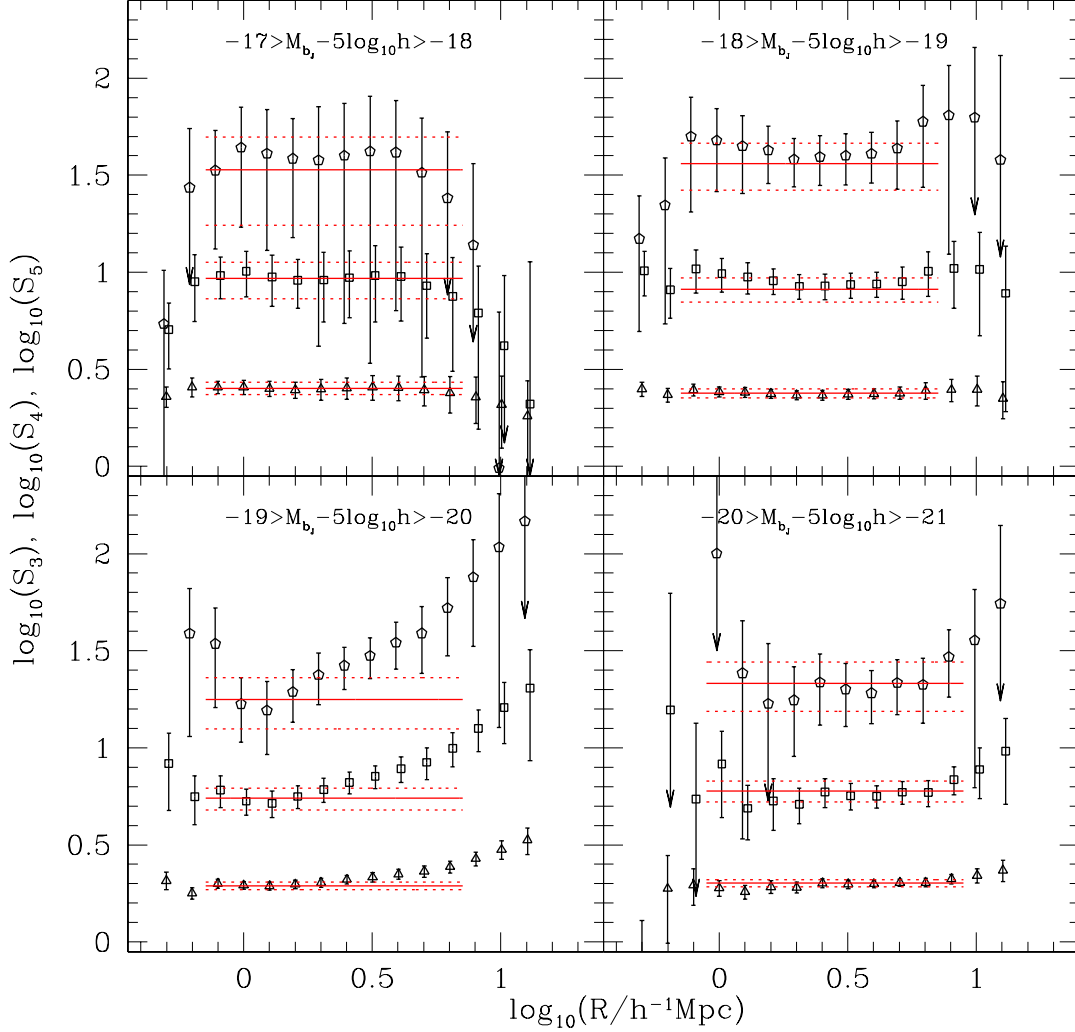
**Figure 3.6:** The hierarchical amplitudes, $S_p$, for $p = 3, 4$ and $5$, plotted as a function of cell radius for the galaxy samples defined in Table 3.1. Each panel shows the results for a different volume limited catalogue, as indicated by the legend. The points with errorbars show the results obtained from the full volume limited samples: triangles show $S_3$, squares show $S_4$ and pentagons show $S_5$. The solid lines show the best fit values and the dotted lines indicate the $1\sigma$ errors on the fits, as described in the text. The lines are plotted over the range of scales used in the fits.

41

to large cells. The thick grey lines show the higher order moments expected in the hierarchical model. (From Eq. 3.7, the offsets of these lines are the hierarchical amplitudes $S_p$. We have used the best fit values of $S_p$ that we obtain later on in this Section. However, the width of the lines does not indicate the error on the fit: the lines are intended merely to guide the eye.) On small scales (large variances), hierarchical scaling is followed. On intermediate and large scales, for which the variance drops below $\sim 1.3$, the measured moments depart somewhat from the hierarchical scaling behaviour, particularly in the case of the higher orders.

The hierarchical scaling of the higher order correlation functions is exploited to plot the hierarchical amplitudes $S_p = \bar{\xi}_p / \bar{\xi}_2^{p-1}$ as a function of cell radius in Fig. 3.6. Each panel corresponds to a different volume limited sample, where the lines and points correspond to $S_3$, $S_4$ and $S_5$ in order of increasing amplitude. The hierarchical amplitudes measured from the two brightest volume limited samples systematically show an increase around $10h^{-1}$Mpc. This effect is particularly significant in the $-19 > M_{b_J} - 5\log_{10} h > -20$ sample, with the $S_p$ increasing by a factor of 2 to 5 depending on $p$. On smaller scales the hierarchical amplitudes are essentially independent of the cell radius for all magnitude ranges considered. It should be noted that the $S_p$ measured in real space vary more strongly in amplitude with scale than in redshift space, particularly at small cell radii (Gaztañaga 1994; Szapudi et al. 1995, Szapudi & Gaztañaga 1998).

We have fit constant values to the measured $S_p$, using the principal component analysis outlined in Section 3.3.3. This approach takes into account the correlations between the measurements on different scales. The range of scales used to fit $S_p$ is held fixed for each volume limited sample and is quoted in Table 3.2. Typically, there are ten values of $S_p$ in the range considered in the fits. The principal component analysis reveals that just $2 - 4$ linear combinations of these points account for more than 90% of the variance; this gives a fairer impression of the number of independent data points. The principal eigenvector is in all cases almost independent of scale, i.e. its effect is to move all the points coherently up and down (driven by large scale variation in the mean density estimated from the survey). Therefore, the best fitting constant tends to favour a fit either slightly above or below each set of data points. This is exactly what is seen in the various panels of Fig. 3.6. The best fit constants to the measured $S_p$ are given in Table 3.2, along with an error from the principal component analysis. The fits to $S_3$ and $S_4$ for the $-19 > M_{b_J} - 5\log_{10} h > -20$ sample are poor in terms of the reduced $\chi^2$. There some dependence of the $S_p$ with increasing luminosity. This behaviour is explored in Section 3.5.

### 3.4.3 Systematic effects: the influence of superclusters

The higher order moments of the CPDF are sensitive to the presence of massive structures that contribute to the extreme event tail of the count distribution. It is therefore important to examine the 2dFGRS to look for any rare large scale structures that could exert a significant influence on the form of the CPDF. The projected density of galaxies in the right ascension-redshift plane for a volume limited catalogue defined by the magnitude range $-19 > M_{b_J} - 5\log_{10} h > -20$ is plotted in figure 1 of Baugh et al. (2004). There are two clear hot spots

| VLC ID | $R_{\min}$ $h^{-1}$Mpc | $R_{\max}$ $h^{-1}$Mpc | $S_3$ | $S_4$ | $S_5$ | $S_6$ | $b_r$ | $c'_2$ |
|---|---|---|---|---|---|---|---|---|
| 1 | 0.71 | 7.1 | $2.58 \pm 0.37\,(0.1)$ | $9.3 \pm 4.0\,(0.1)$ | $34 \pm 32\,(0.1)$ | $-\,-\,-$ | $0.96 \pm 0.16\,(0.1)$ | $0.17 \pm 0.25\,(0.1)$ |
| 2 | 0.71 | 7.1 | $2.38 \pm 0.25\,(0.1)$ | $8.2 \pm 2.3\,(0.9)$ | $36 \pm 20\,(0.4)$ | $185 \pm 170(0.1)$ | $0.96 \pm 0.08\,(0.3)$ | $0.11 \pm 0.13\,(0.1)$ |
| 3 | 0.71 | 7.1 | $1.95 \pm 0.18\,(6.1)$ | $5.5 \pm 1.4\,(2.3)$ | $18 \pm 11\,(1.9)$ | $46 \pm 50(1.1)$ | $1$ | $0$ |
| 4 | 0.80 | 8.9 | $2.01 \pm 0.17\,(1.2)$ | $6.0 \pm 1.5\,(0.6)$ | $22 \pm 12\,(0.4)$ | $71 \pm 80(0.3)$ | $1.13 \pm 0.06\,(2.8)$ | $0.10 \pm 0.08\,(0.3)$ |
| 5 | 2.2 | 11.2 | $2.39 \pm 0.63\,(0.5)$ | $6.8 \pm 7.0\,(0.4)$ | $-\,-\,-$ | $-\,-\,-$ | $1.30 \pm 0.14\,(0.9)$ | $0.33 \pm 0.31\,(0.5)$ |

**Table 3.2:** The best fit values and $2-\sigma$ error ($\Delta\chi^2 = 4$) for $S_p$ (columns 4 to 7). The range of scales used in the fits is given in columns 2 and 3. The number in brackets after each error gives the reduced $\chi^2$ value for the fit, using the number of degrees of freedom derived from the principal component analysis. The last two columns give the relative linear bias, $b_r$ (defined by Eq. 3.14) and the second order bias term, $c'_2$ (defined by Eq. 3.17). The reference sample is sample number 3. These values are obtained for the full volume limited samples. A blank entry indicates that a reliable measurement of the particular hierarchical amplitude was not possible for the sample in question.

or superstructures apparent in this figure, one in the NGP at a redshift of $z = 0.08$ and a right ascension of 3.4 hours, and the other in the SGP at $z = 0.11$ at a right ascension of 0.2 hours. These structures are confirmed as superclusters of galaxies in the group catalogue constructed from the flux limited 2dFGRS (Eke et al. 2004); of the 94 groups in the full flux limited survey out to $z \sim 0.15$ with 9 or more members and estimated masses above $5 \times 10^{14} h^{-1} M_{\odot}$, 20% reside in these superclusters. As a result of the redshift at which these superclusters lie, these structures are only influential in volume limited samples brighter than $M_{b_J} - 5 \log_{10} h = -18$.

The results presented earlier in this Section show features that could be due to the presence of these superclusters. For example, the volume averaged correlation functions for the $-19 > M_{b_J} - 5 \log_{10} h > -20$ sample plotted in Fig. 3.3 appear to have more power on large scales than those measured from the other volume limited samples. This is consistent with the theoretical expectations for measurements that are strongly affected by the presence of a supercluster: a boost in the clustering amplitude on large scales, due to a structure with a larger bias, and a reduction in the clustering amplitude on small scales arising from the large velocity dispersions within the clusters making up the structure.

To investigate this hypothesis, we have carried out the test of removing the two superclusters from the sample and recomputing the volume averaged correlation functions. The goal of this exercise is not to "correct" the measured correlation functions but rather to illustrate the impact of the superclusters on our results. We remove the superclusters by masking out their central densest regions, corresponding to prohibiting the placement of cells within a sphere of radius $25 h^{-1}$Mpc from each supercluster centre (for a different approach on how to take this type of effect into account see Colombi, Bouchet & Schaeffer 1994 and Fry & Gaztañaga 1994).

Fig. 3.7 shows the effect of the supercluster removal on the tail of the CPDF for $10 h^{-1}$Mpc radius cells, calculated for three volume limited catalogues centred on $L^*$. The mean number of galaxies in a cell for each galaxy sample is roughly 40, 24, and 6 going from faintest to brightest. The presence of the two superclusters makes a clear difference to the high $N$ counts for galaxy samples brighter than $M_{b_J} - 5 \log_{10} h = -19$. The maximum redshift of the faint volume limited catalogue in this figure only marginally includes the NGP supercluster, and so $P_N$ remains essentially unaffected in this case.

Fig. 3.8 shows volume averaged correlation functions of order $p = 2, 3, 4$ for three volume limited catalogues from Table 3.1, where each panel corresponds to a fixed absolute magnitude range. The lines correspond to different orders of clustering, starting with the lowest in amplitude, the two point volume averaged correlation function, and moving through to the four point function, at which we stop plotting the results for clarity although the trends shown continue up to sixth order. The solid curves show the correlation functions measured from the full volume limited samples, as shown previously in Fig. 3.6, and the dashed lines show the results when the regions containing the superclusters are excluded from the CPDF. The higher order correlation functions are systematically boosted on intermediate and large scales when the superclusters are included in the analysis. The precise scale on which the correlation functions become sensitive to the presence of the superclusters depends upon the order; for the four point function, the two estimates of the
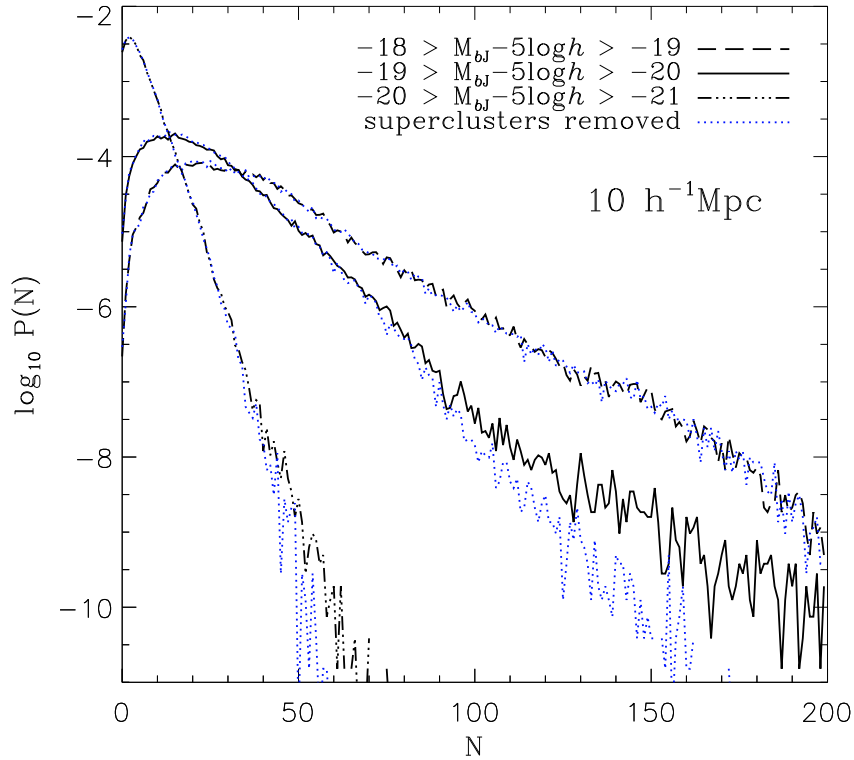
**Figure 3.7:** The probability, $P_N$, of finding exactly $N$ galaxies in randomly placed cells of radius $10h^{-1}$Mpc (the CPDF, Eq. 3.2), for different volume limited galaxy samples. Each bold line shows the full volume CPDF, while the individual dotted lines give the result after the supercluster regions have been omitted from the analysis, as described in Section 3.4.3.

correlation function typically deviate for cells of radius $3h^{-1}$Mpc and larger.

The impact on the hierarchical amplitudes, $S_p$, of removing the superclusters in shown in Fig. 3.9, in which we plot the results for the volume limited sample defined by $-19 > M_{b_J} - 5\log_{10} h > -20$. In Fig. 3.9, the open points show the hierarchical amplitudes measured from the full volume limited sample. The filled symbols show the results obtained from the same volume but with the supercluster regions masked out. The $S_p$ obtained when the two superclusters are removed from the analysis are much closer to being independent of cell size. The sensitivity of higher orders to rare peaks has been noticed in earlier analyses of galaxy surveys (Groth & Peebles 1977; Gaztañaga 1992; Bouchet et al. 1993; Lahav et al. 1993; Gaztañaga 1994; Hoyle et al. 2000).

45
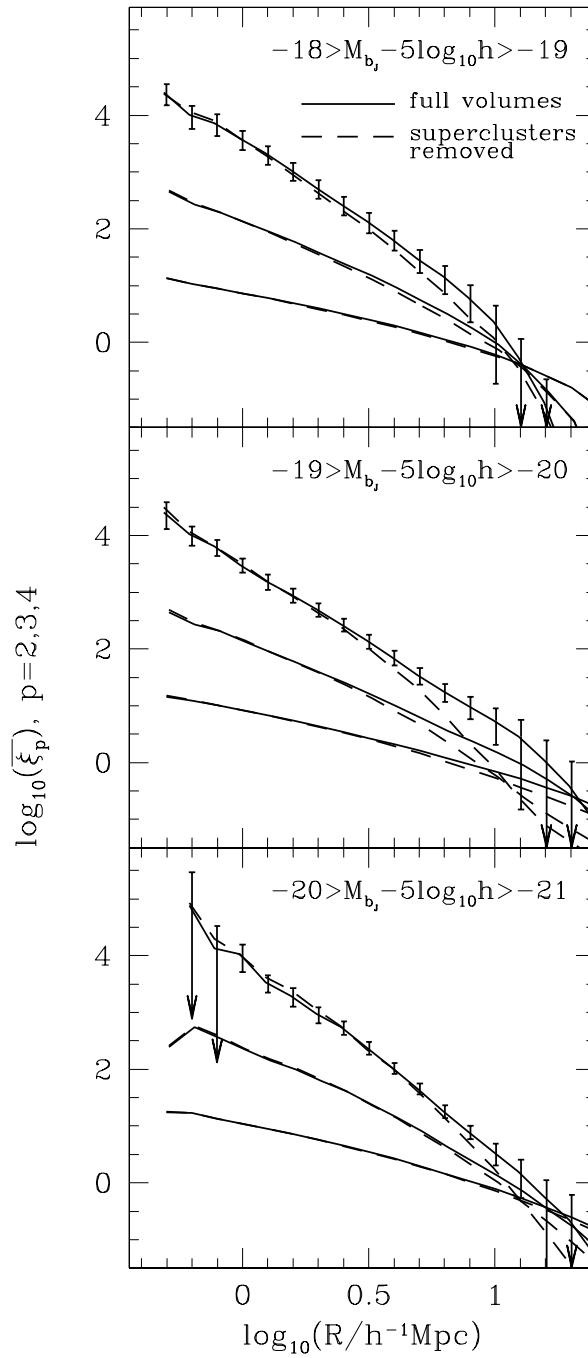
**Figure 3.8:** The volume averaged correlation functions for $p = 2$ to 4, with each panel showing the results from a different volume limited sample, as indicated by the legend. The solid lines show the estimates from the full volumes and the dashed lines show the results when the supercluster regions are omitted from the analysis. For clarity, errorbars are only plotted on the solid curves for order $p = 4$.
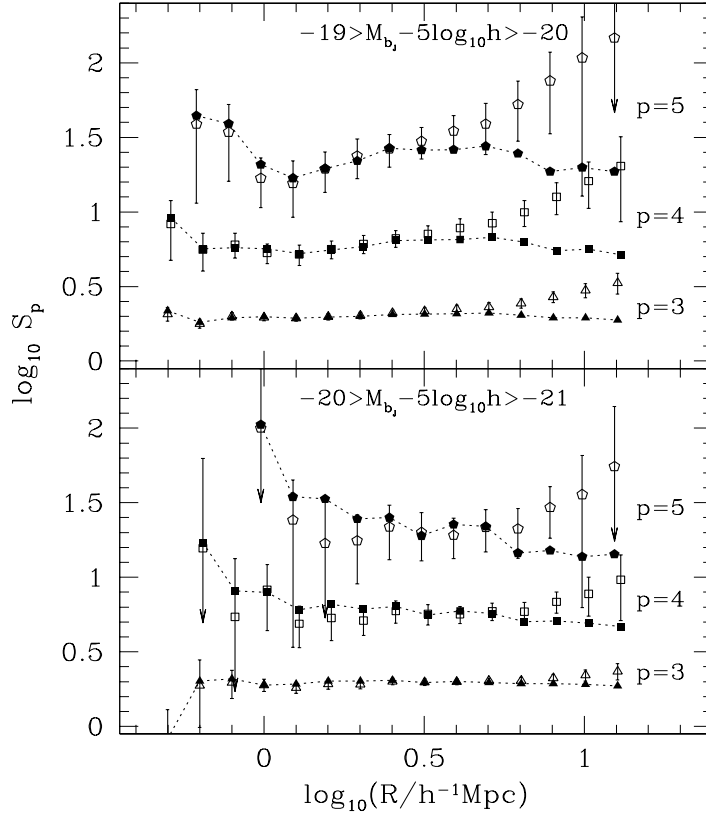
**Figure 3.9:** The hierarchical amplitudes, $S_3$ (triangles), $S_4$ (squares) and $S_5$ (pentagons). The top panel corresponds to galaxies with $-19 > M_{b_J} - 5\log_{10} h > -20$ and the bottom panel to $-20 > M_{b_J} - 5\log_{10} h > -21$. The open symbols with errorbars show the results obtained using the full volume limited catalogues. The fi lled symbols show how the results change when regions containing the two superclusters are omitted from the analysis.

## 3.5  Interpretation and the implications for galaxy bias

In this Section we quantify how the hierarchical amplitudes scale with galaxy luminosity and discuss the implications of our results for simple models of galaxy bias. We first test the hypothesis set out in Section 3.2.4 that the variation in clustering with luminosity apparent in Fig. 3.3 can be described by a single, relative bias factor, as defined by Eq. 3.14. The relative bias factors, $b_r$, computed from the variance and the deviation from the linear bias model, as quantified by $c_2'$ (Eq. 3.17), are listed in Table 3.2; here the mean value is given by the best $\chi^2$ fit over all cell radii. The change in the amplitude of the relative bias with sample luminosity, shown in Fig. 3.4, is in excellent agreement with the trend found by Norberg et al. (2001), who analysed the projected spatial clustering of 2dFGRS

galaxies. This agreement is remarkable given the different approaches used to measure the two-point correlations and the fact that the analysis in this paper is in redshift space, whereas the study carried out by Norberg et al. was unaffected by peculiar motions.

The coefficients $c_2'$ are different from zero at a $1$-$\sigma$ level. These findings are consistent with a small deviation from the linear biasing model (at a 2-sigma level for the brighter samples). This is in qualitative agreement with the estimation of $c_2$ using the the bispectrum (Scoccimarro 2000, Verde et al. 2002) or the 3-point function measured from the parent APM galaxy survey (Frieman & Gaztañaga 1999).

The variation of the hierarchical amplitudes with luminosity is plotted in Fig. 3.10. Each panel corresponds to a different order $p$. The filled points show the hierarchical amplitudes averaged over the different cell radii employed (these values and the associated errors are given in Table 3.2). The dotted line shows the hierarchical amplitudes predicted by the linear relative bias model (Eq. 3.15), using the best fit bias factors stated in Table 3.2. This model gives a rough approximation to the data. However, the observed variation of $S_p$ with luminosity is somewhat better described by a linear fit in the logarithm of luminosity, as shown by the solid lines. This implies that the dependence of the hierarchical amplitudes on luminosity is more complicated than expected in the simple relative bias model of Eq. 3.15 (as does the fact that we find some evidence for non-zero values for $c_2'$). The solid lines show the best linear fit to the hierarchical amplitudes as a function of the logarithm of the median luminosity of the samples:

$$S_p^G = A_p + B_p \log_{10}\left(\frac{L}{L_*}\right). \tag{3.18}$$

We find a greater than $2 - \sigma$ ($\Delta\chi^2 > 7.2$ for two parameters) detection of a non-zero value for $B_3$. However, for $p > 3$, the constraints on $B_p$ are much weaker and there is no clear evidence for a luminosity dependence in the $S_p$ values in these cases. For completeness, the best fit values for each order are: $(A_3, B_3) = (2.07, -0.40)$, $(A_4, B_4) = (6.15, -2.51)$, $(A_5, B_5) = (21.3, -13.5)$, $(A_6, B_6) = (58, -39)$.

## 3.6 Conclusions

In this paper we have measured the higher order correlation functions of galaxies in volume limited samples drawn from the 2dFGRS. The most recent comparable work is the analysis of the Stromlo-APM and UKST redshift surveys by Hoyle, Szapudi & Baugh (2000). These authors also considered volume limited subsamples drawn from the flux limited redshift survey. The largest UKST sample considered by Hoyle et al. contained 500 galaxies and covered a volume of $9 \times 10^5 h^{-3}\mathrm{Mpc}^3$; the reference sample used in our work contains 90 times this number of galaxies and covers ten times the volume. In our analysis, we can follow the variation of clustering over more than a decade in luminosity, whereas Hoyle et al. had to focus their attention around $L_*$.

The measurement of the higher order galaxy correlation functions is still challenging, however. In spite of the order of magnitude increase in size that the 2dFGRS represents
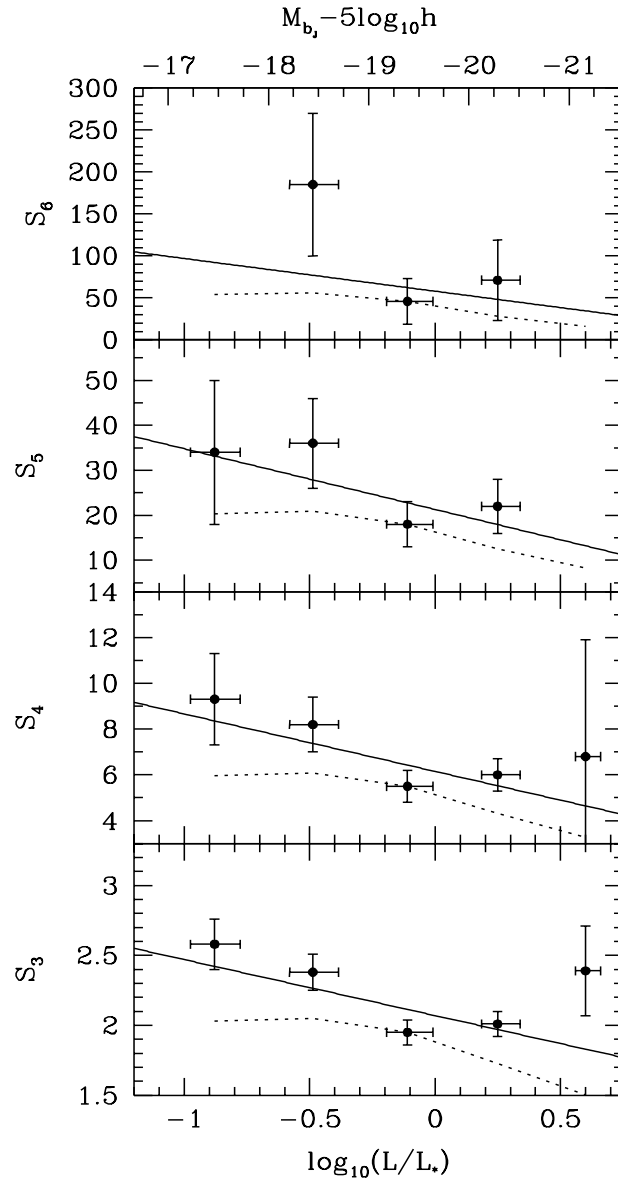
**Figure 3.10:** The variation of the hierarchical amplitudes, $S_p$, with absolute magnitude. The points are plotted at the median magnitude of each volume limited sample and the horizontal bars indicate the interval in which 25% to 75% of the galaxies fall, computed using the 2dFGRS luminosity function fit quoted by Norberg et al. (2002b). Each panel shows the results for a different order of clustering. The dotted line shows predictions of the linear relative bias model for the variation of the $S_p$ with luminosity (Eq. 3.15). The solid lines show linear fits in log luminosity to the observed trend in the value of $S_p$ with sample luminosity (see text of Section 3.5 for details).

over previously completed surveys, we have found that the higher order moments that we measure are somewhat sensitive to the presence of large structures. In particular, there are two superclusters that influence our measurements, one in the SGP region and the other in the NGP. These structures contain a sizeable fraction of the cluster mass groups in the 2dFGRS (Eke et al. 2004). The inclusion of these structures has an impact on our estimates of the three point and higher order volume averaged correlation functions on scales around $4 - 10h^{-1}$Mpc and above, depending on the order of the correlation function. For this reason, we have presented measurements of the higher order correlation functions both with and without these structures. We stress that the removal of these superclusters should not be considered a correction to the full catalogue results, but rather as an indication of the impact of rare structures on our results for the higher order moments. On the other hand, the up-turn that we find in the values of the hierarchical amplitudes on large scales is predicted by some structure formation models; for example models with non-Gaussian initial density fields predict a similar form for the $S_p$ as we measure from the full volume limited samples (Gaztañaga & Mähönen 1996; Gaztañaga & Fosalba 1998; Bernardeau et al. 2002).

The difficulties in estimating $S_p$ values on large, quasi-linear scales ($> 10h^{-1}$Mpc), prevent a direct comparison with perturbation theory (see Bernardeau et al. 2002). The current best estimates on these scales are still those measured from the angular APM Galaxy Survey (Gaztañaga 1994, Szapudi et al. 1995, Szapudi & Gaztañaga 1998). At the time of writing, the results from the SDSS Early Data Release are still limited to small scales (Gaztañaga 2002, Szapudi et al. 2002). Despite being unable to make a robust measurement of the higher order correlation functions on the very large scales for which weakly non-linear perturbation theory is applicable, we are still able to reach a number of interesting conclusions:

(i) We have demonstrated that the higher order galaxy correlation functions measured from the 2dFGRS follow a hierarchical scaling. Baugh et al. (2004) showed that $L_*$ galaxies display higher order correlation functions that scale in a hierarchical fashion; we have extended these authors' analysis to cover a wide range of galaxy luminosity. The higher order moments of the galaxy count distribution are proportional to the variance raised to a power that depends upon the order of the correlation function under consideration. This behaviour holds on physical scales ranging from those on which we expect the underlying density fluctuations to be strongly nonlinear all the way through to quasi-linear scales. This scaling has been tested up to the six point correlation function for the first time using a redshift survey. This confirms the conclusions of a complementary analysis carried out by Croton et al. (2004a), who found hierarchical scaling when measuring the reduced void probability function of the 2dFGRS.

(ii) We have estimated values of the hierarchical amplitudes, $S_p = \bar{\xi}_p / \bar{\xi}_2^{p-1}$, for cells of different radii. The hierarchical amplitudes are approximately constant on small to medium scales (depending on the order considered), while for the larger volumes, $S_p$

seem to increase with radius at large scales. Although this could in principle result from a boundary or mask effect (e.g. see Szapudi & Gaztañaga 1998; Bernardeau et al. 2002), we have shown with mock catalogues that this is not the case here (e.g. see Fig. 3.1). If the two most massive superclusters in the survey are removed from the analysis, the hierarchical amplitudes are remarkably independent over all scales. That the $S_p$ are roughly constant on small scales, with smaller amplitudes than in real space (e.g. Gaztañaga 1994), has been noted before for measurements in redshift space. It arises due to a cancellation of the enhanced signal on small scales in real space by a damping of clustering in redshift space due to peculiar motions (Lahav et al. 1993; Fry & Gaztañaga 1994; Hivon et al. 1995; Hoyle et al. 2000; Bernardeau et al. 2002).

(iii) We find that the amplitude of the higher order correlation functions scales with luminosity. The magnitude of the luminosity segregation increases with the order of the correlation (see Fig. 3.4). For the variance, $\bar{\xi}_2$, the strength of the trend is in very good agreement with that reported by Norberg et al. (2001), but note that these authors measured the luminosity segregation in real space, whereas our results are in redshift space. The strength of the luminosity segregation for higher orders can be mostly explained as the result of hierarchical scaling $\bar{\xi}_p \sim \bar{\xi}_2^{p-1}$, so that most of the effect can be attributed to luminosity segregation in the variance. This can be seen in Fig. 3.5 where data from different luminosities trace out the same hierarchical curve with little scatter.

(iv) We find some evidence for a residual dependence of $S_p$ on luminosity, although the effect is only significant within the errors for the skewness $p = 3$ (greater than $2\sigma$ level). It is not clear whether this is driven by a pure luminosity dependence of the higher order clustering or by a change in the galaxy mix with luminosity, with different galaxy types having different $S_p$ or by a combination of the two effects: see Norberg et al. (2002a) for an investigation of this point for the 2-point correlation function. A simple linear relative bias model (dotted line in Fig. 3.10) does not reproduce the dependence of the $S_p$ on luminosity.

We have interpreted our results in terms of a simple, local bias model, and we have quantified trends in clustering amplitude with luminosity by estimating relative bias factors. These measurements, summarised in Table 3.2, extend the constraints upon models of galaxy formation derived from the two-point correlation function, quantifying the shape of the tails of the count probability distribution as well as its width.

# 4 Voids and hierarchical scaling models[1]

## Abstract

We measure the redshift space reduced void probability function (VPF) for 2dFGRS volume limited galaxy samples covering the absolute magnitude range $M_{b_J} - 5\log_{10} h = -18$ to $-22$. Theoretically, the VPF connects the distribution of voids to the moments of galaxy clustering of all orders, and can be used to discriminate clustering models in the weakly non-linear regime. The reduced VPF measured from the 2dFGRS is in excellent agreement with the paradigm of hierarchical scaling of the galaxy clustering moments. The accuracy of our measurement is such that we can rule out, at a very high significance, popular models for galaxy clustering, including the lognormal distribution. We demonstrate that the negative binomial model gives a very good approximation to the 2dFGRS data over a wide range of scales, out to at least $20h^{-1}$Mpc. Conversely, the reduced VPF for dark matter in a $\Lambda$CDM universe does appear to be lognormal on small scales but deviates significantly beyond $\sim 4h^{-1}$Mpc. We find little dependence of the 2dFGRS reduced VPF on galaxy luminosity. Our results hold independently in both the north and south Galactic pole survey regions.

## 4.1 Introduction

The galaxy distribution on the largest scales display striking geometrical features, such as walls, filaments and voids. These features contain a wealth of information about both the linear and non-linear evolution of galaxy clustering. The nature of such clustering is dependent on many large and small scale effects, such as the cosmological parameters, galaxy and cluster environmental effects and history, the underlying dark matter distribution, and the way in which the dark and luminous components of the Universe couple and evolve. By probing the lower and higher orders of galaxy clustering, one thus hopes to shed light on those physical processes on which the clustering is dependent.

The traditional tool used to analyse such distributions has been the 2-point correlation function (Davis & Peebles 1983, Davis et al. 1988, Fisher et al. 1994, Loveday et al. 1995, Norberg et al. 2001, Zehavi et al. 2002), providing a description of clustering at the lowest orders. However despite its usefulness, the 2-point correlation function only provides a

---

[1] **D.J. Croton**, M. Colless, E. Gaztañaga, C.M. Baugh, P. Norberg, et al. (the 2dFGRS Team), MNRAS, 352, 828, 2004

full clustering description in the case of a Gaussian distribution. A more complete account of clustering must include correlation functions of higher orders, although these are often difficult to extract (see Croton et al. 2004b and Baugh et al. 2004 for an analysis of galaxy clustering in the 2dFGRS up to sixth order).

In light of this researchers have looked towards other clustering statistics to glean higher-order information from a galaxy distribution. Historically, many astronomers have favoured using void statistics (e.g. Fry 1986, Maurogordato & Lachieze-Rey 1987, Balian & Scha-effer 1989, Fry et al. 1989, Bouchet et al. 1993, Gaztañaga & Yokoyama 1993, Vogeley et al. 1994). This approach is useful in that results are easily obtainable and are well supported by a solid theoretical framework (White 1979, Fry 1986, Balian & Schaeffer 1989), which directly relates the void distribution to that of galaxy clustering of higher orders.

In this paper we employ the completed 2dFGRS dataset to undertake a detailed analysis of the void distribution using the reduced void probability function. We rely heavily on the well established theoretical framework which connects the void distribution with galaxy clustering of all orders (Eq. 4.1 below). The distribution of voids and the moments of galaxy clustering of all orders are known to be intimately linked, and the study of one can reveal information about the other which would otherwise be difficult to measure. Our goal is thus to use the reduced void probability function to investigate if galaxy clustering in the 2dFGRS obeys a hierarchy of scaling, and on what physical scales this scaling holds. We explore a number of phenomenological models of galaxy clustering which exhibit hierarchical scaling, and use these models to help clarify the way in which higher-order clustering is constructed[2].

This paper is organised as follows. In Section 4.2 we give a brief review of the theory behind the void statistics to be employed in our analysis. In Section 4.3 we present the 2dFGRS data set, and in Section 4.4 the counts-in-cells method we use to measure the void statistics is explained. Our results are presented in Section 4.5, and in Section 4.6 we provide a discussion and summary of our conclusions. Throughout, we adopt standard present day values of the cosmological parameters to compute comoving distance from redshift: a density parameter $\Omega_m = 0.3$ and a cosmological constant $\Omega_\Lambda = 0.7$.

## 4.2 Void statistics

### 4.2.1 The void probability function

For a given distribution of galaxies, the count probability distribution function (CPDF), $P_N(V)$, is defined as the probability of finding exactly $N$ galaxies in a cell of volume $V$ randomly placed within the sample. In the case where $N = 0$ we have the void probability function (VPF), $P_0(V)$. A choice of spherical cells with which to sample the distribution makes $P_0$ a function of sphere radius $R$ only. The VPF can be related to the hierarchy of

---

[2]Recently Hoyle et al. (2004) also measured the VPF of the 2dFGRS galaxy distribution, however their analysis focused more on the physical properties of voids in the 2dFGRS volume, rather than the hierarchical nature of galaxy clustering itself.

54

*p*-point correlation functions by (White 1979):

$$P_0(R) = \exp\left[ \sum_{p=1}^{\infty} \frac{(-\bar{N}(R))^p}{p!} \bar{\xi}_p(R) \right] . \tag{4.1}$$

Here $\bar{N}$ is the average number of objects in a cell of volume $V$, and $\bar{\xi}_p$ is the $p^{th}$ order correlation function averaged over $V$. A completely random (Poisson) distribution has $\xi_p \equiv 0$ for all $p > 1$, and thus $P_0$ reduces to a simple analytic expression:

$$P_{0_P}(R) = \exp[-\bar{N}(R)] . \tag{4.2}$$

Any departure from this relation is therefore a signature of the presence of clustering.

## 4.2.2 Hierarchical scaling

The idea that higher-order clustering arises in a *hierarchical* fashion from the 2-point correlation function appears naturally in perturbation theory and also in the highly non-linear regime of gravitational clustering (e.g. Peebles 1980), and is supported by much observational evidence (e.g. Maurogordato & Lachieze-Rey 1987, Fry et al. 1989, Gaztañaga 1992, Bouchet et al. 1993, Bonometto et al. 1995, Benoist et al. 1999, see Bernardeau et al. 2002 for a review). The concept can be generalised by assuming that each *p*-point correlation function depends only on the product of the 2-point correlation function and a dimensionless scaling coefficient, $S_p$:

$$\bar{\xi}_p(R) = S_p \bar{\xi}^{p-1}(R) , \tag{4.3}$$

where we have dropped the subscript 2 for the 2-point correlation function on the right-hand side for convenience (see Baugh et al. 2004 and Croton et al. 2004b for the measured values of $S_p$ up to $p = 6$ in redshift space for the 2dFGRS).

The hierarchical idea is directly applicable to the VPF, which is itself dependent on an infinite sum of *p*-point correlation functions. The hierarchical assumption allows us to remove the higher-order correlation functions from Eq. 4.1:

$$P_0(R) = \exp\left[ \sum_{p=1}^{\infty} \frac{(-\bar{N})^p}{p!} S_p \bar{\xi}^{p-1} \right] . \tag{4.4}$$

Furthermore, the above scaling relation allows us to express the VPF as a function of $\bar{N}\bar{\xi}$ only, where the scaling variable $\bar{N}\bar{\xi}$ approximately represents the average number of galaxies in a cell *in excess* of that expected given the mean density of the sample. We formalise this idea by firstly considering the analytic VPF expression for a purely random sample (Eq. 4.2). For the hierarchical situation, we can define a parameter $\chi$ with $P_0 = e^{-\bar{N}\chi}$, called the *reduced void probability function* (see Fry 1986):

$$\chi = -\ln(P_0) / \bar{N} . \tag{4.5}$$

We note here that, independent of the hierarchical assumption, $\chi$ normalises out the Poisson contribution to the distribution, and it is clear that the effects of clustering will appear as values of $\chi < 1$. Combining Eq. 4.4 and 4.5, the reduced VPF takes the form

$$\chi(\bar{N}\bar{\xi}) = \sum_{p=1}^{\infty} \frac{S_p}{p!}(-\bar{N}\bar{\xi})^{p-1} \ . \tag{4.6}$$

This exhibits the scaling advertised above, and the shape of $\chi(\bar{N}\bar{\xi})$ thus characterises the distribution of voids. If the scaling relation assumption holds, we expect different galaxy samples of different density and clustering strength to all collapse onto one universal curve, since all are a function of the same scaling variable. The curve will not be universal for different magnitude ranges if it turns out that the coefficients $S_p$ are a strong function of galaxy magnitude. The values of $S_p$ have recently been shown to depend at best only weakly on magnitude (see Croton et al. 2004b).

In the hierarchical picture, when $\bar{N}\bar{\xi} \ll 1$ one always recovers the Poisson VPF, $\chi(\bar{N}\bar{\xi}) = 1$, regardless of the actual clustering pattern or its strength. In the regime where $\bar{N}\bar{\xi} < 1$ we see from Eq. 4.6 that the reduced void probability function is dominated by the Gaussian contribution: $1 - \frac{1}{2}\bar{N}\bar{\xi}$. Thus the interesting observational window, where we can separate different clustering models, comes for values of $\bar{N}\bar{\xi}$ larger than unity. In practice, this only seems to happen at scales $R$ larger than a few $h^{-1}$Mpc, where $\bar{N} \sim R^3$ is large and dominates $\bar{\xi} \sim R^{-2}$. On smaller scales, where $\bar{\xi} > 1$, $\bar{N}\bar{\xi}$ will always be small, and galaxy samples will typically be too sparse to show measurable deviations from the Gaussian contribution. Thus, it should be stressed that the VPF is a good discriminant of weakly non-linear clustering only. In the highly non-linear regime voids do not provide us with much information.

Although the expansion given in Eq. 4.6 is technically only valid for small values of $\bar{N}\bar{\xi}$, the implications for clustering do extend beyond this. For large values of $\bar{N}\bar{\xi}$ models with different hierarchical amplitudes $S_p$ give different reduced void probabilities $\chi$: as $\bar{N}\bar{\xi}$ increases the value of $\chi$ gets smaller and the resulting VPF gets larger (with respect to the corresponding Poisson case). The Gaussian CPDF ($S_p = 0$) produces the smallest values of $\chi$ and therefore the largest deviations in the VPF. As we will illustrate with the models below, larger values of $S_p > 0$ will result in larger values of $\chi(\bar{N}\bar{\xi})$.

### 4.2.3 Phenomenological models

In presenting our reduced VPF results, we follow the lead of Fry (1986) and Fry et al. (1989) and compare with a number of model scaling relations that differ in the way they fix the scaling coefficients $S_p$. We give a brief description of these models here, and refer the reader to the cited papers and references therein for further details. In Fig. 4.1 we summarise the behaviour of each.
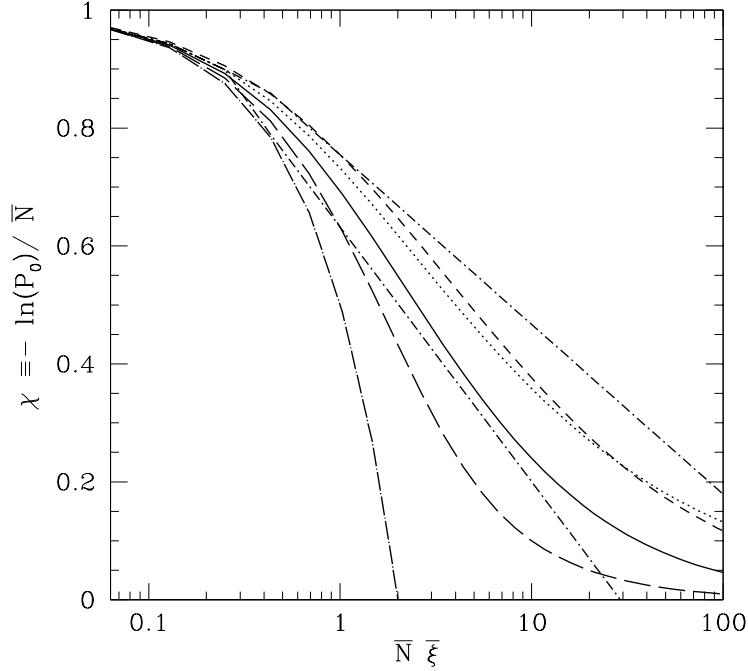
**Figure 4.1:** Reduced void probability $\chi$ for different models (left to right at $\chi \sim 0.4$): Gaussian (long-dashed-dotted, Eq. 4.12), minimal (long-dashed, Eq. 4.7), BBGKY (short-dashed-dotted, Eq. 4.10 with $Q = 2/3$), negative binomial (continuous, Eq. 4.8), thermodynamic (dotted, Eq. 4.9), lognormal (short-dashed) and BBGKY (short-dashed-dotted, Eq. 4.10 with $Q = 1$).

## Minimal model

The first model is the so-called *minimal cluster model*, the motivation of which is to consider a clumpy galaxy distribution of clusters, the cluster distribution in space itself being Poisson with a Poisson galaxy occupancy. This is reminiscent of the halo model (e.g. Cooray & Sheth 2002) but with a Poisson halo/cluster profile. Evaluating the set of $S_p$'s from the distribution function generated by this model leads to a functional form for $\chi$ of

$$\chi = (1 - e^{-\bar{N}\bar{\xi}})/\bar{N}\bar{\xi} \quad \text{(minimal)}, \tag{4.7}$$
$$S_p = 1 \quad (\text{Skewness} : S_3 = 1) .$$

Fry (1986) speculated that this model represents a lower bound on the allowable functions $\chi(\bar{N}\bar{\xi})$ in any consistent hierarchical model.

## Negative binomial model

The second model, commonly called the *negative binomial model*, has been used in a number of fields with different physical motivations (Klauder & Sudarshan 1968, Carruthers &

Shin 1983, Carruthers & Minh 1983, Fry 1986, Elizalde & Gaztañaga 1992, Gaztañaga & Yokoyama 1993). After a set of $T$ independent trials with probability $q$ for "success" and $p = 1 - q$ for "failure", the probability of having $S$ number of successes *and $F = T - S$* number of failures is given by the binomial distribution: $P(S) = (F + S)!/S!/F!(1 - q)^F q^S$. The negative binomial distribution describes the probability for having $S$ number of successes *after* a fixed number $F$ of failures: $P(S) = (F + S - 1)!/S!/(F - 1)!(1 - q)^F q^S$. Note that in the binomial case what is fixed is the total number of trials.

We can identify a "success" as finding a galaxy in a cell, so that $P_N = P(N = S)$ is the CPDF. The fixed number of failures, $F$, is assumed to be inversely proportional to $\bar{\xi}$ (the larger the $\bar{\xi}$, the smaller the number of failures to count a galaxy in a cell). The probability for a failure $p$ is assumed to be proportional to the product $\bar{N}\bar{\xi}$ (because of clustering there is an $\bar{N}\bar{\xi}$ rms excess of galaxies within a cell with $\bar{N}$ density: the larger this clumpiness the larger the probability to miss galaxies in a random cell). After fixing the proportionality constants, this leads to $F = 1/\bar{\xi}$ and $p = \bar{N}\bar{\xi}/(1 + \bar{N}\bar{\xi})$ (for a different derivation see Gaztañaga & Yokoyama 1993). This model is a discrete version of the gamma probability distribution (see Gaztañaga, Fosalba & Elizalde 2000). The reduced VPF and cumulants in this case are:

$$\chi = \ln(1 + \bar{N}\bar{\xi})/\bar{N}\bar{\xi} \quad \text{(negative binomial)}, \tag{4.8}$$
$$S_p = (p - 1)! \quad \text{(Skewness}: S_3 = 2) .$$

**Thermodynamic model**

The third model was first suggested by Saslaw and Hamilton (1984) and arose from a thermodynamic theory of the properties of gravitational clustering. The original model had a fixed degree of virialization (temperature or density variance) for all cell sizes, but such behaviour is inconsistent with observations. The model was later extended (see e.g. Fry 1986) to include a different level of virialization at each scale, to be identified with the variance $\bar{\xi}$ as a function of scale. The results is:

$$\chi = [(1 + 2\bar{N}\bar{\xi})^{1/2} - 1]/\bar{N}\bar{\xi} \quad \text{(thermodynamic)}, \tag{4.9}$$
$$S_p = (2p - 3)!! \quad \text{(Skewness}: S_3 = 3) ,$$

where $(2p - 3)!! = (2p - 3).(2p - 5).(2p - 7)...$ and truncates at zero.

**Lognormal distribution**

The *lognormal* distribution (e.g. Coles & Jones 1991, Weinberg & Cole 1993), is often used as a phenomenological model for galaxy and dark matter clustering. Although no analytic expression exists for the reduced void probability, it can be estimated numerically (see above references) and is found to behave similarly to the thermodynamic model, as shown in Fig. 4.1 (note how the dotted and the short-dashed lines overlap). As in the thermodynamic model, the lognormal distribution also has a large skewness: $S_3 = 3 + \bar{\xi}$ (which exactly tends to the thermodynamical value $S_3 \rightarrow 3$ on large scales where $\bar{\xi} \rightarrow 0$).

In fact, it should be noted that the lognormal model is not truly hierarchical, as it does not have constant moments $S_p$, but in practice the variations have little effect on the reduced void distribution.

**BBGKY model**

The BBGKY model of Fry (1984) provides a prescription for $\chi$ and $S_p$ as an asymptotic solution to the BBGKY kinetic equations:

$$
\begin{aligned}
\chi &= 1 - (\gamma + \ln 4Q\bar{N}\bar{\xi})/8Q \quad \text{(BBGKY)}, &\text{(4.10)} \\
S_p &= (4Q)^{p-2}\frac{p}{2(p-1)} ,
\end{aligned}
$$

where $\gamma = 0.57721...$ is Euler's constant. This asymptotic solution is only a good approximation for large values of $\bar{N}\bar{\xi}$. When $\bar{N}\bar{\xi}$ becomes small, for completeness we simply match it to the nearest model.

The skewness in the BBGKY model contains a free parameter, $S_3 = 3Q$, with the restriction that $Q > 1/3$. Fry (1984) used $Q \simeq 1$, which was close to the then observed $S_3 \simeq 3$ value measured from the 3-point function in real space (inferred from projected maps). Croton et al. (2004b) and Baugh et al. (2004) have since shown that $S_3$ is in fact closer to $S_3 = 2$ in the 2dFGRS, corresponding to the case where $Q = 2/3$. Both possibilities are shown as short-dashed-dotted lines in Fig. 4.1, with the upper curve for $Q = 1$ and the lower curve for $Q = 2/3$. Since we later show that neither of these $Q$ values with the BBGKY model are able to match the data very well, for the sake of clarity we omit the lower $Q = 2/3$ curve in subsequent figures. The upper curve is retained in order to demonstrate the range of possible $\chi$ values that a hierarchical model may have.

**Poisson and Gaussian distributions**

In addition to the above models we also use the analytic expressions of the reduced VPF for purely Poisson and Gaussian distributions. Trivially, from Eq. 4.6 we see that

$$
\chi = 1 \quad \text{(Poisson)}, \tag{4.11}
$$

and

$$
\begin{aligned}
\chi &= 1 - \frac{1}{2}\bar{N}\bar{\xi} \quad \text{(Gaussian)}, &\text{(4.12)} \\
S_p &= 0 \quad \text{(Skewness}: S_3 = 0) .
\end{aligned}
$$

The later only makes sense for small values of $\bar{N}\bar{\xi}$, but note that even when the underlying distribution is not Gaussian, the above expression always gives a good approximation to the void probability in the limit of small $\bar{N}\bar{\xi}$.

## 4.3 The data sets

### 4.3.1 The 2dFGRS data set

In our analysis we use the completed 2dFGRS (Colless et al. 2003). The catalogue is sourced from a revised and extended version of the APM galaxy catalogue (Maddox et al. 1990), and the targets are galaxies with extinction-corrected magnitudes brighter than $b_J$=19.45. Our galaxy sample contains a total of 221,414 high quality redshifts. The median depth of the full survey, to a nominal magnitude limit of $b_J \approx 19.45$, is $z \approx 0.11$. We consider the two large contiguous survey regions, one in the south Galactic pole (SGP) and one towards the north Galactic pole (NGP), and restrict our attention to the parts of the survey with high redshift completeness ($> 70\%$). Full details of the 2dFGRS and the construction and use of the mask quantifying the completeness of the survey can be found in Colless et al. (2001, 2003).

A model accounting for the change in galaxy magnitude due to redshifting of the $b_J$-filter bandpass (k-correction) and galaxy evolution (e-correction) was adopted following Norberg et al. (2002b):

$$k(z) + e(z) = \frac{z + 6z^2}{1 + 20z^3} \; .$$

(4.13)

This model gives the mean k+e-correction over the mix of different spectral types observed in the 2dFGRS sample, and was shown by Norberg et al. to accurately account for such observational effects when estimating 2dFGRS galaxy absolute magnitudes.

### 4.3.2 Volume limited catalogues

The 2dFGRS galaxy catalogue is *magnitude-limited*, meaning the survey is constructed by observing galaxies brighter than the fixed apparent magnitude limit of $b_J$=19.45. A magnitude-limited galaxy catalogue is not uniform in space, since intrinsically fainter objects may be missed even if they are relatively nearby, while the most luminous galaxies will be seen out to large distances. This non-uniformity of the magnitude-limited catalogue must be dealt with for a correct statistical analysis, and the simplest way to do this with a catalogue the size of the 2dFGRS is by constructing a volume limited catalogue (VLC) from the magnitude-limited sample.

Volume limited catalogues are defined by choosing minimum and maximum *absolute* magnitude limits. These limits, along with the intrinsic apparent magnitude limits of the survey, define minimum and maximum redshift boundaries via standard luminosity–distance relations (Peebles 1980). The VLC is built by selecting galaxies whose redshift lies within the minimum and maximum boundaries just determined, and whose absolute magnitude lies within the specified absolute magnitude limits. Such galaxies can be displaced to any redshift within the VLC volume and still remain within the bright and faint apparent magnitude limits of the magnitude limited survey. Table 4.1 presents the properties of the combined NGP and SGP volume limited catalogues used in this paper.

| Mag. range | | Median mag. | $N_G$ | $\rho_{ave}$ | $d_{mean}$ | $z_{min}$ | $z_{max}$ | $D_{min}$ | $D_{max}$ | Volume |
|---|---|---|---|---|---|---|---|---|---|---|
| $M_{b_J} - 5\log_{10}h$ | | $M_{b_J} - 5\log_{10}h$ | | $10^{-3}/h^{-3}\mathrm{Mpc}^3$ | $h^{-1}\mathrm{Mpc}$ | | | $h^{-1}\mathrm{Mpc}$ | $h^{-1}\mathrm{Mpc}$ | $10^6 h^{-3}\mathrm{Mpc}^3$ |
| $-18.0$ | $-19.0$ | $-18.44$ | 23290 | 9.26 | 4.76 | 0.014 | 0.088 | 39.0 | 255.6 | 2.52 |
| $-19.0$ | $-20.0$ | $-19.39$ | 44931 | 5.64 | 5.62 | 0.021 | 0.130 | 61.1 | 375.6 | 7.97 |
| $-20.0$ | $-21.0$ | $-20.28$ | 33997 | 1.46 | 8.82 | 0.033 | 0.188 | 95.1 | 537.2 | 23.3 |
| $-21.0$ | $-22.0$ | $-21.16$ | 6895 | 0.110 | 20.9 | 0.050 | 0.266 | 146.4 | 747.9 | 62.8 |

**Table 4.1:** Properties of the combined 2dFGRS SGP and NGP volume limited catalogues (VLCs). Columns 1 and 2 give the faint and bright absolute magnitude limits that define the sample. Column 3 gives the median magnitude of the sample, computed using the Schechter function parameters quoted by Norberg et al. (2002b). Columns 4, 5 and 6 give the number of galaxies, the mean number density and the mean inter-galaxy separation for each VLC, respectively. Columns 7 and 8 state the redshift boundaries of each sample for the nominal apparent magnitude limits of the survey; columns 9 and 10 give the corresponding comoving distances. Finally, column 11 gives the combined SGP and NGP volume. All distances are comoving and are calculated assuming standard cosmological parameters ($\Omega_m = 0.3$ and $\Omega_\Lambda = 0.7$).

## 4.4 Measuring the galaxy distribution

To measure the void probability function we use the method of counts-in-cells. The survey volume is uniformly sampled with a large number ($2.5 \times 10^7$) of randomly placed spheres of fixed radius $R$, and we record the number of times a sphere contains exactly $N$ galaxies. Our choice of massive oversampling ensures a high level of statistical accuracy in the calculation (Szapudi 1998). The CPDF can then be found as the probability of finding exactly $N$ galaxies in a randomly placed sphere:

$$P_N(R) = \frac{N_N}{N_T} \,, \qquad (4.14)$$

where $N_N$ is the number of spheres that contain exactly $N$ galaxies out of the total number of spheres thrown down, $N_T$. By definition, the void probability function is the probability of finding an empty sphere:

$$P_0(R) = \frac{N_0}{N_T} \,. \qquad (4.15)$$

The mean number of galaxies expected inside a sphere of radius $R$ is readily calculated from

$$\bar{N}(R) = \sum N P_N(R) \,, \qquad (4.16)$$

and this estimation of $\bar{N}$ for each individual VLC is found to be independent of scale and indistinguishable from that determined from the known mean galaxy density. The volume averaged 2-point correlation function, $\bar{\xi}_2$, is found directly from the second moment of the CPDF:

$$\bar{\xi}_2(R) = \frac{\langle (N - \bar{N})^2 \rangle - \bar{N}(R)}{\bar{N}(R)^2} \,. \qquad (4.17)$$

We have also carried out an independent counts-in-cells analysis by placing the spheres at the positions of a regular spatial lattice that homogeneously oversamples the survey area. The results are insensitive to these details.

   The 2dFGRS has an inherent spectroscopic galaxy incompleteness which will change the results of any void analysis (Colless et al. 2001). In addition, due to the irregular geometry of the survey boundaries it is difficult to guarantee that every sphere will be completely contained within the regions we wish to measure. Since the CPDF is sensitive to such effects we adopt a technique which accurately accounts for such deficiencies. This method is explained and tested in Appendix 4A (see also Croton et al. 2004b).

### 4.4.1 Error estimation

We estimate the error on our void statistics using the set of 22 mock 2dFGRS surveys described by Norberg et al. (2002b; see also Cole et al. 1998). These mock catalogues have the same radial and angular selection function as the 2dFGRS and have been convolved with the completeness mask of the survey. The mock catalogues are drawn from the Virgo Consortium's $\Lambda$CDM Hubble Volume simulation and thus include sample variance due

to large scale structure (see Evrard et al. 2002 for a description of the Hubble Volume simulation). The $1\sigma$ errors we quote correspond to the *rms* scatter over the ensemble of mocks (see Norberg et al. 2001). We have compared this estimate with an internal estimate using a jack knife technique (Zehavi et al. 2002). In the jack knife approach, the survey is split into subsamples. The error is then the scatter between the measurements when each subsample is omitted in turn from the analysis. The jack knife gives comparable errors to the mock ensemble for the VPF measurement.

## 4.5 Results

We begin with Fig. 4.2, where we plot the reduced void probability function, $\chi$, individually as a function of both the mean galaxy number, $\bar{N}$, and the variance, $\bar{\xi}$, in the top and bottom panels respectively. The physical scale given on each top axis corresponds to values for the $-20 > M_{b_{\mathrm{J}}} - 5\log_{10} > -21$ VLC only, and is included for reference (for VLCs of different mean density the scale at which a given $\bar{N}$ or $\bar{\xi}$ will occur will be different). Note that for VLCs fainter than our reference this scale shifts to the right in the top panel and to the left in the bottom panel. The converse is true when considering brighter galaxies than the reference.

The main feature of this figure is that neither $\bar{N}$ nor $\bar{\xi}$ individually show hierarchical scaling when plotted against $\chi$. Note that smaller values of $\chi$ correspond to larger deviations from a Poisson distribution. Brighter galaxy samples show behaviour which is closer to that of the Poisson distribution for any given value of $\bar{N}$ or $\bar{\xi}$, however this merely reflects the fact that the brightest VLCs are also the sparsest (Table 4.1).

We now test for hierarchical scaling in the 2dFGRS, as outlined in Section 4.2.2. In Fig. 4.3 we plot the reduced void probability function, $\chi$, as a function of the scaling variable $\bar{N}\bar{\xi}$. In this way we eliminate the dependence of the void probability on the variance and mean density. This figure shows VLCs ranging in absolute magnitude from $-18$ to $-22$. If a scaling between correlation functions of different orders exits we expect to see all points for each catalogue fall onto the same line. Again we provide a reference scale on the top axis, given for the $-20 > M_{b_{\mathrm{J}}} - 5\log_{10} > -21$ VLC, and note that for fainter galaxy samples this scale shifts to the right and conversely for brighter samples. Over-plotted are the scaling models previously discussed in Section 4.2.3: (bottom to top) the Gaussian (Eq. 4.12), minimal (Eq. 4.7), negative binomial (Eq. 4.8), thermodynamic (Eq. 4.9), lognormal, and BBGKY (Eq. 4.10, $Q = 1$) models respectively.

Fig. 4.3 demonstrates the clear signature of hierarchical scaling in the clustering moments of the 2dFGRS. All points are seen to follow a tight path (within the error bars) out to values of $\bar{N}\bar{\xi} \sim 30$, and sit close to the negative binomial model prediction along this entire range. Such values encompass galaxy clustering from the deeply non-linear to the linear regime, revealing hierarchical scaling out to scales of $\sim 20h^{-1}$Mpc or more.

For comparison, in Fig. 4.3 we also present the dark matter reduced VPF measured from the $\Lambda$CDM Hubble volume simulation (particle mass $2.3 \times 10^{12} h^{-1} M_{\odot}$) (Evrard et al. 2002). We independently analyse 100 randomly placed cubes of side length $200h^{-1}$Mpc
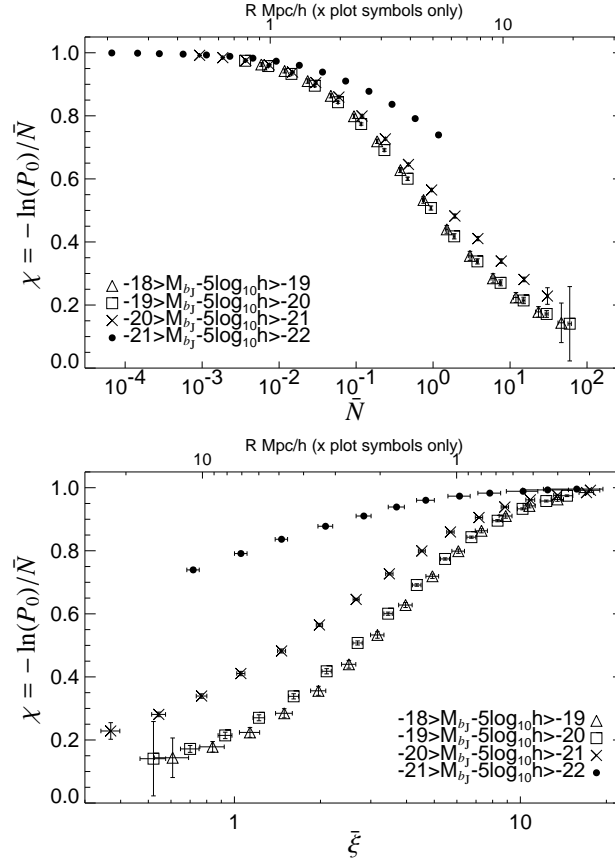
**Figure 4.2:** The 2dFGRS reduced VPF, $\chi = -\ln P_0/\bar{N}$, as a function of (top) the mean galaxy number, $\bar{N}$, and (bottom) the variance of the distribution, $\bar{\xi}$, as measured for volume limited catalogues in varying luminosity bins (Table 4.1). Smaller values of $\chi$ imply larger deviations from a Poisson distribution. The reference scale given on the top axis is for the $-20 > M_{b_J} - 5\log_{10} > -21$ VLC only (each $\bar{N}$ and $\bar{\xi}$ value individually correspond to different scales for each VLC). Notice that neither variable displays hierarchical scaling when plotted individually against $\chi$.

(approximately equal in volume to our $M^*$ galaxy volume limited sample), from which the rms is then plotted. In contrast to the 2dFGRS galaxies, the dark matter follows a lognormal distribution out to values of $\bar{N}\bar{\xi} \sim 6$ (a scale of approximately $R \sim 4h^{-1}$Mpc in the simulation), but then deviates strongly on larger scales (the last point plotted corresponds to $R = 10h^{-1}$Mpc in the simulation).

To highlight the differences between the 2dFGRS galaxy reduced VPF and the negative binomial prediction, in Fig. 4.4 we show the fractional difference between the two. Also included are the "bounding" models closest to the negative binomial: the minimal
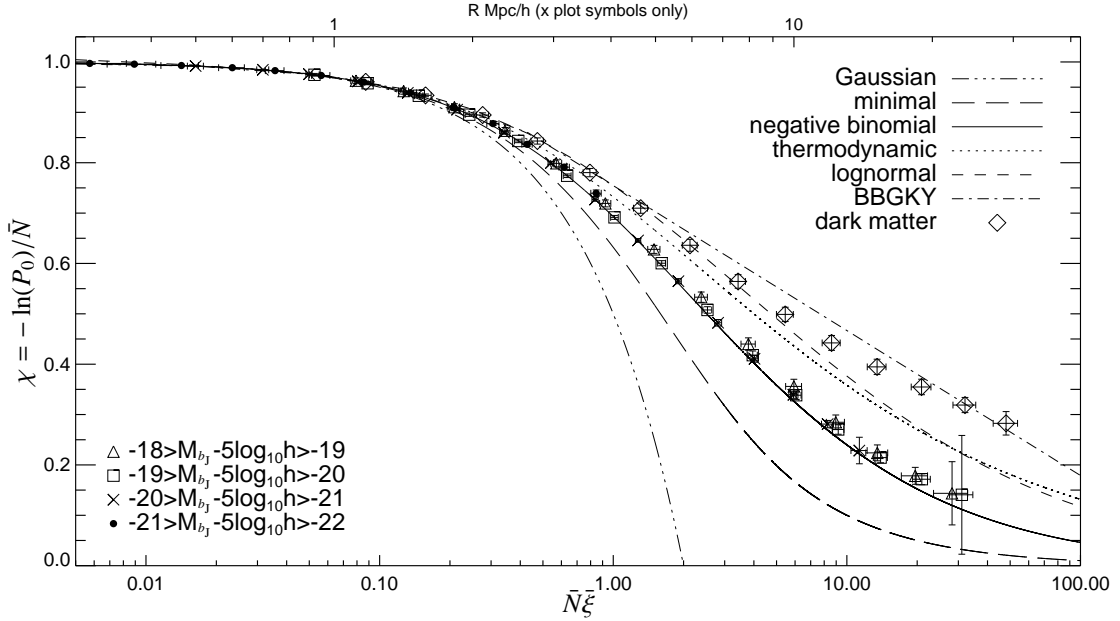
**Figure 4.3:** The reduced VPF, $\chi = -\ln P_0/\bar{N}$, as a function of the scaling variable $\bar{N}\bar{\xi}$ for the four 2dFGRS galaxy VLCs from Table 4.1. The dark matter reduced VPF, as measured from the $\Lambda$CDM Hubble Volume simulation, is shown as large diamonds. In all cases, smaller values of $\chi$ imply larger deviations from a Poisson distribution. The reference scale given on the top axis is for the $-20 > M_{b_J} - 5\log_{10} > -21$ VLC only (each $\bar{N}\bar{\xi}$ value corresponds to a different scale for each VLC). If hierarchical scaling is present in the galaxy distribution all points should collapse onto a single line, which is clearly seen. The six curves represent the hierarchical models discussed in Section 4.2.3 (Eq. 4.7 to 4.12).

and thermodynamic models. All 2dFGRS points plotted are consistent with the negative binomial model at the $2\sigma$ level. At larger values of $\bar{N}\bar{\xi}$ we find some small departures from the negative binomial model, and it is interesting to note that these deviations appear the greatest for the faintest VLC. This could be explained by the weak dependence of $S_p$ on galaxy luminosity found by Croton et al. (2004b), where fainter samples typically had larger $S_p$ values than brighter samples (albeit with large error bars). The effect of such an increase in the hierarchical picture would result in a value of $\chi$ closer to unity (Eq. 4.6).

An important feature of Fig. 4.3 is the inconsistency of the reduced void probability function with a Gaussian distribution across all scales considered (up to approximately $30h^{-1}$Mpc). On large scales where the galaxy correlation functions become too small to measure independently, the value of $\bar{N}$ is found to increase faster than $\bar{\xi}$ decreases, and thus $\chi$ is still affected strongly by higher-order correlations. It is clear that even in the quasi-linear regime, where one would expect galaxy clustering to be very simple, higher-order
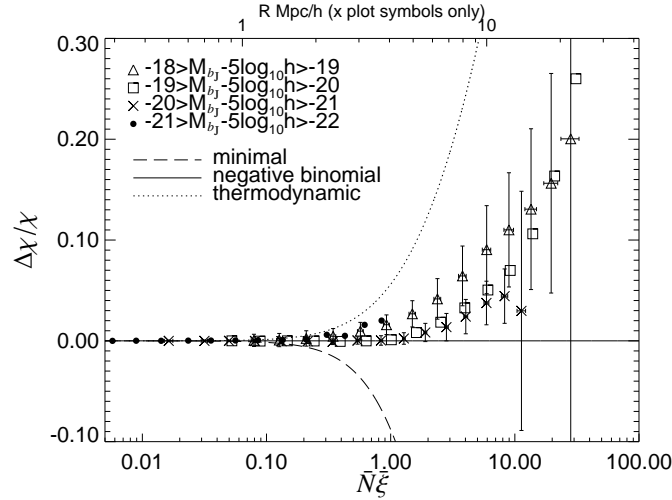
**Figure 4.4:** The fractional difference between the negative binomial model and the 2dF-GRS, thermodynamic, and minimal reduced VPFs. The reference scale given on the top axis is for the $-20 > M_{b_J} - 5\log_{10} > -21$ VLC only (each $\bar{N}\bar{\xi}$ value corresponds to a different scale for each VLC). Some error bars have been omitted for clarity. All 2dFGRS results are consistent with the negative binomial model at the $2\sigma$ level.

correlations still play a significant role in the make-up of the large scale distribution.

To evaluate the robustness of the results seen in Fig. 4.3 we apply two tests to illustrate the degree of confidence we should have in believing the existence of hierarchical scaling in the 2dFGRS. Firstly, one of the most valuable features of the 2dFGRS is that we have available data from two totally independent regions on the sky, the SGP and NGP. So far we have been calculating our void statistics from the combined volume of the two, but it is useful to check that the scaling properties still exist in the two regions independently. This we do in the top panel of Fig. 4.5, where the large symbols represent the SGP and small symbols the NGP. It is immediately clear that galaxies from both the SGP and NPG regions independently obey hierarchical scaling and reproduce the negative binomial results discussed previously to good accuracy.

Secondly, we test the scaling properties seen in Fig. 4.3 by calculating the reduced VPF for randomly diluted samples of galaxies. Such dilutions leave the 2-point correlation function unchanged, and within the hierarchical paradigm the scaling exhibited in Fig. 4.3 should also remain unchanged. This test is shown in the bottom panel of Fig. 4.5, where we have diluted each of the VLCs used in Fig. 4.3 by factors of 0.5 (large symbols) and 0.25 (small symbols). We again see that the trend for hierarchical scaling exists and follows the negative binomial model, consistent with our previous conclusions.
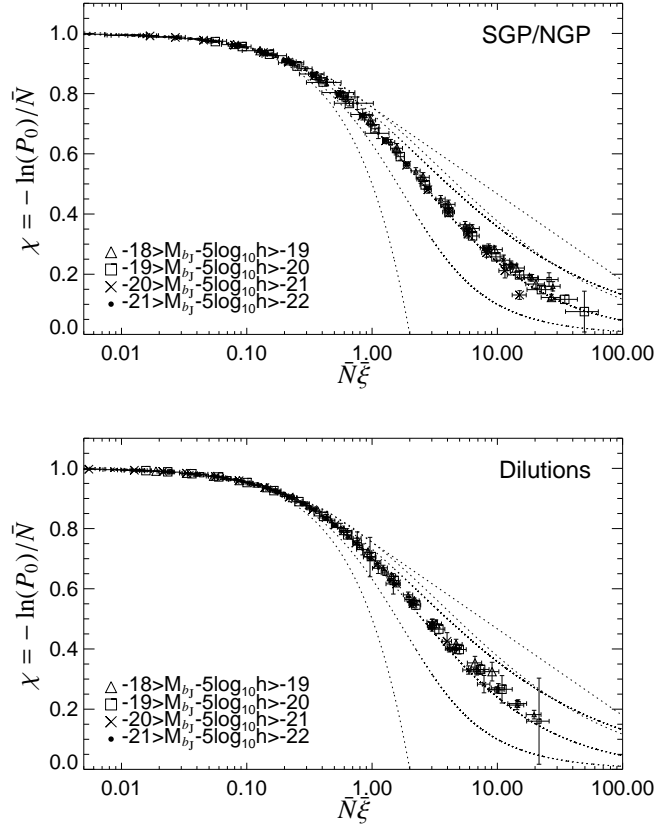
**Figure 4.5:** Two tests of the scaling properties seen in Fig. 4.3 using the reduced VPF, $\chi = -\ln P_0/\bar{N}$, as a function of the scaling variable $\bar{N}\bar{\xi}$. (top) Independent SGP and NGP VLCs show identical scaling to that seen in Fig. 4.3. Here the large symbols represent the SGP result, and the small represent the NGP result. (bottom) The same combined VLCs as in Fig. 4.3, but now diluted by factors of 0.5 (large symbols) and 0.25 (small symbols). If hierarchical scaling exists in the galaxy distribution, dilution should make little difference to the results found in Fig. 4.3. For both panels, the dotted curves represent the same six models plotted in Fig. 4.3 and discussed in Section 4.2.3. Some error bars have been omitted for clarity.

## 4.6 Discussion

The 2dFGRS represents an enormous improvement in volume and number of galaxies over previous surveys, such as the CfA or the SSRS samples. Here we measure the galaxy distribution over both a wider range in variance ($\bar{\xi} \sim 0.3 - 20$) and mean galaxy number ($\bar{N} \sim 10^{-4} - 10^2$). The impact on the VPF can be seem by comparing Fig. 4.3 above to Fig. 7 in Gaztañaga & Yokoyama (1993), where the CfA and SSRS data can not discrim-

inate between the negative binomial and the thermodynamical models. As shown here in Fig. 4.3 and 4.4, although the agreement is not always perfect, the negative binomial does much better, by far, than any of the other models considered in the literature. This includes the lognormal distribution, which is close to the thermodynamical model (Fig. 4.1) and is widely used as a phenomenological clustering model. These results are valid independently in the NGP and SGP regions of the survey, and do not change when we randomly dilute the galaxy samples (Fig. 4.5). The lognormal distribution does, however, appear to be a good representation for the distribution of dark matter on smaller scales (less than $\sim 4h^{-1}$Mpc), although not at larger scales. The differences between the galaxy and dark matter reduced VPFs can be understood by noting the differences between their higher-order volume-averaged correlation functions, as shown by Baugh et al. (2004).

The 2dFGRS reduced void probability function appears to behave differently from the one presented by Vogeley et al. (1994) for the CfA-1 and CfA-2 samples, which show more scatter with magnitude and values well above the negative binomial model (compare their Fig. 4 to our Fig. 4.3). Here we do not observe any significant departure from the scaling models on scales larger than $R \sim 8.5h^{-1}$Mpc as they had previously found. In contrast, our results indicate hierarchical scaling exists in the galaxy distribution out to scales of at least $R \sim 20h^{-1}$Mpc.

Although some heuristic derivations exist for the negative binomial distribution (see Section 4.2.3), we have not found a satisfactory physical explanation for the very good performance of this model. The value of the skewness for the negative binomial model, $S_3 = 2$, is quite close to the direct measurement in the 2dFGRS: $S_3 = 1.86 - 2.03$ (Baugh et al. 2004). Other phenomenological models, such as the thermodynamical or the lognormal distribution, have larger values for the skewness ($S_3 \simeq 3$). A similar trend was found by Baugh et al. for the higher order coefficients $S_4$, $S_5$, and $S_6$. In this respect it is not totally surprising that the negative binomial does better. The one freedom the reduced VPF has is in the value of the scaling coefficients which appear in the sum in Eq. 4.6. If these coefficients are found to match that predicted by a particular hierarchical scaling model, then one would expect their reduced VPFs to look similar.

Perturbation theory with Gaussian initial conditions predict values for the $S_p$'s that are universal and only depend on the local spectral index. They are therefore a known function of scale. Such scale dependence, however, breaks the hierarchy in Eq. 4.3, and therefore the universality of the scaling in Eq. 4.6. On the other hand, redshift space distortions and biasing tend to wash away this scale dependence (see e.g. Fig. 49 in Bernardeau et al. 2002), an argument which has been used to explain the good performance of the scaling hierarchy. But, as shown by Baugh et al. (2004) and Croton et al. (2004b), the measured values of the $S_p$'s do not seem to match the expectations in either dark matter models or mock galaxy surveys (both in redshift space). The reasons for this, and a more physically motivated interpretation of the negative binomial model, will provide important constraints to be matched by models of galaxy formation.

# Appendix 4A: Correcting for incompleteness in the 2dFGRS

The 2dFGRS is spectroscopically incomplete to a small degree resulting in missed galaxies (see Colless et al. 2001), and some spheres used in our counts-in-cells analysis may straddle the survey boundaries or holes resulting in missed volume. Such influences will induce an artifical "voidness" that will be picked up by our VPF measurements, and any analysis that neglects these effects will tend to over predict the VPF. Thus it is desirable to devise a method with which one can confidently correct for such incompleteness. This is not a trivial exercise, since weighting schemes that work with other statistics (e.g. Efstathiou et al. 1990) cannot necessarily be applied here, as the VPF will remain uncorrected (how does one weight no galaxies?). Such techniques will lead to an under-estimation of the mean density of galaxies and an over-estimation of the influence of the voids. Ideally, we need to ensure that any correction faithfully reproduces the full CPDF of the complete distribution for all orders of galaxy clustering.

To resolve these problems we have adopted the following method. When a satisfactory sphere location is found in the 2dFGRS wedge we project the sphere onto the sky and estimate, using the survey masks (Colless et al. 2001), the average completeness $f$ within the sphere. Due to the incompleteness effects described above we typically will have $f < 1$. Instead of viewing this incompleteness as missed galaxies, we instead consider it as *missed volume*, and to compensate we scale the radius of the sphere according to $R' = R/f^{\frac{1}{3}}$. This new radius gives an effective sphere volume *with incompleteness* equal to that of a 100% complete sphere with the original radius. Galaxies are counted within the new radius $R'$, but contribute their counts to the scale $R$. Each sphere we place is individually scaled in this way according to its local incompleteness, as given by the masks. We note that due to our chosen acceptable minimum incompleteness of 0.7 spheres are never scaled beyond the radius bin $R$ under consideration. Thus each correction applies only to the value of the VPF at each radius point plotted.

We have tested the robustness of our method by comparing measurements of the CPDF using a fully sampled, complete Hubble Volume 2dFGRS mock VLC (Norberg et al. 2002b) with those from the same mock but which have been made artifically incomplete using the survey masks (spectroscopically, and including irregular boundaries and holes) and then corrected. In Fig. 4A.1 we show the results for $P_N$ vs. radius, where $N = 0$ (the VPF), 2, 6, 20 and 70 (note other $N$'s are omitted for clarity, but all behave similarly over the scales where the VPF is of interest to us). Here the points with error bars are the complete $P_N$'s, the solid lines are the equivalent corrected incomplete $P_N$'s, and the dashed lines represent the uncorrected incomplete $P_N$'s. As can be seen, the complete points and corrected lines are fully consistent, whereas the uncorrected values almost always lie off the complete points and well outside their error bars (note the steepness of each curve which is plotted on a log scale). The $P_0$ curve in particular demonstrates that such incompleteness effects must be accounted for to obtain correct void measurements; simply building volume limited catalogues is not enough and will lead to an over-prediction of the scale and frequency of voids in the survey. Our method can be applied to any counts-in-cells analysis where incompleteness in the galaxy distribution is present.

PSfrag replacements

$\bar{N}$
$\bar{\xi}$
$\bar{N}\bar{\xi}$
$\chi = \ln(P_0)/\bar{N}$

$b_J$
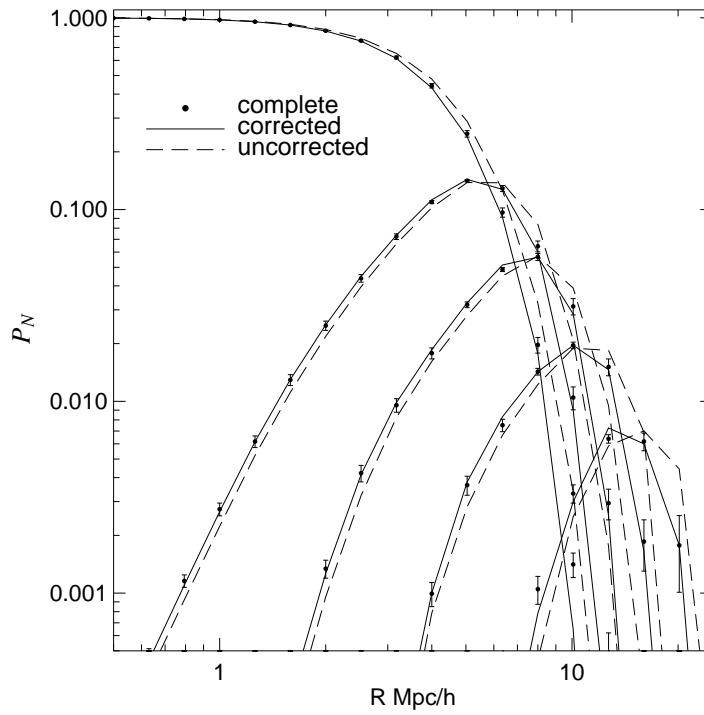
**Figure 4A.1:** Correcting for incompleteness in the 2dFGRS. The CPDF, $P_N$, for a Hubble Volume 2dFGRS mock VLC in the magnitude range $-19 > M_{b_J} - 5\log_{10} > -20$: left to right $N = 0$ (the VPF), 2, 6, 20 and 70. The points with errors represent the complete mock, the solid line is the corrected incomplete mock and the long-dashed line is the uncorrected incomplete mock. Note the uncorrected incomplete mock always lies outside the error bars.

# 5 Luminosity functions by density environment and galaxy type[1]

## Abstract

We use the 2dF Galaxy Redshift Survey to measure the dependence of the $b_J$-band galaxy luminosity function on large-scale environment, defined by density contrast in spheres of radius $8h^{-1}$Mpc, and on spectral type, determined from principal component analysis. We find that the galaxy populations at both extremes of density differ significantly from that at the mean density. The population in voids is dominated by late types and shows, relative to the mean, a deficit of galaxies that becomes increasingly pronounced at magnitudes brighter than $M_{b_J} - 5\log_{10} h \lesssim -18.5$. In contrast, cluster regions have a relative excess of very bright early-type galaxies with $M_{b_J} - 5\log_{10} h \lesssim -21$. Differences in the mid to faint-end population between environments are significant: at $M_{b_J} - 5\log_{10} h = -18$ early and late-type cluster galaxies show comparable abundances, whereas in voids the late types dominate by almost an order of magnitude. We find that the luminosity functions measured in all density environments, from voids to clusters, can be approximated by Schechter functions with parameters that vary smoothly with local density, but in a fashion which differs strikingly for early and late-type galaxies. These observed variations, combined with our finding that the faint-end slope of the overall luminosity function depends at most weakly on density environment, may prove to be a significant challenge for models of galaxy formation.

## 5.1 Introduction

The galaxy luminosity function has played a central role in the development of modern observational and theoretical astrophysics, and is a well established and fundamental tool for measuring the large-scale distribution of galaxies in the universe (Efstathiou, Ellis & Peterson 1988; Loveday et al. 1992; Marzke, Huchra & Geller 1994; Lin et al. 1996; Zucca et al. 1997; Ratcliffe et al. 1998; Norberg et al. 2002b; Blanton et al. 2003a;). The galaxy luminosity function of the 2dF Galaxy Redshift Survey (2dFGRS) has been characterised in several papers: Norberg et al. (2002b) consider the survey as a whole; Folkes et al.

---

(1999) and Madgwick et al. (2002) split the galaxy population by spectral type; De Propris et al. (2003) measure the galaxy luminosity function of clusters in the 2dFGRS; Eke et al. (2004) estimate the galaxy luminosity function for groups of different mass. Such targeted studies are invaluable if one wishes to understand how galaxy properties are influenced by external factors such as local density environment (e.g. the differences between cluster and field galaxies).

A natural extension of such work is to examine a wider range of galaxy environments and how specific galaxy properties transform as one moves between them, from the very under-dense 'void' regions, to mean density regions, to the most over-dense 'cluster' regions. In order to 'connect the dots' between galaxy populations of different type and with different local density a more comprehensive analysis needs to be undertaken. Although progress has been made in this regard on both the observational front (Bromley et al. 1998; Christlein 2000; Hütsi et al. 2002) and theoretical front (Peebles 2001; Mathis & White 2002; Benson et al. 2003; Mo et al. 2004), past galaxy redshift surveys have been severely limited in both their small galaxy numbers and small survey volumes. Only with the recent emergence of large galaxy redshift surveys such as the 2dFGRS and also the Sloan Digital Sky Survey (SDSS) can such a study be undertaken with any reasonable kind of precision (for the SDSS, see recent work by Hogg et al. 2003, Kauffmann et al. 2004, and Hoyle et al. 2005).

In this paper we use the 2dFGRS galaxy catalogue to provide an extensive description of the luminosity distribution of galaxies in the local universe for all density environments within the 2dFGRS survey volume. In addition, the extreme under-dense and over-dense regions of the survey are further dissected as a function of 2dFGRS galaxy spectral type, $\eta$, which can approximately be cast as early and late-type galaxy populations (Madgwick et al. 2002, see Section 5.2). The void galaxy population is especially interesting as it is only with these very large survey samples and volumes possible to measure it with any degree of accuracy. Questions have been raised (e.g., Peebles 2001) as to whether the standard $\Lambda$CDM cosmology correctly describes voids, most notably in relation to reionisation and the significance of the dwarf galaxy population in such under-dense regions.

This paper is organised as follows. In Section 5.2 we provide a brief description of the 2dFGRS and the way in which we measure the galaxy luminosity function from it. The luminosity function results are presented in Section 5.3, and then compared with past results in Section 5.4. We discuss the implications for models of galaxy formation in Section 5.5. Throughout we assume a $\Lambda$CDM cosmology with parameters $\Omega_m = 0.3$, $\Omega_\Lambda = 0.7$, and $H_0 = 100h^{-1}\text{kms}^{-1}\text{Mpc}^{-1}$.

## 5.2 Method

### 5.2.1 The 2dFGRS survey

We use the completed 2dFGRS as our starting point (Colless et al. 2003), giving a total of 221,414 high quality redshifts. The median depth of the full survey, to a nominal magnitude limit of $b_\text{J} \approx 19.45$, is $z \approx 0.11$. We consider the two large contiguous survey regions,

one in the south Galactic pole and one towards the north Galactic pole. To improve the accuracy of our measurement our attention is restricted to the parts of the survey with high redshift completeness (> 70%) and galaxies with apparent magnitude $b_J < 19.0$, well within the above survey limit (see also Appendix 5C). Our conclusions remain unchanged for reasonable choices of both these restrictions. Full details of the 2dFGRS and the construction and use of the mask quantifying the completeness of the survey can be found in Colless et al. (2001, 2003) and Norberg et al. (2002b).

Where possible, galaxy spectral types are determined using the principal component analysis (PCA) of Madgwick et al. (2002) and the classification quantified by a spectral parameter, $\eta$. This allows us to divide the galaxy sample into two broad classes, conventionally called late and early types for brevity. The late types are those with $\eta \geq -1.4$ that have active star formation and the early types are the more quiescent galaxy population with $\eta < -1.4$. Approximately 90% of the galaxy catalogue can be classified in this way. This division at $\eta = -1.4$ corresponds to an obvious dip in the $\eta$ distribution (Section 5.2.4; see also Madgwick et al. 2002) and a similar feature in the $b_J - r_F$ colour distribution, and therefore provides a fairly natural partition between early and late types. When calculating each galaxy's absolute magnitude we apply the spectral type dependent $k+e$ corrections of Norberg et al. (2002b); when no type can be measured we use their mean $k + e$ correction. In this way all galaxy magnitudes have been corrected to zero redshift.

## 5.2.2 Local density measurement

The 2dFGRS galaxy catalogue is *magnitude limited*; it has a fixed apparent magnitude limit which corresponds to a faint absolute magnitude limit that becomes brighter at higher redshifts. Over any given range of redshift there is a certain range of absolute magnitudes within which all galaxies can be seen by the survey and are thus included in the catalogue (apart from a modest incompleteness in obtaining the galaxies' redshifts). Selecting galaxies within these redshift and absolute magnitude limits defines a *volume-limited* subsample of galaxies from the magnitude-limited catalogue (see e.g. Norberg et al. 2001, 2002b; Croton et al. 2004b); this sub-sample is complete over the specified redshift and absolute magnitude ranges.

To estimate the local density for each galaxy we first need to establish a volume-limited *density defining population* (DDP) of galaxies. This population is used to fix the density contours in the redshift space volume containing the magnitude-limited galaxy catalogue. We restrict the magnitude-limited survey to the redshift range $0.05 < z < 0.13$, giving an effective sampling volume of approximately $7 \times 10^6 h^{-3} \text{Mpc}^3$. Such a restriction guarantees that all galaxies in the magnitude range $-19 > M_{b_J} - 5 \log_{10} h > -22$ (i.e. effectively brighter than $M^* + 0.7$) are volume limited, and allows us to use this sub-population as the DDP. The mean number density of DDP galaxies is $8.6 \times 10^{-3} h^3 \text{Mpc}^{-3}$. In Appendix 5B we consider the effect of changing the magnitude range of the DDP and find only a very small difference in our final results.

The local density contrast for each magnitude-limited galaxy is determined by counting the number of DDP neighbours within an $8h^{-1}\text{Mpc}$ radius, $N_g$, and comparing this with

the expected number, $\bar{N}_g$, obtained by integrating under the published luminosity 2dFGRS function of Norberg et al. (2002b) over the same magnitude range that defines the DDP:

$$\delta_8 \equiv \frac{\delta\rho_g}{\rho_g} = \left.\frac{N_g - \bar{N}_g}{\bar{N}_g}\right|_{R=8h^{-1}\text{Mpc}}. \tag{5.1}$$

In Appendix 5B we explore the effect of changing this smoothing scale from between $4h^{-1}$Mpc to $12h^{-1}$Mpc. We find that our conclusions remain unchanged, although, not surprisingly, smaller scale spheres tend to sample the under dense regions differently. Spheres of $8h^{-1}$Mpc are found to be the best probe of both the under and over-dense regions of the survey.

With the above restrictions, the magnitude-limited galaxy sample considered in our analysis contains a total of $81,387$ ($51,596$) galaxies brighter than $M_{\text{b}_\text{J}} - 5\log_{10}h = -17$ ($-19$), with $30,354$ ($23,043$) classified as early types and $42,772$ ($23,815$) classified as late types. Approximately 70% of all galaxies in this sample are sufficiently within the survey boundaries to be given a local density. Details of the different sub-samples binned by local density and type are given in Table 5.1.

### 5.2.3 Measuring the luminosity function

The luminosity function, giving the number density of galaxies as a function of luminosity, is conveniently approximated by the Schechter function (Schechter 1976, see also Norberg et al. 2002b):

$$d\phi = \phi^*(L/L^*)^\alpha \exp(-L/L^*)\, d(L/L^*), \tag{5.2}$$

dependent on three parameters: $L^*$ (or equivalently $M^*$), providing a characteristic luminosity (magnitude) for the galaxy population; $\alpha$, governing the faint-end slope of the luminosity function; and $\phi^*$, giving the overall normalisation. Our method, which we describe below, will be to use the magnitude-limited catalogue binned by density and type to calculate the shape of each luminosity function, draw on restricted volume-limited sub-samples of each to fix the correct luminosity function normalisation, then determine the maximum likelihood Schechter function parameters for each in order to quantify the changing behaviour between different environments.

The luminosity function shape is determined in the standard way using the step-wise maximum likelihood method (SWML Efstathiou, Ellis & Peterson 1988) and the STY estimator (Sandage, Tammann & Yahil 1979). See Norberg et al. (2002b) for a complete description of the application of these two techniques to the 2dFGRS. All STY fits are performed over the magnitude range $-17 > M_{\text{b}_\text{J}} - 5\log_{10}h > -22$.

Such techniques fail to provide the luminosity function normalisation, however, and one needs to consider carefully how to do this when studying galaxy populations in different density environments. To normalise each luminosity function we employ a new counts in cells (CiC) technique which directly calculates the number density of galaxies as a function of galaxy magnitude from the galaxy distribution. Briefly, this is achieved by counting galaxies in restricted volume-limited sub-regions of the survey. We discuss our
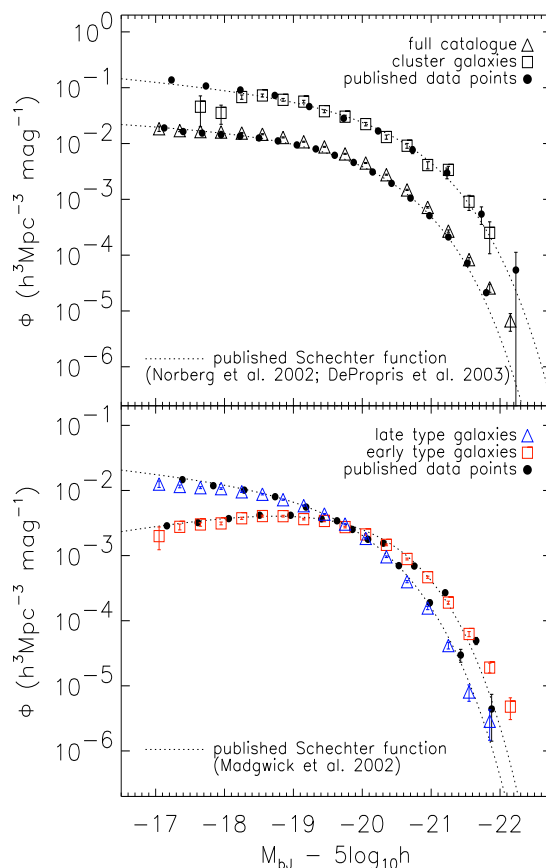
**Figure 5.1:** A comparison of the published 2dFGRS luminosity function (circles and dotted lines) to that calculated by our joint SWML(shape)/CiC(normalisation) method (squares and triangles) for select galaxy samples. Shown are the (top) full catalogue luminosity function (Norberg et al. 2002b) and cluster galaxy population luminosity function (De Propris et al. 2003), and (bottom) the luminosity function for early and late-type galaxy sub-samples separately (Madgwick et al. 2002).

CiC method in more detail in Appendix 5A. As we show there, when galaxy numbers allow a good statistical measurement the luminosity function shape determined by the SWML and CiC methods agree very well. As the SWML estimator draws from the larger magnitude-limited survey rather than the smaller CiC volume-limited sub-samples, we choose the above two-step SWML/CiC approach rather than the CiC method alone to obtain the best results for each luminosity function. Once the CiC luminosity function has been calculated for the same galaxy sample, the SWML luminosity function is then given the correct amplitude by requiring that the number density integrated between the
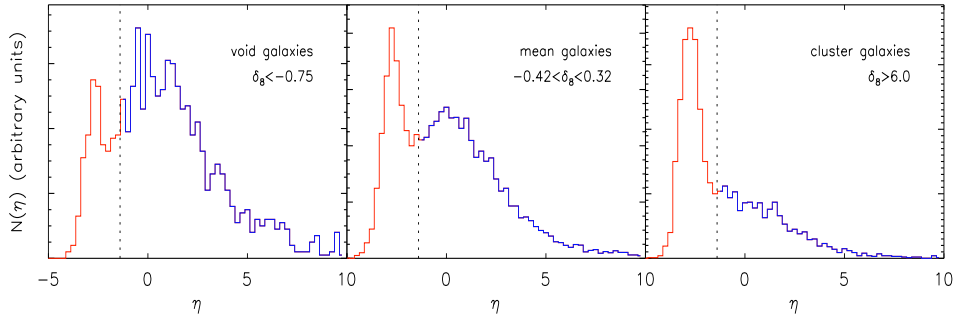
**Figure 5.2:** The distribution of the spectral parameter, $\eta$, for the void, mean, and cluster galaxies used in our analysis (Table 5.1). The vertical dotted line at $\eta = -1.4$ divides the quiescent galaxy population (early types on left) from the more active star-forming galaxies (late types on right). From void to cluster environment, the dominant galaxy population changes smoothly from late-type to early-type.

magnitude range $-19 > M_{b_J} - 5\log_{10} h > -22$ be the same as that for the CiC result.

### 5.2.4 Comparison to previous 2dFGRS results

In Fig. 5.1 we give a comparison of our measured luminosity functions for selected galaxy populations with the equivalent previously-published 2dFGRS results (see each reference for complete details). These include (top panel) the full survey volume (Norberg et al. 2002b) and cluster galaxy luminosity functions (De Propris et al. 2003), and (bottom panel) the luminosity functions derived for late and early-type galaxy populations separately (Madgwick et al. 2002). For all, the squares and triangle symbols show our hybrid SWML/CiC values while the circles and dotted lines give the corresponding published 2dFGRS luminosity function data points and best Schechter function estimates, respectively. The close match between each set of points confirms that our method is able to reproduce the published 2dFGRS luminosity shape and amplitude successfully.

There are a few points to note. Firstly, the cluster luminosity function is not typically quoted with a value of $\phi^*$ since the normalisation of the cluster galaxy luminosity distribution will vary from cluster to cluster (dependent on cluster richness). Because of this we plot the De Propris et al. cluster luminosity function using our $\phi^*$ value.

Secondly, the Madgwick et al. early and late-type galaxy absolute magnitudes include no correction for galaxy evolution, which, if included, would have the effect of dimming the galaxy population somewhat. We have checked the significance of omitting the evolution correction when determining the galaxy absolute magnitudes and typically find only minimal differences in our results and no change to our conclusions.

Thirdly, the STY Schechter function values we measure tend to present a slightly 'flatter' faint-end slope than seen for the full survey: our all-type STY estimate returns $\alpha =$

−1.05 ± 0.02 (Table 5.1) whereas for the completed survey (across the redshift range 0.02 < $z$ < 0.25) the recovered $\alpha$ value is −1.18 ± 0.02 (Cole et al. 2005). This difference is due primarily to three systematic causes: the minimum redshift cut required to define the DDP which results in a restricted absolute magnitude range over which we can measure galaxies; the non-perfect description of the galaxy luminosity function by a Schechter function together with the existing degeneracies in the $M^* − \alpha$ plane; the sensitivity of the faint-end slope parametrisation to model dependent corrections for missed galaxies. For our results, these systematic effects do not hinder a comparison between sub-samples, but it is essential to take into account the different cuts we imposed for any detailed comparison with other works. In Appendix 5C we discuss these degeneracies and correlations further. We test their influence by fixing each $\alpha$ at the published field value when applying the STY estimator and find a typical variation of less than 0.2 magnitudes in $M^*$ from the main results presented in Section 5.3. Such systematics do not change our conclusions.

Lastly, the 2dFGRS photometric calibrations have improved since earlier luminosity function determinations, and thus the good match seen in Fig. 5.1 demonstrates that the new calibrations have not significantly altered the earlier results.

In Fig. 5.2 we show the $\eta$ distribution for our void, mean, and cluster galaxy samples. The mean galaxy distribution is essentially identical to that shown in Fig. 4 of Madgwick et al. (2002) for the full survey, demonstrating that the mean density regions contain a similar mix of galaxy types to that of the survey as a whole. For under-dense regions late types progressively dominate, while the converse is true in the over-dense regions. This behaviour can be understood in terms of the density-morphology relation (e.g. Dressler 1980), and will be explored in more detail in the next section.

## 5.3 Results

### 5.3.1 Luminosity functions

The top panel of Fig. 5.3 shows the 2dFGRS galaxy luminosity function estimated for the six logarithmically-spaced density bins and additional extreme void bin, $\delta_8 < −0.9$, given in Table 5.1. The luminosity function varies smoothly as one moves between the extremes in environment. Each curve shows the characteristic shape of the Schechter function, for which we show the STY fit across the entire range of points plotted with dotted lines. The Schechter parameters are given in Table 5.1, along with the number of galaxies considered in each density environment and the volume fraction they occupy. A number of points of interest regarding the variation of these parameters with local density will be discussed below.

To examine the relative differences in the void and cluster galaxy populations with respect to the mean, in the bottom panel of Fig. 5.3 we plot the ratio of the void and cluster luminosity functions to the mean luminosity function. Also shown is the ratio of the corresponding Schechter functions to the mean Schechter function (solid lines) and $1\sigma$ uncertainty (dotted lines, where only the error in $M^*$ and $\alpha$ has been propagated). For a

| Galaxy Type | Galaxy Sample | $\delta_{8_{min}}$ | $\delta_{8_{max}}$ | $N_{GAL}$ | $f_{VOL}$ | $M^*$ $M_{b_J} - 5\log_{10} h$ | $\alpha$ | $\phi^*$ $10^{-3} h^3 \mathrm{Mpc}^{-3}$ | $\langle \rho_L \rangle$ $10^8 h \mathrm{L}_\odot \mathrm{Mpc}^{-3}$ |
|---|---|---|---|---|---|---|---|---|---|
| all types: | full volume | −1.0 | ∞ | 81, 387 | 1.0 | −19.65 ± 0.02 | −1.05 ± 0.02 | 21.3 ± 0.5 | 2.10 ± 0.08 |
| | extreme void | −1.0 | −0.90 | 260 | 0.09 | −18.26 ± 0.33 | −0.81 ± 0.50 | 3.17 ± 0.90 | 0.08 ± 0.04 |
| | void | −1.0 | −0.75 | 1, 157 | 0.20 | −18.84 ± 0.16 | −1.06 ± 0.24 | 3.15 ± 0.56 | 0.15 ± 0.04 |
| | | −0.75 | −0.43 | 3, 331 | 0.19 | −19.20 ± 0.10 | −0.93 ± 0.11 | 5.99 ± 0.62 | 0.36 ± 0.05 |
| | mean | −0.43 | 0.32 | 11, 877 | 0.30 | −19.44 ± 0.05 | −0.94 ± 0.05 | 11.3 ± 0.7 | 0.86 ± 0.07 |
| | | 0.32 | 2.1 | 21, 989 | 0.24 | −19.64 ± 0.04 | −0.99 ± 0.04 | 22.9 ± 1.0 | 2.16 ± 0.13 |
| | | 2.1 | 6.0 | 15, 656 | 0.07 | −19.85 ± 0.05 | −1.09 ± 0.04 | 49.0 ± 3.0 | 5.95 ± 0.49 |
| | cluster | 6.0 | ∞ | 3, 175 | 0.01 | −20.08 ± 0.13 | −1.33 ± 0.11 | 60.7 ± 13.2 | 11.6 ± 3.4 |
| late type: | full volume | −1.0 | ∞ | 42, 772 | − | −19.30 ± 0.03 | −1.03 ± 0.03 | 15.0 ± 0.5 | 1.06 ± 0.05 |
| | void | −1.0 | −0.75 | 855 | − | −18.78 ± 0.19 | −1.14 ± 0.24 | 2.42 ± 0.55 | 0.11 ± 0.04 |
| | | −0.75 | −0.43 | 2, 249 | − | −19.07 ± 0.12 | −0.95 ± 0.14 | 4.54 ± 0.58 | 0.25 ± 0.05 |
| | mean | −0.43 | 0.32 | 7, 261 | − | −19.24 ± 0.07 | −1.00 ± 0.07 | 8.03 ± 0.61 | 0.53 ± 0.06 |
| | | 0.32 | 2.1 | 11, 921 | − | −19.36 ± 0.06 | −1.04 ± 0.05 | 15.5 ± 1.0 | 1.17 ± 0.11 |
| | | 2.1 | 6.0 | 7, 596 | − | −19.37 ± 0.07 | −1.03 ± 0.07 | 36.3 ± 2.9 | 2.73 ± 0.31 |
| | cluster | 6.0 | ∞ | 1, 316 | − | −19.34 ± 0.18 | −1.09 ± 0.20 | 54.0 ± 12.2 | 4.09 ± 1.31 |
| early type: | full volume | −1.0 | ∞ | 30, 354 | − | −19.65 ± 0.03 | −0.65 ± 0.03 | 8.80 ± 0.22 | 0.75 ± 0.03 |
| | void | −1.0 | −0.75 | 220 | − | −18.62 ± 0.33 | −0.15 ± 0.53 | 0.67 ± 0.10 | 0.02 ± 0.01 |
| | | −0.75 | −0.43 | 861 | − | −19.16 ± 0.14 | −0.43 ± 0.24 | 1.62 ± 0.17 | 0.88 ± 0.02 |
| | mean | −0.43 | 0.32 | 3, 873 | − | −19.38 ± 0.08 | −0.39 ± 0.11 | 4.13 ± 0.19 | 0.27 ± 0.02 |
| | | 0.32 | 2.1 | 8, 809 | − | −19.59 ± 0.05 | −0.52 ± 0.06 | 10.6 ± 0.4 | 0.84 ± 0.05 |
| | | 2.1 | 6.0 | 7, 163 | − | −19.89 ± 0.06 | −0.81 ± 0.06 | 24.2 ± 1.6 | 2.67 ± 0.23 |
| | cluster | 6.0 | ∞ | 1, 731 | − | −20.13 ± 0.18 | −1.12 ± 0.14 | 37.1 ± 7.7 | 6.00 ± 1.75 |

**Table 5.1:** Properties of our magnitude-limited galaxy samples, split by spectral type (all, early and late) and in seven density ranges (defined by $\delta_{8_{min}}$ and $\delta_{8_{max}}$, the density contrast in spheres of radius $8h^{-1}$Mpc). The all-type sample is also split into an 'extreme void' sample. $N_{GAL}$ and $f_{VOL}$ are the number of galaxies in each density bin and the volume fraction these galaxies occupy, respectively. $f_{VOL}$ is given for all galaxy types only: early/late-type density populations are just sub-divisions of the associated all-type sample. $M^*$ and $\alpha$ are the likelihood estimated Schechter function parameters, and $\phi^*$ the associated normalisation. The integrated luminosity density, as defined by Eq. 5.3 with $L_{min} = 0$, is given in the last column. All errors on the derived parameters reflect only the associated statistical uncertainty.
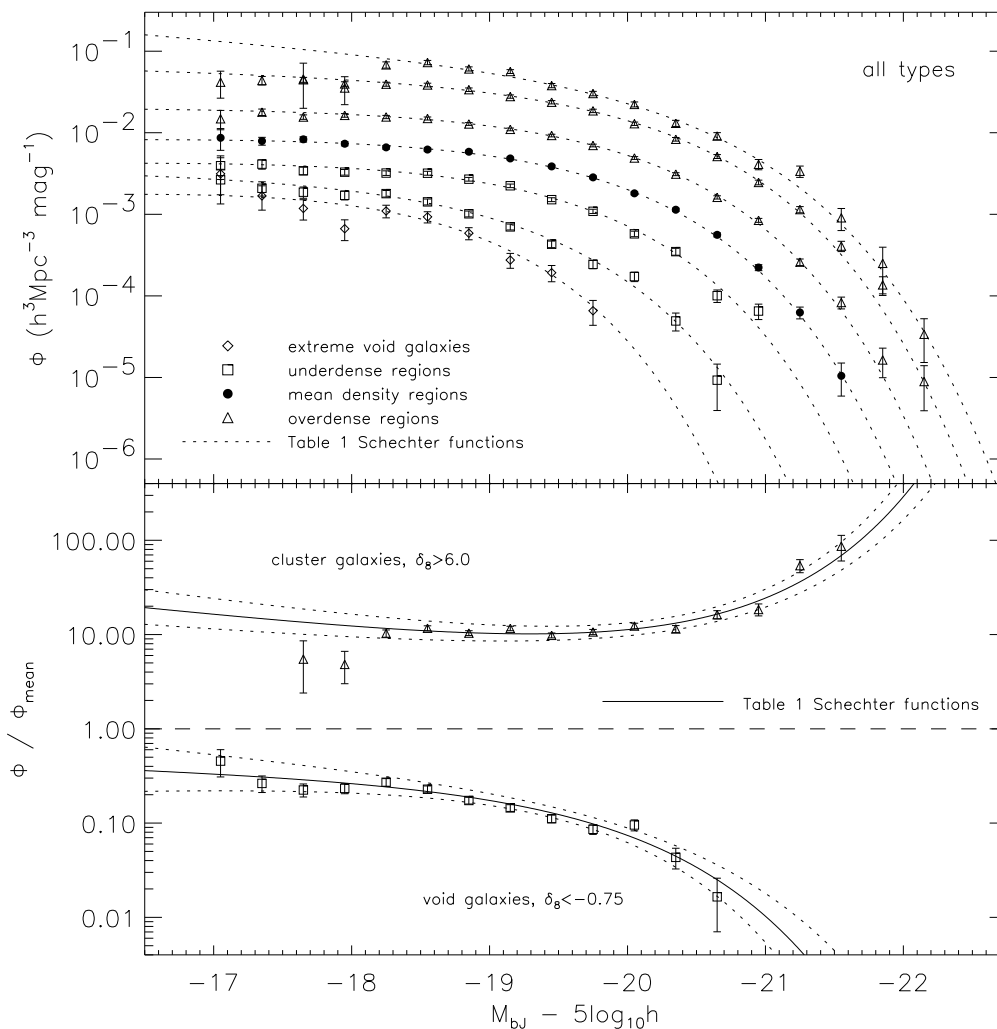
**Figure 5.3:** (top) The SWML luminosity functions for the 2dFGRS galaxy catalogue
in regions of the survey of varying density contrast, $\delta_8$, from void to mean
density to cluster. The best-fit Schechter function parameters for each are
given in Table 5.1 and the corresponding Schechter function curves are over
plotted here with dotted lines. (bottom) The void and cluster luminosity
functions normalised to the mean luminosity function so as to highlight the
relative differences in the shape of each distribution. The solid lines and
bounding dotted lines show the appropriate Table 5.1 Schechter functions
normalised to the mean Schechter function and $1\sigma$ uncertainty.

non-changing luminosity function shape, this ratio is a flat line whose amplitude reflects the relative abundance of the samples considered. For two Schechter functions differing in both $\alpha$ and $M^*$, the faint-end of the ratio is most sensitive to the differences in $\alpha$ and the bright end to the differences in $M^*$. We note that the error regions on the Schechter function fits shown here do not include the uncertainty of the mean sample, as the correlation of its error with the other samples is unknown. This panel reveals significant shifts in abundances at the bright end: in voids there is an increasing deficit of bright galaxies for magnitudes $M_{b_J} - 5 \log h \lesssim -18.5$, while clusters exhibit an excess of very luminous galaxies at magnitudes $M_{b_J} - 5 \log h \lesssim -21$.

It is well-established that early and late-type galaxy populations have very different luminosity distributions (Fig. 5.1). In Fig. 5.4 we explore the density dependence of these populations. The upper panels show the luminosity functions and their Schechter function fits, as in Fig. 5.3, but for (left panel) early types and (right panel) late types separately. In the corresponding lower panels we show the ratio of each extreme density population to the mean density luminosity function, following the same format as the bottom panel of Fig. 5.3. (We note that the mean luminosity functions for each type used in this figure are both very similar in shape to that shown in the bottom panel of Fig. 5.1). The best-fit Schechter parameters are given in Table 5.1. Again we see a smooth transition in the galaxy luminosity function as one moves through regions of different density contrast. The lower left panel of Fig. 5.4 shows a significant variation of the bright end early-type galaxy population with respect to the mean, while at the faint end the changes are more ambiguous, but with Schechter fits that suggest some evolution into the denser regions. Note that, although the faint end of our early-type cluster Schechter function is primarily constrained by the mid-luminosity galaxies in the sample, our maximum liklihood Schechter parameters are quite close to that found by De Propris et al. (2003) for a comparable galaxy population but measured approximately three magnitudes fainter. In contrast to the early types, in the lower right panel of Fig. 5.4 late-type galaxies show little change in relative population between the mean and cluster environments and a possible "tilt" favouring the faint-end for low-density environments. Due to deteriorating statistics we do not consider the type dependent extreme void luminosity function which was introduced in Fig. 5.3.

The essence of our results is best appreciated when we directly compare the early and late-type galaxy distributions, separately for the cluster and void regions of the survey, as shown in Fig. 5.5. This figure reveals a striking contrast: the void population is composed primarily of medium to faint luminosity late-type galaxies, while for the cluster population early types dominate down to all but the faintest magnitude considered. This is the central result of our study, and shows the crucial role of accurately determining the amplitude of the luminosity function, since the shape alone does not necessarily determine the dominant population of a region.

### 5.3.2 Evolution with environment

It is well known that the Schechter function parameters are highly correlated. In Fig. 5.6 we show the $1\sigma$ (68% 2-parameter) and $3\sigma$ (99% 2-parameter) $\chi^2$ contours in the $M^* - \alpha$
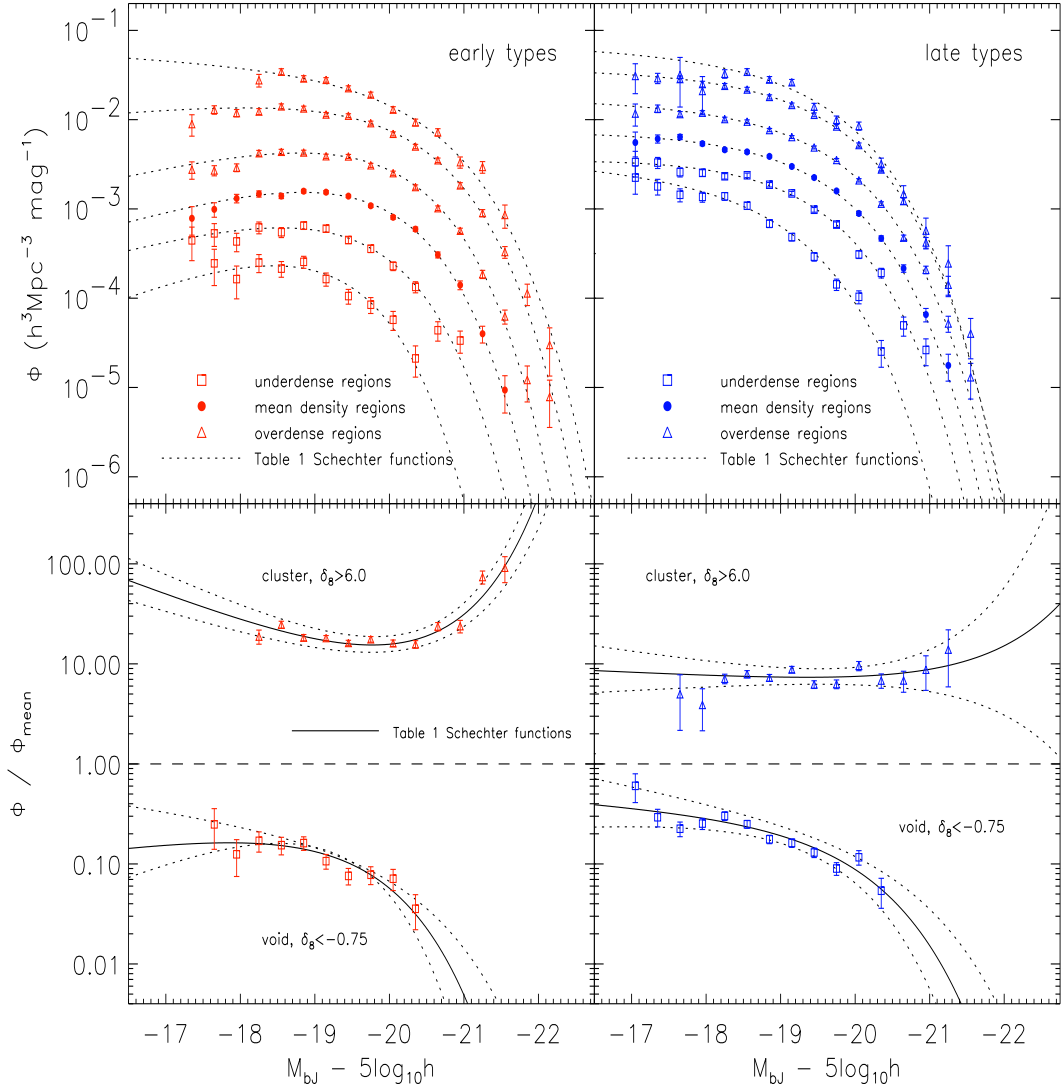
**Figure 5.4:** Comparing both the (top) absolute and (bottom) relative distributions of (left) early-type galaxies in different density environments, and (right) late-type galaxies in different density environments. In the bottom panels the luminosity functions have again been normalised to the mean (each to their respective type) as done previously in Fig. 5.3 (note that the shape of the mean for each type is very similar to that shown in Fig. 5.1). Here the solid lines and bounding dotted lines show the appropriate Table 5.1 Schechter functions normalised to the mean Schechter function and $1\sigma$ uncertainty.
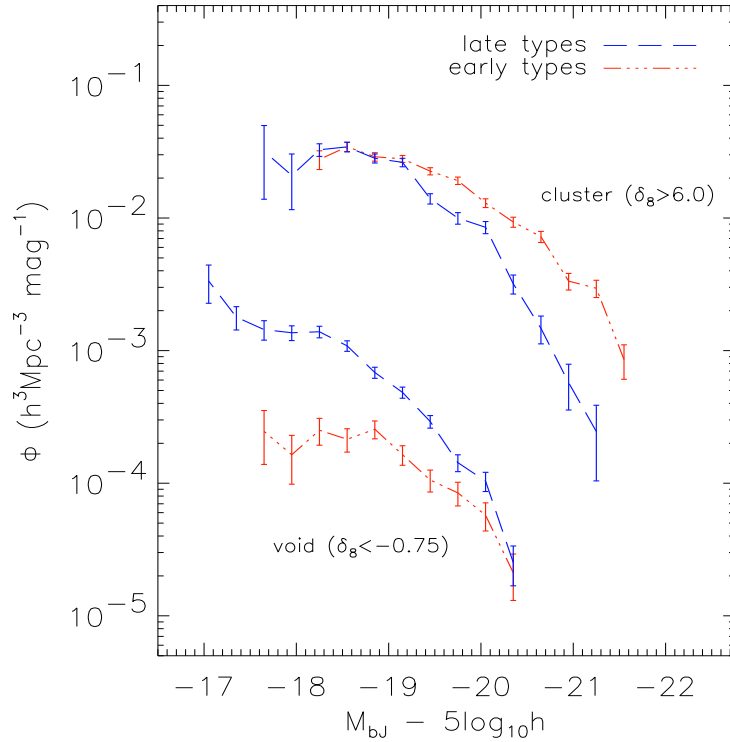
**Figure 5.5:** A direct comparison of the early and late-type galaxy populations in the cluster environment (top two luminosity functions) and void regions of the survey (bottom two luminosity functions). The void population is composed almost exclusively of faint late-type galaxies, while in the clusters regions the galaxy population brighter than $M_{b_J} - 5\log_{10} h = -19$ consists predominantly of early types.

plane for the early-type, late-type, and combined type cluster and void populations. For a given spectral type, all show a greater than $3\sigma$ difference in the STY Schechter parameters between the void and cluster regions. Intermediate density bins are omitted for clarity but follow a smooth progression with smaller error ellipses between the two extremes shown. In Appendix 5C we explore in more detail the $M^* - \alpha$ degeneracy and confirm that our results are robust.

Our findings show that the galaxy luminosity function changes gradually with environment. We quantify this behaviour in Fig. 5.7 by plotting the variation of $M^*$ and $\alpha$ as a function of density contrast, where points to the left of $\delta_8 = 0$ represent the under-dense to void regions in the survey, and points to the right of this are measured in the over-dense to cluster regions. Late-type galaxies display a consistent luminosity function across all density environments, from sparse voids to dense clusters, with a weak dimming of $M^*$ in the under-dense regions, and an almost constant faint-end slope. In contrast, the luminosity
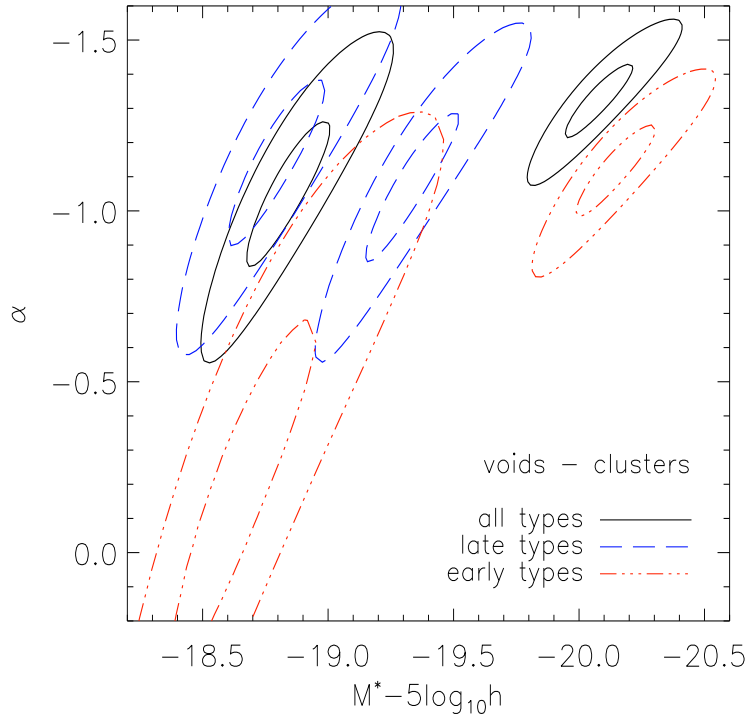
**Figure 5.6:** The $1\sigma$ (68% 2-parameter) and $3\sigma$ (99% 2-parameter) contours of constant $\chi^2$ in the $M^* - \alpha$ plane for the void and cluster STY estimates (in each case the void fit is on the left, corresponding to a fainter M*). Galaxy types are identified by the linestyle given in the legend. Even at the $3\sigma$ level significant differences in the void and cluster Schechter function parameters for each galaxy type can be seen.

distribution of early-type galaxies differs sharply between the extremes in environment: $M^*$ brightens by approximately 1.5 magnitudes going from voids to clusters, while the faint-end slope moves from $\alpha \approx -0.3$ in under-dense regions to around $\alpha \approx -1.0$ in the densest parts of the survey.

Finally, in Fig. 5.8 we plot the mean luminosity per galaxy, $\langle \rho_L \rangle / \langle \rho_g \rangle$, obtained by integrating the luminosity function for each set of Schechter function parameters from Table 5.1:

$$\langle \rho_g \rangle = \int_{L_{min}}^{\infty} \phi(L)\, dL \,, \quad \langle \rho_L \rangle = \int_{L_{min}}^{\infty} \phi(L) L\, dL \,, \tag{5.3}$$

where $L_{min}$ is a somewhat arbitrary observational cutoff chosen at $M_{b_J} - 5 \log_{10} h = -17$. This is both the limit down to which we confidently measure our luminosity functions, and also the limit beyond which the Schechter function no longer provides a good fit to the early-type luminosity function of Madgwick et al. (2002). The final column of Table 5.1
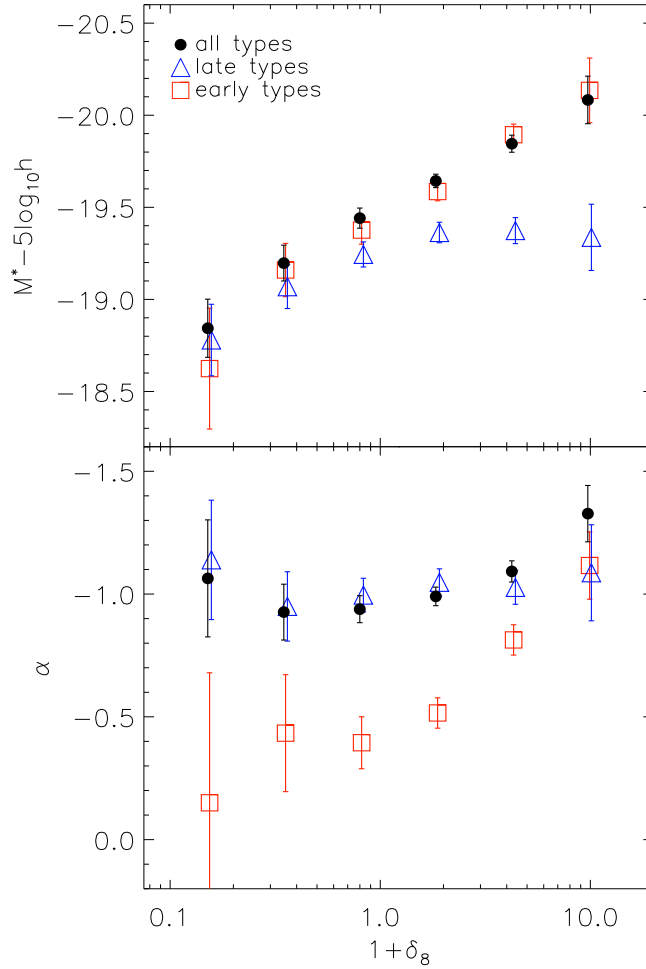
**Figure 5.7:** The maximum liklihood Schechter function $M^*$ and $\alpha$ parameters for each of the six density contrast regions in Table 5.1 (Figs. 5.3 and 5.4). Each panel shows the result for individual samples split by spectral type (early/late) and both types combined.

gives the total luminosity density in the various density contrast environments, computed by integrating the Schechter function with no cutoff, to allow easy comparison with past and future analyses; the contribution to the calculated $\langle \rho_L \rangle$ from luminosities below the observational cutoff is less than a few percent. We note that $\langle \rho_g \rangle$ is directly related to the density contrast, $\delta_8$, by definition. It is interesting to see that the early-type galaxies in Fig. 5.8 are, on average, about a factor of two brighter per galaxy than the late types, even though the late types dominate in terms of both number and luminosity density. For all galaxy populations, the mean luminosity per galaxy shows a remarkable constancy across

84
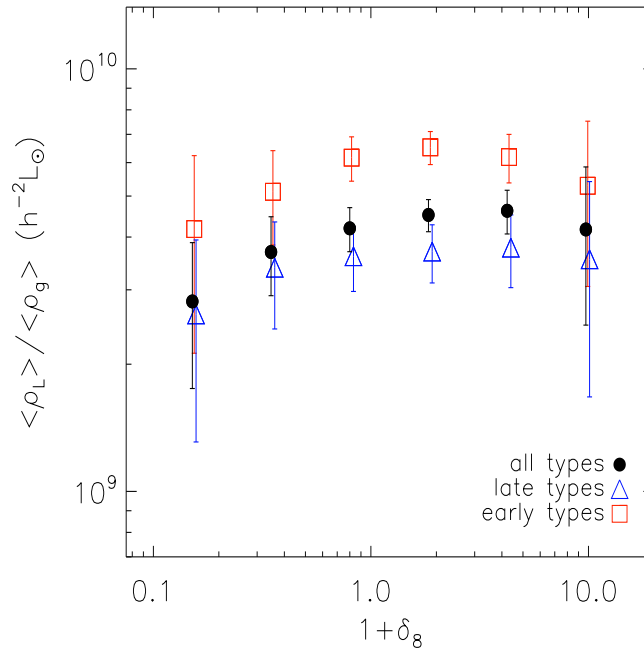
**Figure 5.8:** The mean luminosity per galaxy as a function of density environment for each galaxy type, calculated from Eq. 6.3 using the Schechter function parameters given in Table 5.1. The integral is performed by choosing $L_{min}$ so that $M_{min} - 5 \log_{10} h = -17$ (Section 5.3.2). The mean luminosity per galaxy of early types is consistently about a factor of two brighter than their late type counterparts across all density environments.

the full range of density environments.

## 5.4 Comparison to previous work

Historically, work on the dependence of the luminosity function on large scale environment has been restricted primarily to comparisons between cluster and field galaxies, due to insufficient statistics to study voids. (Note that 'field' samples are usually flux-limited catalogues which cover all types of environments.) One of the aims of this work is to elucidate the properties of galaxies in void environments and understand the relationship between clusters and voids. In this section, we briefly summarise previous observations and compare them with the results presented in Section 5.3.

We have already shown in Fig. 5.1 and Section 5.2 that our cluster and field results are equivalent to the published 2dFGRS luminosity function results of Norberg et al. (2002b), Madgwick et al. (2002), and De Propris et al. (2003). The latter paper explains their cluster luminosity function by demonstrating that the field luminosity function can be ap-

proximately transformed into the cluster luminosity function using a simple model where the cluster environment suppresses star formation to produce a dominant bright, early-type population (see Section 4.4 of their paper for details). We expand upon such models in the next section.

Bromley et al. (1998) considered $18,278$ galaxies in the Las Campanas Redshift Survey (LCRS) as a function of spectral type and high and low local density. We confirm (e.g., Fig. 5.7) their qualitative finding that for early-type galaxies the faint-end slope steepens with density whereas late-type objects show little or no significant trend. We cannot make a quantitative comparison to their result because they do not give the definition of their low density sample.

Hütsi et al. (2003) use the Early Data Release of the Sloan Digital Sky Survey (SDSS) and the LCRS to consider the galaxy luminosity function as a function of density field, but in two-dimensional projection so their results are not directly comparable to ours. They find a faint-end slope of $\alpha \approx -1.1$ in all environments and an increase in $M^*$ of roughly 0.3 magnitudes between the under and over-dense portions of their data. This is broadly consistent with the more detailed results obtained here with the full 2dFGRS catalogue when one averages over our two most underdense bins and three most over-dense. In separate work, these authors also consider the environmental dependence of cluster and supercluster properties in the SDSS and LCRS (Einasto et al. 2003a, 2003b). They show an almost order of magnitude increase in the mean cluster luminosity between extremes in density (defined in two dimensions by smoothing over a projected $10h^{-1}$Mpc radius around each cluster). A comparison of their results to ours (i.e. Fig. 5.7) suggests a correlation between galaxy, galaxy group, and galaxy cluster properties in a given density environment. A more detailed exploration would shed light on the connection between virialised objects of different mass with local density. We defer such an investigation to later work.

In a series of papers, members of the SDSS team undertook an analysis of the properties of galaxy samples drawn from under-dense regions in the SDSS (Rojas et al. 2004, 2005; Goldberg et al. 2004; Hoyle et al. 2003). Of most relevance to our study is the work of Hoyle et al. who completed a preliminary analysis of the SDSS void luminosity function, defined in regions of $\delta_7 < -0.6$ using a smoothing scale of $7h^{-1}$Mpc. Their sample of $1,010$ void galaxies are typically fainter and bluer than galaxies in higher density environments but with a similar faint-end slope. Their results are consistent with what we find using a sample which contains about twice the number of void galaxies as defined by Hoyle et al.. Using the same void galaxy catalogue, Rojas et al. (2005) show that this behaviour is not merely an extrapolation of the density-morphology relationship (e.g. Dressler 1980) into sparser environments. By measuring the concentration and Sersic indices (Sersic 1968, Blanton et al. 2003b) of void and field galaxies they detect no significant shift in the morphological mix, even though their void galaxy sample is shown to be significantly bluer.

Also using the SDSS dataset, Hogg et al. (2003) consider the mean environment as a function of luminosity and colour of $115,000$ galaxies, on smoothing scales of 1 and $8h^{-1}$Mpc. They find that their reddest galaxies show strong correlations of luminosity

| Region | Observation | Process |
|--------|-------------|---------|
| Voids | | 1. galaxies typically reside at the centre |
| | faint, late type | of low mass dark halos ($\Rightarrow$ faint) |
| | galaxies dominate | 2. gas is available for star formation ($\Rightarrow$ blue) |
| | | 3. merger rate is low ($\Rightarrow$ spirals) |
| Clusters | | 1. typically satellite and central galaxies of |
| | mid-bright, early-type | massive dark halos ($\Rightarrow$ mid-bright) |
| | galaxies dominate | 2. gas is unavailable for star formation ($\Rightarrow$ red) |
| | | 3. merger rate is high ($\Rightarrow$ ellipticals) |

**Table 5.2:** A summary of our main results, drawing on the work of De Propris et al. (2003) and Mo et al. (2004) to interpret the observed behaviour in Figs. 5.5 and 5.7 in terms of physical processes which govern the void and cluster galaxy populations.

with local density at both the faint and bright extremes, whereas the luminosities of blue galaxies have little dependence on environment. These conclusions are consistent with the present results for our early (red) and late (blue) type luminosity functions (Fig. 5.7). However by restricting attention to the *average* environment of a galaxy of given luminosity and colour, their sample is by definition dominated by galaxies in over-dense environments. The measures they consider are therefore insensitive to one of the main questions of interest to us here, namely whether the characteristic galaxy population in the voids is distinctively different from that in other density environments. Indeed, we clearly find evidence for a population which is particularly favoured in void regions, namely faint late-type galaxies (Fig. 5.5).

## 5.5 Discussion

As clusters are comparatively well-studied objects, and have already been addressed using the 2dFGRS by De Propris et al. (2003), we focus here primarily on a discussion of the voids.

A detailed analysis of void population properties has recently become possible due to significant improvements in the quality of both theoretical modelling and observational data, as summarised by Benson et al. (2003). Peebles (2001) has argued that, visually, observed voids do not match simulated ones and discussed several statistical measures for quantifying a comparison, primarily the distance to the nearest neighbour in a reference sample. However the cumulative distributions of nearest neighbour distances shown in Figs. 4–6 of Peebles (2001) show very little difference between the reference–reference and test–reference distributions. It is not surprising that these statistical measures are insensitive to a void effect, since they are dominated by cluster galaxies. Our method is designed to overcome this difficulty by explicitly isolating the void population of galaxies so that their properties can be studied.

Motivated by the claims of discrepancies in Peebles (2001), Mathis & White (2002) in-

vestigated the nature of void galaxies using N-body simulations with semi-analytic recipes for galaxy formation. They call into question the assertion of Peebles (2001) that $\Lambda$CDM predicts a population of small haloes in the voids, concluding that "the population of faint galaxies...does not constitute a void population". More specifically, they find that all types of galaxies tend to avoid the void regions of their simulation, down to their resolution limit of $M_B = -16.27$ in luminosity and $M_B = -18.46$ in morphology.

The abundance of faint galaxies we find in the void regions of the 2dFGRS seems to be at odds with the Mathis & White predictions. However their results rely on the Peebles (2001) cumulative distribution of galaxies as a function of over density (their Fig. 3) which, like cumulative distributions in general, are rather insensitive to numerically-minor components of the galaxy population. Note that Mathis & White define density contrast using the dark matter mass distribution smoothed over a 5 $h^{-1}$Mpc sphere, whereas we measure the density contrast by galaxy counts. Another possible source of discrepancy is the uncertainties in their semi-analytic recipes, such as the implementation of supernova feedback, which can strongly effect the faint-end luminosity distribution.

There has been recent discussion in the literature about the nature of the faint-end galaxy population and its dependence on group and cluster richness. Most notably, Tully et al. (2002) show a significant steepening in the faint-end population as one considers nearby galaxy groups of increasing richness, from the Local Group to Coma. On the surface of it, this might seem at variance with our results, which are rather better described by a faint-end slope which is approximately constant with changing density environment for the full 2dFGRS galaxy sample (Fig. 5.7). However the steepening of the faint-end slope they find primarily occurs at magnitudes fainter than $M_B = -17$, which is beyond the limit we can study with our sample. Also, their analysis focuses on individual groups of galaxies, while we have chosen to work with a much bigger galaxy sample and have smoothed it over a scale much larger than the typical cluster. Indeed, as discussed in Appendix 5B, when the smoothing scale is significantly larger than the characteristic size of the structures being probed it is possible that the Schechter function parameters may become insensitive to the small scale shifts in population. This effect, of course, would be less significant for survey regions which host clusters of clusters (i.e. super-clusters), and which are prominently seen in the 2dFGRS (Baugh et al. 2004, Croton et al. 2004b). When sampling the 2dFGRS volume the trend with density that one sees using $4h^{-1}$ Mpc spheres in Fig. 5B.1 is consistent with the Tully et al. result, although one needs to additionally understand the influences of Poisson noise.

Tully et al. attribute their results to a process of photoionisation of the IGM which suppresses dwarf galaxy formation. Over-dense regions, which at later times become massive clusters, typically collapse early and thus have time to form a dwarf galaxy population before the epoch of reionisation. Under-dense regions, on the other hand, begin their collapse at much later times and are thus subject to the photoionisation suppression of cooling baryons. This, they argue, explains the significant increase between the dwarf populations of the Local Group (low density environment) and Coma (over-dense environment). Although suggestive, a deeper understanding of what is happening will require a much more statistically significant sample.

Recently Mo et al. (2004) have considered the dependence of the galaxy luminosity function on large scale environment in their halo occupation model. In this model, the mass of a dark matter halo alone determines the properties of the galaxies. They create mock catalogues built with a halo-conditional luminosity function (Yang et al. 2003) which is constrained to reproduce the overall 2dFGRS luminosity function and correlation length for both luminosity and type. They analyse their data by smoothing over spheres of radius $8 \, h^{-1}$Mpc in their mock catalogue, and measure the luminosity function as a function of density contrast. Their work is performed in real space while we are restricted to work in redshift space. Nonetheless, their predictions qualitatively match our density-dependent luminosity functions; a quantitative comparison is deferred to subsequent work.

In the framework of the Mo et al. model, the reason the faint-end slope $\alpha$ has such a strong dependence on local density for early types (Fig. 5.7) is that faint ellipticals tend to reside predominantly in cluster-sized halos. The $\alpha$ dependence is weaker for late types because faint later-type galaxies tend to live primarily in less massive haloes, which are present in all density environments. The correlations between dark halo mass and the properties of the associated galaxies are not a fundamental prediction of their model, but are input through phenomenological functions adjusted to give agreement with the 2dFGRS overall luminosity functions by galaxy type. However it would be a non-trivial result if the correlations are the same independently of whether the dark matter halo is in a void or in a cluster. For instance, this property would not apply in models for which reionisation more efficiently prevented star formation in under-dense environments than in over-dense environments, as discussed above.

An interesting consequence of the Mo et al. (2004) model is that the luminous galaxy distribution (which is easy to observe but hard to model) correlates well with the dark halo mass distribution (which is hard to observe but easy to model). If their predictions prove to give a good description of the present data it will lend credence to the underlying assumption of their model—that the environmental dependence of many fundamental galaxy properties are entirely due to the dependence of the dark halo mass function on environment. Exactly why this is would still need to be explained, however such a demonstration may facilitate more detailed comparisons between theory and observation than previously possible.

An important result of our work is presented in Fig. 5.5, where a significant shift in the dominant population between voids and clusters is seen. Such a result points to substantial differences in the evolutionary tracks of cluster and void early-type galaxies. Cluster galaxies have been historically well studied: they are more numerous and much brighter on average, with an evolution dominated by galaxy-galaxy interactions and mergers. In voids, however, the picture is not so clear. A reasonable expectation would be that the dynamical evolution of void galaxies should be much slower due to their relative isolation, with passively evolved stellar populations and morphologies similar to that obtained during their formation. Targeted observational studies of void early-type galaxies may reveal much about the high redshift formation processes that go into making such rare objects.

Table 5.2 summarises our main results and provides a qualitative or mnemonic interpretation based on our observations and the work of Mo et al. (2004) and De Propris
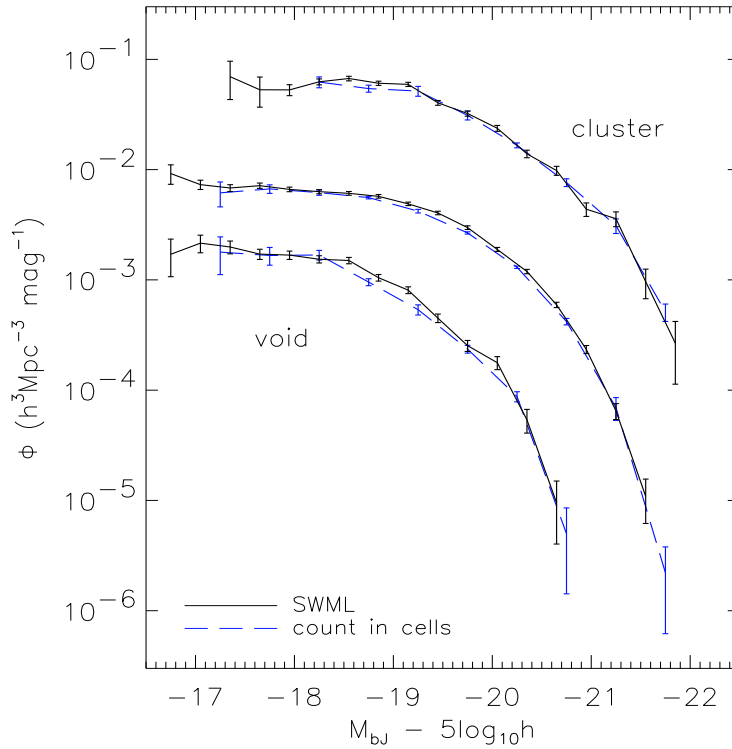
**Figure 5A.1:** A comparison of the raw counts in cells luminosity function with the normalised SWML luminosity function, as described in the text (Section 5.2.3 and Appendix 5A). Shown are the cluster, mean, and void populations consisting of all galaxy types only, although all luminosity functions used in this paper behave equally as well. The shapes estimated by the two very different methods are in very good agreement over the magnitude ranges considered.

et al. (2003) (and references therein). Our primary result is the striking change in population types between voids and clusters shown in Fig. 5.5: faint, late-type galaxies are overwhelmingly the dominant galaxy population in voids, completely the contrary of the situation in clusters. The existence of such a population in the voids, and more generally the way populations of different type are seen to change between different density environments, place important constraints on current and future models of galaxy formation.

## Appendix 5A: The counts-in-cells luminosity function estimator and comparison to the SWML results

Our counts-in-cells (CiC) method to measure the density dependent luminosity function and obtain its amplitude is simple and will be illustrated with the example of a mock

galaxy sample in a cubical volume of side-length *L*. The full luminosity function for such a sample is trivial. By definition it is simply the number of galaxies in each magnitude interval divided by the volume of the box:

$$\Phi(M) = N(M) \,/\, L^3 \;. \tag{5A.1}$$

To determine the luminosity function as a function of local galaxy density we require two additional pieces of information. Firstly we sub-divide the galaxy population into density bins. The local density for each galaxy is calculated within an $8h^{-1}$Mpc radius as described in Section 5.2.2. This gives us the number of galaxies in each density bin belonging to each magnitude range, $N_{\delta_8}(M)$.

Secondly we determine the volume which should be attributed to the various density bins. We do this by finding the fraction of the volume in which the galaxies of each density bin reside, $f_{\delta_8}$. This fraction is measured by massively oversampling the box with *randomly* placed $8h^{-1}$Mpc spheres, in each of which we estimate a local density in the same way as before. Once all spheres have been placed we count the number which have a local density in each density range. The volume fraction of each bin is then just the fraction of spheres found in each bin. Since the total volume of the box is known, the volume of each density bin is now also known. The density dependent luminosity function is then calculated as:

$$\phi_{\delta_8}(M) = N_{\delta_8}(M) \,/\, f_{\delta_8} L^3 \;. \tag{5A.2}$$

The situation becomes more complicated when dealing with a magnitude limited redshift survey instead of a simple simulated box. Galaxy counting and volume estimation must now be restricted to regions of the survey in which the magnitude range being considered is volume limited. This range of course changes for each magnitude bin in which the luminosity function is measured. In addition, small corrections ($<$ 10%) are required when counting galaxies to account for the spectroscopic incompleteness of the survey (see Croton et al. 2004a,b). In all other respects, however, the calculation of $\Phi_{\delta_8}(M)$ is the same as in the "box" example given above.

In Fig. 5A.1 we show a comparison of the 2dFGRS CiC and SWML luminosity functions calculated from the same void, mean, and cluster galaxy samples. The SWML luminosity function has been normalised to the CiC measurement as described in Section 5.2.2. We see that both methods produce almost identical luminosity distribution shapes. This gives us confidence that the CiC luminosity function can be used to normalise the SWML luminosity function in an unbiased way.

Because of the volume-limited restriction of the CiC method, the number of galaxies used to calculate the luminosity function is smaller than for the SWML method, which draws from the larger magnitude-limited catalogue. However the benefit of the CiC method is that it gives a direct measurement of the number density of galaxies rather than just the shape of the distribution as the SWML estimator does. In addition, the CiC method is very easy to apply to mock catalogues, as described above. By combining the CiC and SWML methods we capture the best features of both.
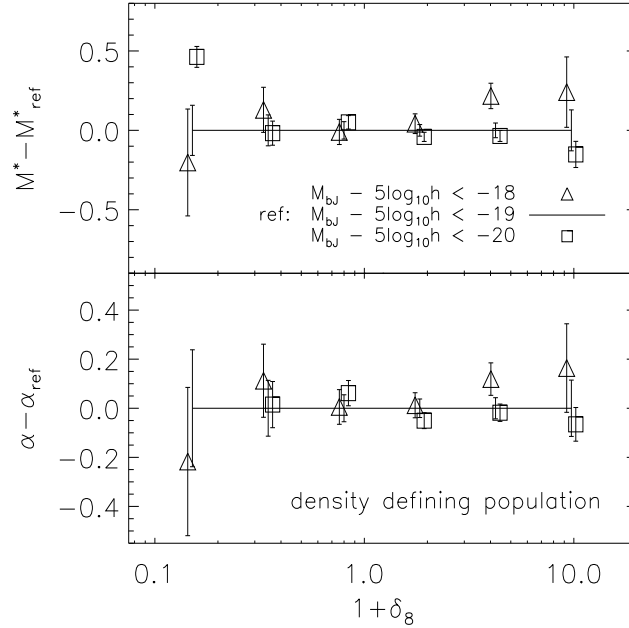
**Figure 5B.1:** The difference in the STY Schechter function parameters when the local density is calculated with an increasingly fainter density defining population (DDP): $M_{min} - 5\log_{10} h = -20, -19$, and $-18$. Such a change also changes the redshift range of the included volume as described in the text. For clarity only results for all galaxy types are shown. The reference sample is the $M_{min} - 5\log_{10} h = -19$ DDP used throughout this paper, and the other DDP results are shown relative to this.

# Appendix 5B: The effects of changing the density defining population and smoothing scale

In our analysis we are required to make two important choices before beginning. The first is to find the widest possible absolute magnitude range for the density defining population (DDP, see Section 5.2.2) while maximising the amount of the 2dFGRS survey volume sampled. The second is the scale over which we smooth the DDP galaxy distribution to determine the density contours within this volume. We will now consider the effect of changing each of these choices in turn.

## The density defining population

The DDP is important in that it not only sets the mean density of galaxies used to define the density contours, but also determines the redshift range of the full magnitude-limited
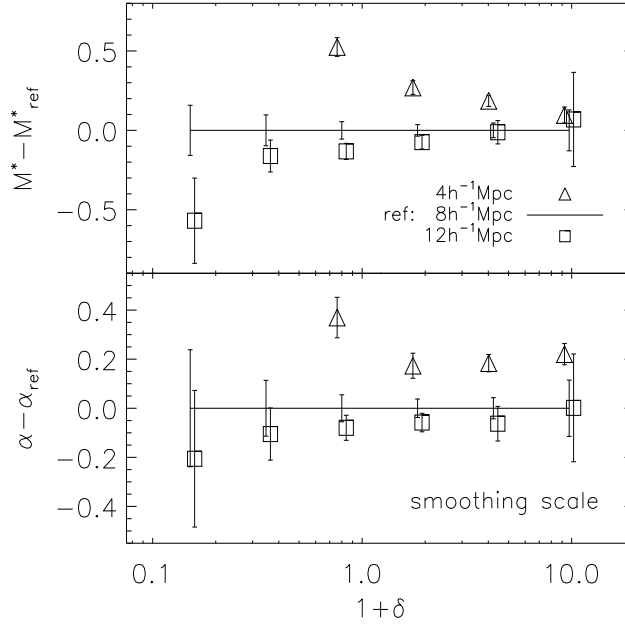
**Figure 5B.2:** The difference in the STY Schechter function parameters for different density bins when calculated by smoothing the local galaxy distribution on different scales: 4, 8, and $12h^{-1}$Mpc. For clarity only results for all galaxy types are shown. The reference sample is the $8h^{-1}$Mpc sphere smoothing scale used throughout this paper, and the other smoothing scale results are shown relative to this.

catalogue to be included in the analysis. Clearly one would like as high-statistics a sample as possible in as large a volume as possible for the best results. In a volume limited galaxy sample such as the DDP, the maximum galaxy redshift available is constrained by the specified faint absolute magnitude limit: galaxies beyond this redshift range are no longer guaranteed to be volume limited and are thus not included. For the DDP faint magnitude limit of $M_{min} - 5\log_{10} h = -19$ the maximum survey boundary is $z = 0.13$. Changing the faint magnitude limit to $M_{min} - 5\log_{10} h = -18$ (20), i.e. a denser (sparser) DDP, results in a maximum redshift boundary of $z = 0.088$ (0.188), i.e. a smaller (larger) sampling volume.

In Fig. 5B.1 we show the result found when repeating the analysis of Section 5.3 (Fig. 5.7) but using DDPs defined by different faint absolute magnitude limits. We plot the STY $M^*$ and $\alpha$ values for each density bin *relative* to the $M_{min} - 5\log_{10} h = -19$ DDP used throughout this paper. The faintest DDP shown, $M_{min} - 5\log_{10} h = -18$, is approximately 8 times denser than the brightest, $M_{min} - 5\log_{10} h = -20$, but with a volume roughly 30 times smaller. Even so, almost all measurements shown across all density bins are consistent at

the $1\sigma$ level, demonstrating that our definition of the DDP is a robust representation of the underlying global density distribution.

## The smoothing scale

Now let us examine how changing the smoothing scale with which we define local density affects the shape of our luminosity functions. In Fig. 5B.2 we examine the values of the Schechter parameters when measured with spheres of radius 4 and $12h^{-1}$Mpc, compared to when the luminosity function is measured with an $8h^{-1}$Mpc sphere.

Fig. 5B.2 shows a typical deviation of $< 0.2$ magnitudes for $M^*$ and $< 0.2$ for $\alpha$. The $4h^{-1}$Mpc smoothing scale deviates strongly from the other values in the under-dense regions (the first two points lie beyond the axis range plotted), however in these environments such a smoothing scale gives a poor estimate of the local galaxy density due to Poisson noise in small number counts. Indeed, Hoyle et al. (2004) have shown that in the extreme under-dense 2dFGRS survey regions the characteristic scale of voids is approximately $15h^{-1}$Mpc. For cluster regions $4h^{-1}$Mpc spheres can be employed and would give a higher resolution discrimination of the structure. The $8h^{-1}$Mpc smoothing scale we have adopted captures the essential aspects of voids while roughly optimising the statistical signal, and is thus a good probe of both the under and over-dense regions of the survey volume.

# Appendix 5C: Systematic effects when estimating the Schechter function parameters

One may ask to what degree the trends seen in Fig. 5.7 and Table 5.1 are influenced by the systematics discussed in Section 5.2.4. We note there that our STY measurements recover a flatter faint end than the current published 2dFGRS luminosity function for the completed catalogue. We identify three systematic effects which contribute to this behaviour: the absolute magnitude range considered when applying the STY estimator, the fact that the luminosity function is not perfectly described by a Schechter function, and the sensitivity of the faint-end slope parameterisation to model-dependent corrections included to account for missed galaxies.

We find that the first two of these effects have the strongest influence on the measured STY faint-end slope. Indeed, testing the first reveals that any STY estimate of the 2dFGRS luminosity function over a restricted absolute magnitude range displays a systematic shift in the recovered STY parameters along a line in the $M^* - \alpha$ plane. The brighter the faint magnitude restriction, the flatter the faint-end slope is and the fainter the characteristic magnitude becomes. Such behaviour is a consequence of small but important deviations in the galaxy luminosity function shape from the pure Schechter function assumed by the STY estimator. In addition, Fig. 11 of Norberg et al. (2002) reveals a dip in the luminosity function between the magnitude range $-17 > M_{b_J} - 5\log_{10}h > -18$ and a steepening faintward of this. In our analysis only galaxies brighter than $M_{b_J} - 5\log_{10}h =$
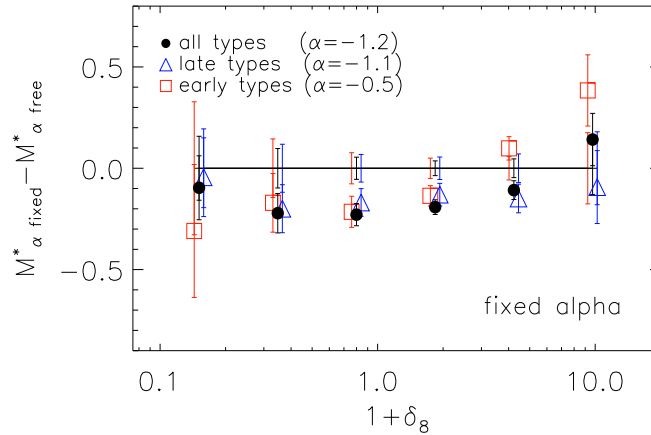
**Figure 5C.1:** The shift in the STY Schechter function parameter $M^*$ when $\alpha$ is kept fixed at the published field value, compared with that found when $\alpha$ remains free (Table 5.1 and Fig. 5.7). The points are plotted as a function of local density and shown for each galaxy type and the combined all-type sample.

$-17$ are considered due to the restriction of the DDP. This limitation adds extra weight to the influence of the dip on the STY fit contributing further to a flatter estimation of $\alpha$. When mock galaxy catalogues constructed to have a perfect Schechter function luminosity distribution are analysed in an identical way to the 2dFGRS samples, we find that the above systematics all but disappear and the "true" $M^*$ and $\alpha$ values are recovered for any reasonable choice of STY fitting range.

Finally, we note that the sensitivity of the faint-end slope parametrisation to systematic corrections for spectroscopically missed galaxies is minimised by restricting our analysis to galaxies with $b_J < 19$, for which the spectroscopic incompleteness is typically less than $\sim 8\%$ (see Fig. 16 of Colless et al. 2001).

Given that a full correction of the above systematic effects is not possible in our analysis, the next best thing we can do is try to quantify to what degree they influence our results and conclusions. We do this by fixing the faint-end slope $\alpha$ when applying the STY estimator: at $-1.2$ for the all-types samples, $-1.1$ for the late-type samples, and at $-0.5$ for the early-type samples. Such choices enforce the published field luminosity function faint end values found by Norberg et al. (2002b) and Madgwick et al. (2002) and remove the degeneracy in the $M^* - \alpha$ plane.

Fig. 5C.1 shows the size of the shift in $M^*$ when such constraints are applied relative to that found when $\alpha$ is allowed to remain free (i.e. Table 5.1 and Fig. 5.7). Most notable here is that, apart from the two most over-dense bins in the early-type sample, there is no significant difference in the *behaviour* of $M^*$ with density environment. The approximate 0.2 magnitude offset seen in this figure can be understood by remembering that because the faint-end slope we measure when $\alpha$ remains free is slightly flatter than the published

values (due to the systematics discussed above), by artifically fixing $\alpha$ one forces $M^*$ to move to compensate. The important point is that the *trends* seen in Fig. 5.7 with changing local density remain unchanged.

For the two most over-dense early-type samples a shift of up to 0.4 magnitudes is seen. We note from Table 5.1 that our best-fit (free $\alpha$) early-type cluster value of $\alpha = -1.12\pm0.14$ is well matched by the equivalent 2dFGRS De Propris et al. (2003) result of $-1.05 \pm 0.04$. In effect, by constraining the early-type cluster faint-end slope to the field value of $-0.5$ we ignore the real changes in galaxy population seen between the Madgwick et al. (their Fig. 10) and De Propris et al. (their Fig. 3) luminosity functions (see also our Fig. 5.2). Such population changes, we argue, result in the strikingly different Schechter function parameterisation behaviour seen in Fig. 5.7 and Table 5.1 for early and late-type galaxies. Fig. 5C.1 gives us confidence that the $M^* - \alpha$ degeneracies and systematics investigated here are not significantly influencing our results or the conclusions we draw from them.

# 6 The many lives of AGN: cooling fbws, black holes and the luminosities and colours of galaxies[1]

## Abstract

We simulate the growth of galaxies and their central supermassive black holes throughout a representative region of the universe by implementing a suite of semi-analytic models on the output of the Millennium Run, a very large simulation of the concordance $\Lambda$CDM cosmogony. Our procedures follow the detailed assembly history of each object and are able to track the evolution of all objects more massive than the Small Magellanic Cloud throughout a volume comparable to that of large modern redshift surveys. In this first paper we supplement previous treatments of the growth and activity of central black holes with a new model for 'radio' feedback from those AGN that lie at the centre of a quasistatic X-ray emitting atmosphere in a galaxy group or cluster. We show that for energetically and observationally plausible parameters such a model can simultaneously explain: (i) the low observed mass drop-out rate in cooling flows; (ii) the exponential cut-off at the bright end of the galaxy luminosity function; and (iii) the fact that the most massive galaxies tend to be bulge-dominated systems in clusters and to contain systematically older stars than lower mass galaxies. This success occurs because static hot atmospheres form only in the most massive structures, and radio feedback (in contrast, for example, to supernova or starburst feedback) can suppress further cooling and star formation without itself requiring star formation. We discuss possible physical models which might explain the accretion rate scalings required for our phenomenological 'radio mode' model to be successful.

## 6.1 Introduction

The remarkable agreement between recent measurements of cosmic structure over a wide range of length- and time-scales has established a standard paradigm for structure formation, the $\Lambda$CDM cosmogony. This model can simultaneously match the microwave background fluctuations seen at $z \sim 1000$ (e.g. Spergel et al. 2003), the power spectrum of the low redshift galaxy distribution (e.g. Percival et al. 2002; Tegmark et al. 2004),

---

[1]**D.J. Croton**, V. Springel, S.D.M. White, G. De Lucia, C.S. Frenk, L. Gao, A.R. Jenkins, G. Kauffmann, J.F. Navarro, N. Yoshida, MNRAS, submitted, 2005

the nonlinear mass distribution at low redshift as characterised by cosmic shear (e.g. Van Waerbeke et al. 2002) and the structure seen in the $z = 3$ Ly $\alpha$ forest (e.g. Mandelbaum et al. 2003). It also reproduces the present acceleration of the cosmic expansion inferred from supernova observations (Perlmutter et al. 1999; Riess et al. 1998), and it is consistent with the mass budget inferred for the present universe from the dynamics of large-scale structure (Peacock et al. 2001), the baryon fraction in rich clusters (White et al. 1993) and the theory of Big Bang nucleosynthesis (Olive et al. 2000). A working model for the growth of all structure thus appears well established.

In this cosmogony, galaxies form when gas condenses at the centres of a hierarchically merging population of dark haloes, as originally proposed by White & Rees (1978). Attempts to understand this process in detail have consistently run into problems stemming from a mismatch in shape between the predicted distribution of dark halo masses and the observed distribution of galaxy luminosities. Most stars are in galaxies of Milky Way brightness; the galaxy abundance declines exponentially at brighter luminosities and increases sufficiently slowly at fainter luminosities that relatively few stars are in dwarfs. In contrast, the theory predicts a much broader halo mass distribution – a constant mass-to-light ratio would produce more high and low luminosity galaxies than are observed while underpredicting the number of galaxies like the Milky Way. Attempts to solve these problems initially invoked cooling inefficiencies to reduce gas condensation in massive systems, and supernova feedback to reduce star formation efficiency in low mass systems (White & Rees 1978; White & Frenk 1991). Formation of dwarfs may also be suppressed by photoionisation heating (Efstathiou 1992). As Thoul & Weinberg (1995) emphasised, cooling effects alone are too weak to produce the bright end cut-off of the luminosity function, and recent attempts to fit observed luminosity functions have been forced to include additional feedback processes in massive systems (e.g. Benson et al. 2003). In this paper we argue that radio sources may provide the required feedback while at the same time providing a solution to two other long-standing puzzles.

An important unanswered question is why the gas at the centre of most galaxy clusters is apparently not condensing and turning into stars when the observed X-ray emission implies a cooling time which is much shorter than the age of the system. This cooling flow puzzle was noted as soon as the first X-ray maps of clusters became available (Cowie & Binney 1977; Fabian & Nulsen 1977) and it was made more acute when X-ray spectroscopy demonstrated that very little gas is cooling through temperatures even a factor of three below that of the bulk of the gas (Peterson et al. 2001; Tamura et al. 2001). A clue to the solution may come from the observation (Burns et al. 1981) that every cluster with a strong cooling flow also contains a massive and active central radio galaxy. Tabor & Binney (1993) suggested that radio galaxies might regulate cooling flows, and this idea has gained considerable recent support from X-ray maps which show direct evidence for an interaction between radio lobes and the intracluster gas (Fabian et al. 2003; McNamara et al. 2000, 2005). A number of authors have suggested ways in which the radio source might replace the thermal energy lost to X-ray emission (Binney & Tabor 1995; Churazov et al. 2002; Brüggen & Kaiser 2002; Ruszkowski & Begelman 2002; Kaiser & Binney 2003; Omma et al. 2004). We do not focus on this aspect of the problem here, but rather

demonstrate that if the scaling properties of radio source feedback are set so they can plausibly solve the cooling flow problem they induce a cut-off at the bright end of the galaxy luminosity function which agrees well with observation.

Another puzzling aspect of the galaxy population is the fact that the most massive galaxies, typically ellipticals in clusters, are made of the oldest stars and so finished their star formation earlier than lower mass galaxies (Kauffmann et al. 2003; Heavens et al. 2004). Confirming evidence for this comes from look-back studies which show that both star-formation and AGN activity take place more vigorously and in higher mass objects at redshifts of 1 to 2 than in the present Universe (e.g. Shaver et al. 1996; Madau et al. 1996). Cowie et al. (1996) termed this phenomenon 'down-sizing', and *prima facie* it conflicts with hierarchical growth of structure in a ΛCDM cosmogony where massive dark haloes assemble at lower redshift than lower mass haloes (e.g. Lacey & Cole 1993). This puzzle is related to the previous two; the late-forming high mass haloes in ΛCDM correspond to groups and clusters of galaxies, and simple theories predict that at late times their central galaxies should grow to masses larger than those observed through accretion from cooling flows. In the model we present below, radio galaxies prevent significant accretion, thus limiting the mass of the central galaxies and preventing them from forming stars at late times when their mass and morphology can still change through mergers. The result is a galaxy luminosity function with a sharper high-mass cut-off in which the most massive systems are red, dead and elliptical.

To make quantitative predictions for the galaxy population in a ΛCDM universe it is necessary to carry out simulations. Present numerical capabilities allow reliable simulation of the coupled nonlinear evolution of dark matter and diffuse gas, at least on the scales which determine the global properties of galaxies. Once gas cools and condenses into halo cores, however, both its structure and the rates at which it turns into stars and feeds black holes are determined by small-scale 'interstellar medium' processes which are not resolved. These are usually treated through semi-analytic recipes, parameterised formulae which encapsulate 'subgrid' physics in terms of star formation thresholds, Schmidt 'laws' for star formation, Bondi models for black hole feeding, etc. The form and the parameters of these recipes are chosen to reproduce the observed systematics of star formation and AGN activity in galaxies (e.g. Kennicutt 1998). With a well-constructed scheme it is possible to produce stable and numerically converged simulations which mimic real star-forming galaxies remarkably well (Springel & Hernquist 2003a). In strongly star-forming galaxies, massive stars and supernovae produce winds which redistribute energy, mass and heavy elements over large regions (Heckman et al. 1990; Martin 1999). Even stronger feedback is possible, in principle, from AGN (Begelman et al. 1991). In both cases the determining processes occur on very small scales and so have to be included in simulations through parametrised semi-analytic models. Unfortunately, the properties of simulated galaxies turn out to depend strongly on how these unresolved star-formation and feedback processes are treated (Di Matteo et al. 2005).

Since the diffuse gas distribution and its cooling onto galaxies are strongly affected by the description adopted for the subgrid physics, every modification of a semi-analytic model (or of its parameters) requires a simulation to be repeated. This makes parameter studies or

tests of, say, the effects of different AGN feedback models into a very expensive computing exercise. A cost-effective alternative is to represent the behaviour of the diffuse gas also by a semi-analytic recipe. Since the dark matter couples to the baryons only through gravity, its distribution on scales of galaxy haloes and above is only weakly affected by the details of galaxy formation. Its evolution can therefore be simulated once, and the evolution of the baryonic component can be included in post-processing by applying semi-analytic models to the stored histories of all dark matter objects. Since the second step is computationally cheap, available resources can be used to carry out the best possible dark matter simulation, and then many parameter studies or tests of alternative models for, say, starburst winds or radio galaxy feedback can be carried out in post-processing. This simulation approach was first introduced by Kauffmann et al. (1999) and it is the approach we apply here to the Millennium Run, the largest calculation to date of the evolution of structure in the concordance ΛCDM cosmogony (Springel et al. 2005).

This paper is organised as follows. In Section 6.2 we describe the Millennium Run and the post-processing we carried out to construct merging history trees for all the dark haloes within it. Section 6.3 presents the model for the formation and evolution of galaxies and their central supermassive black holes that we implement on these merging trees. Section 6.4 describes the main results of our modelling, concentrating on the influence of 'radio mode' feedback on the properties of the massive galaxy population. In Section 6.5 we discuss physical models for black hole accretion which may explain the phenomenology required for our model to be successful. Finally, Section 6.6 summarises our conclusions and suggests some possible directions for future investigation.

## 6.2 The dark matter skeleton: the Millennium Run

Our model for the formation and evolution of galaxies and their central supermassive black holes is implemented on top of the Millennium Run, a very large dark matter simulation of the concordance ΛCDM cosmology with $2160^3 \simeq 1.0078 \times 10^{10}$ particles in a periodic box of $500\,h^{-3}\mathrm{Mpc}^3$. A full description is given in Springel et al. (2005): here we summarise the main simulation characteristics and the definition and construction of the dark matter merging history trees we use in our galaxy formation modelling. The dark matter distribution is illustrated in the top panel of Fig. 6.1 for a $330 \times 280 \times 15\,h^{-1}\mathrm{Mpc}$ slice cut from the full volume. The projection is colour coded by density and local velocity dispersion, and illustrates the richness of dark matter structure for comparison with structure in the light distribution to which we will come later. Dark matter plots on a wider range of scales may be found in Springel et al. (2005).

### 6.2.1 Simulation characteristics

We adopt cosmological parameter values consistent with a combined analysis of the 2dF-GRS (Colless et al. 2001) and first-year WMAP data (Spergel et al. 2003; Seljak et al. 2004). They are $\Omega_m = \Omega_{dm} + \Omega_b = 0.25$, $\Omega_b = 0.045$, $h = 0.73$, $\Omega_\Lambda = 0.75$, $n = 1$,

and $\sigma_8 = 0.9$. Here $\Omega_m$ denotes the total matter density in units of the critical density for closure, $\rho_{crit} = 3H_0^2/(8\pi G)$. Similarly, $\Omega_b$ and $\Omega_\Lambda$ denote the densities of baryons and dark energy at the present day. The Hubble constant is given as $H_0 = 100\,h\,\mathrm{km\,s^{-1}\,Mpc^{-1}}$, while $\sigma_8$ is the *rms* linear mass fluctuation within a sphere of radius $8\,h^{-1}\mathrm{Mpc}$ extrapolated to $z = 0$.

The chosen simulation volume is a periodic box of size $500\,h^{-1}\mathrm{Mpc}$, which implies a particle mass of $8.6 \times 10^8\,h^{-1}\mathrm{M}_\odot$. This volume is large enough to include interesting objects of low space density, such as quasars or rich galaxy clusters, the largest of which contain about 3 million simulation particles at $z = 0$. At the same time, the mass resolution is sufficient that haloes that host galaxies as faint as $0.1\,L_\star$ are typically resolved with at least $\sim 100$ particles.

The initial conditions at $z = 127$ were created by displacing particles from a homogeneous, 'glass-like' distribution (White 1996) using a Gaussian random field with a $\Lambda$CDM linear power spectrum as given by the Boltzmann code CMBFAST (Seljak & Zaldarriaga 1996). The simulation was then evolved to the present epoch using a leapfrog integration scheme with individual and adaptive time steps, with up to 11 000 time steps for individual particles.

The simulation itself was carried out with a special version of the GADGET-2 code (Springel et al. 2001b; Springel 2005) optimised for very low memory consumption so that it would fit into the nearly 1 TB of physically distributed memory available on the parallel IBM p690 computer[2] used for the calculation. The computational algorithm used the 'TreePM' method (Xu 1995; Bode et al. 2000; Bagla 2002) to evaluate gravitational forces, combining a hierarchical multipole expansion, or 'tree' algorithm (Barnes & Hut 1986), and a classical, Fourier transform particle-mesh method (Hockney & Eastwood 1981). An explicit force-split in Fourier-space produces a very nearly isotropic force law with negligible force errors at the force matching scale. The short-range gravitational force law is softened on comoving scale $5\,h^{-1}\mathrm{kpc}$ (Plummer-equivalent) which may be taken as the spatial resolution limit of the calculation, thus achieving a dynamic range of $10^5$ in 3D. The calculation, performed in parallel on 512 processors, required slightly less than 350 000 processor hours of CPU time, or 28 days of wall-clock time.

## 6.2.2 Haloes, substructure, and merger tree construction

Our primary application of the Millennium Run in this paper uses finely resolved hierarchical merging trees which encode the full formation history of tens of millions of haloes and the subhaloes that survive within them. These merging history trees are the backbone of the galaxy formation model that we implement in post-processing in order to study the wide range of baryonic processes that are important during the formation and evolution of galaxies and their central supermassive black holes.

We store the full particle data at 64 output times, spaced approximately logarithmically in expansion factor between $z = 20$ and $z = 0$. The logarithmic spacing is, however, made

---

[2]This computer is operated by the Computing Centre of the Max-Planck Society in Garching, Germany.
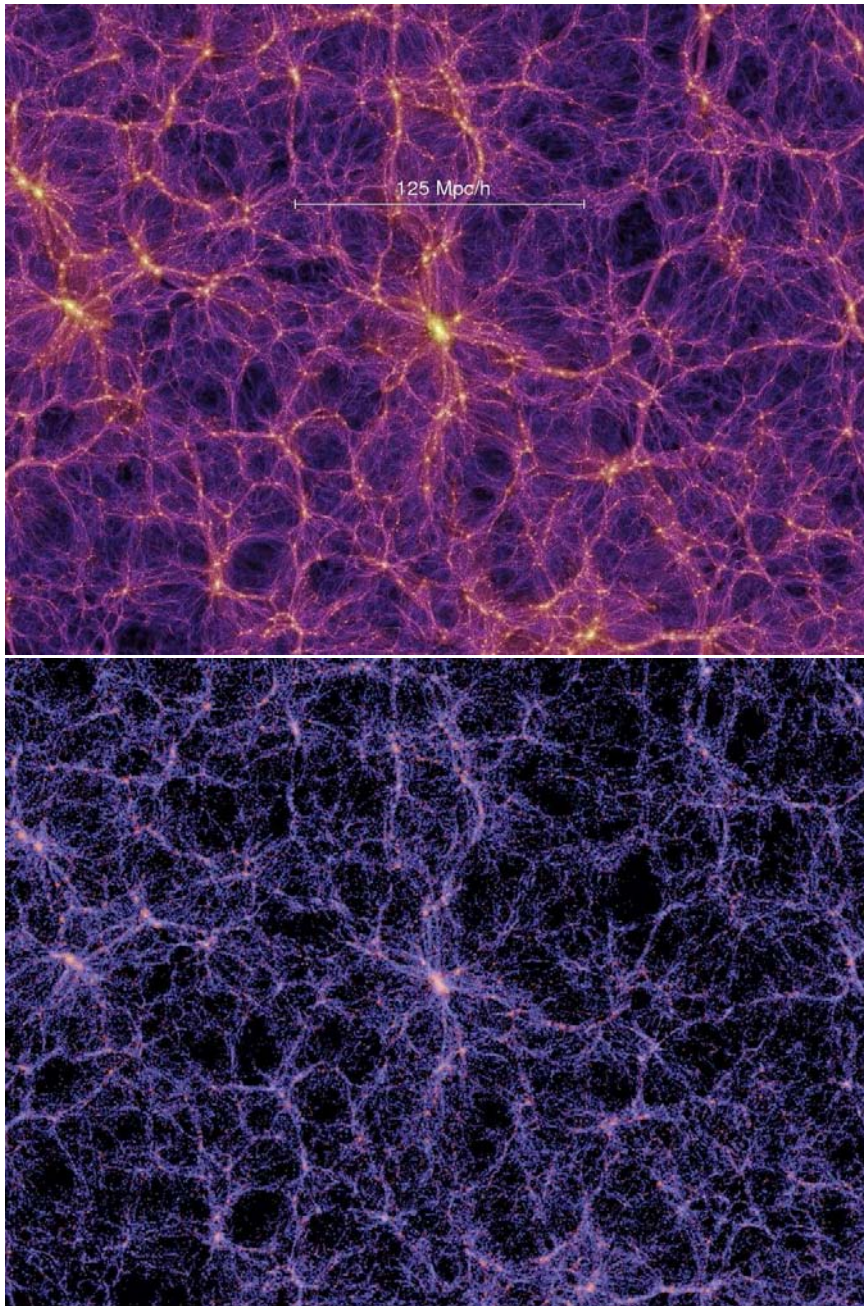
**Figure 6.1:** The redshift zero distribution of dark matter (top) and of galaxy light (bottom) for a slice of thickness $15\,h^{-1}$Mpc, cut from the Millennium Run. For the dark matter distribution, intensity encodes surface density and colour encodes local velocity dispersion. For the light distribution, intensity encodes surface brightness and colour encodes mean B−V colour. The linear scale is shown by the bar in the top panel.

progressively finer towards lower redshift. We note that each snapshot has a total size in excess of 300 GB, giving a raw data volume of nearly 20 TB.

Together with each particle coordinate dump, the simulation code directly produces a friends-of-friends (FOF) group catalogue on the fly and in parallel. FOF groups are defined as equivalence classes where any pair of two particles is placed into the same group if their mutual separation is less than 0.2 of the mean particle separation (Davis et al. 1985). This criterion combines particles into groups with a mean overdensity of about 200, corresponding approximately to that expected for a virialised group. The group catalogue saved to disk for each output only kept groups with at least 20 particles.

High-resolution simulations like the present one exhibit a rich substructure of gravitationally bound dark matter subhaloes orbiting within larger virialised structures (e.g. Ghigna et al. 1998). The FOF group-finder built into our simulation code identifies the haloes but not their substructure. Since we wish to follow the fate of infalling haloes and galaxies, which are typically identifiable for a substantial time as a dark matter substructure within a FOF halo, we apply in post-processing an improved and extended version of the SUBFIND algorithm of Springel et al. (2001a). This computes an adaptively smoothed dark matter density field within each halo using a kernel-interpolation technique, and then exploits the topological connectivity of excursion sets above a density threshold to identify substructure candidates. Each substructure candidate is subjected to a gravitational unbinding procedure. If the remaining bound part has more than 20 particles, the subhalo is kept for further analysis and some of its basic physical properties are determined (angular momentum, maximum of its rotation curve, velocity dispersion, etc.). After all subhaloes are identified they are extracted from the FOF halo so that the remaining featureless 'background' halo can also be subjected to the unbinding procedure. We also compute a virial mass estimate for each FOF halo using the spherical-overdensity approach, where the centre is determined using the minimum of the gravitational potential within the group and we define the boundary at the radius which encloses a mean overdensity of 200 times the critical value. The virial mass, radius and circular velocity of a halo at redshift $z$ are then related by

$$M_{\mathrm{vir}} \;=\; \frac{100}{\mathrm{G}}\, H_0^2(z)\, R_{\mathrm{vir}}^3 \;=\; \frac{V_{\mathrm{vir}}^3}{10\,\mathrm{G}\,H_0(z)} \tag{6.1}$$

where $H_0(z)$ is the Hubble constant at redshift $z$.

At $z = 0$ our procedures identify $17.7 \times 10^6$ FOF groups, down from a maximum of $19.8 \times 10^6$ at $z = 1.4$ when groups were more abundant but lower mass on average. The $z = 0$ groups contain a total of $18.2 \times 10^6$ subhaloes, with the largest FOF group containing 2328 of them. (Note that with our definitions, all FOF groups contain at least one subhalo, the *main* subhalo which is left over after removal of any substructure and the unbound component.)

Having found all haloes and subhaloes at all output snapshots, we then characterise structural evolution by building merging trees that describe in detail how haloes grow as the universe evolves. Because structures merge hierarchically in CDM universes there can be several progenitors for any given halo, but in general there is only one descendant. (Typ-

ically the cores of virialised dark matter structures do not split into two or more objects.) We therefore construct merger trees based on defining a unique descendant for each halo and subhalo. This is, in fact, sufficient to define the entire merger tree, since the progenitor information then follows implicitly. Further details can be found in Springel et al. (2005).

We store the resulting merging histories tree by tree. Since each tree contains the full formation history of some $z=0$ halo, the physical model for galaxy formation can be computed sequentially tree by tree. It is thus unnecessary to load all the history information on the simulation into computer memory at the same time. Actually, this would be currently impossible, since the trees contain a total of around 800 million subhaloes for each of which a number of attributes are stored.

## 6.3 Building galaxies: the semi-analytic model

### 6.3.1 Overview

In the following sub-sections we describe the baryonic physics of one particular model for the formation and evolution of galaxies and of their central supermassive black holes. A major advantage of our simulation strategy is that the effects of parameter variations within this model (or indeed alternative assumptions for some of the processes) can be explored at relatively little computational expense since the model operates on the stored database of merger trees; the simulation itself and the earlier stages of post-processing do not need to be repeated. We have, in fact, explored a wide model and parameter space to identify our current best model. We summarise the main parameters of this model, their 'best' values, and their plausible ranges in Table 6.1. These choices produce a galaxy population which matches quite closely many observed quantities. In this paper we discuss the field galaxy luminosity-colour distribution; the mean stellar mass – stellar age relation; the Tully-Fisher relation, cold gas fractions and gas-phase metallicities of Sb/c spirals; the colour – magnitude relation of ellipticals; the bulge mass – black hole mass relation; and the volume-averaged cosmic star-formation and black hole accretion histories. In Springel et al. (2005) we also presented results for galaxy correlations as a function of absolute magnitude and colour, for the baryonic 'wiggles' in the large-scale power spectrum of galaxies, and for the abundance, origin and fate of high redshift supermassive black holes which might correspond to the $z \sim 6$ quasars discovered by the SDSS (Fan et al. 2001)

In our model we aim to motivate each aspect of the physics of galaxy formation using the best available observations and simulations. Our parameters have been chosen to reproduce local galaxy properties and are stable in the sense that none of our results is critically dependent on any single parameter choice; plausible changes in one parameter or recipe can usually be accommodated through adjustment of the remaining parameters within their own plausible range. The particular model we present is thus not unique. Importantly, our model for radio galaxy heating in cooling flows, which is the main focus of this paper, is only weakly influenced by the remaining galaxy formation and black hole growth physics. As a consequence, most of our inferences about the effect of such feedback on the galaxy population do not depend strongly on the broader model and its uncertainties.

The distribution of galaxy light in our 'best' model is shown in the bottom panel of Fig. 6.1 for comparison with the mass distribution in the top panel. For both the volume is a projected $330 \times 280 \times 15 \, h^{-1}$Mpc slice cut from the full $0.125 \, h^{-3}$Gpc$^3$ simulation box. The plot of surface brightness is colour-coded by the luminosity-weighted mean $B-V$ colour of the galaxies. On large scales light clearly follows mass, but non-trivial biases become evident on smaller scales, especially in 'void' regions. The redder colour of galaxies in high density regions is also very clear.

## 6.3.2 Gas infall and cooling

We follow the standard paradigm set out by White & Frenk (1991) as adapted for implementation on high resolution N-body simulations by Springel et al. (2001a) and De Lucia et al. (2004). This assumes that as each dark matter halo collapses, its own 'fair share' of cosmic baryons collapse with it (but see Section 6.3.3 below). Thus in our model the mass fraction in baryons associated with every halo is taken to be $f_b = 17\%$, consistent with the first-year WMAP result (Spergel et al. 2003). Initially these baryons are in the form of diffuse gas with primordial composition, but later they include gas in several phases as well as stars and heavy elements. The fate of the infalling gas depends on redshift and on the depth of the halo potential (Silk 1977; Rees & Ostriker 1977; Binney 1977; White & Rees 1978). At late times and in massive systems the gas shocks to the virial temperature and is added to a quasi-static hot atmosphere that extends approximately to the virial radius of the dark halo. Gas from the central region of this atmosphere may accrete onto a central object through a cooling flow. At early times and in lower mass systems the infalling gas still shocks to the virial temperature but its post-shock cooling time is sufficiently short that a quasi-static atmosphere cannot form. Rather the shock occurs at much smaller radius and the shocked gas cools rapidly and settles onto a central object, which we assume to be a cold gas disk. This may in turn be subject to gravitational instability, leading to episodes of star formation.

More specifically, the cooling time of a gas is conventionally taken as the ratio of its specific thermal energy to the cooling rate per unit volume,

$$t_{\text{cool}} = \frac{3}{2} \frac{\bar{\mu} m_p kT}{\rho_g(r) \Lambda(T, Z)} \, . \tag{6.2}$$

Here $\bar{\mu} m_p$ is the mean particle mass, $k$ is the Boltzmann constant, $\rho_g(r)$ is the hot gas density, and $\Lambda(T, Z)$ is the cooling function. The latter depends both on the metallicity $Z$ and the temperature of the gas. In our models we assume the post-shock temperature of the infalling gas to be the virial temperature of the halo, $T = 35.9(V_{\text{vir}}/\text{km s}^{-1})^2$K. When needed, we assume that the hot gas within a static atmosphere has a simple 'isothermal' distribution,

$$\rho_g(r) = \frac{m_{\text{hot}}}{4\pi R_{\text{vir}} r^2} \, , \tag{6.3}$$

where $m_{\text{hot}}$ is the total hot gas mass associated with the halo and is assumed to extend to its virial radius $R_{\text{vir}}$.

**Table 6.1:** A summary of our main model parameters and their best values and plausible ranges, as described in the text. Once set, these values are kept fixed for all results presented in this paper, in particular for models in which AGN feedback is switched off.

| parameter | description | best value | plausible range |
|:---:|:---|:---:|:---:|
| $f_b$ | cosmic baryon fraction (§6.3.3) | 0.17 | fixed |
| $z_0, z_r$ | redshift of reionization (§6.3.3) | 8, 7 | fixed |
| $f_{BH}$ | merger cold gas BH accretion fraction (§6.3.4) | 0.03 | $0.02 - 0.04$ |
| $\kappa_{AGN}$ | quiescent hot gas BH accretion rate ($M_\odot yr^{-1}$) (§6.3.4) | $6 \times 10^{-6}$ | $(4 - 8) \times 10^{-6}$ |
| $\alpha_{SF}$ | star formation efficiency (§6.3.5) | 0.07 | $0.05 - 0.15$ |
| $\epsilon_{disk}$ | SN feedback disk reheating efficiency (§6.3.6) | 3.5 | $1 - 5$ |
| $\epsilon_{halo}$ | SN feedback halo ejection efficiency (§6.3.6) | 0.35 | $0.1 - 0.5$ |
| $\gamma_{ej}$ | ejected gas reincorporation efficiency (§6.3.6) | 0.5 | $0.1 - 1.0$ |
| $T_{merger}$ | major merger mass ratio threshold (§6.3.7) | 0.3 | $0.2 - 0.4$ |
| $R$ | instantaneous recycled fraction of SF to the cold disk (§6.3.9) | 0.3 | $0.2 - 0.4$ |
| $Y$ | yield of metals produced per unit SF (§6.3.9) | 0.03 | $0.02 - 0.04$ |

To estimate an instantaneous cooling rate onto the central object of a halo, given its current hot gas content, we define the cooling radius, $r_{\text{cool}}$, as the radius at which the local cooling time (assuming the structure of Eq. 6.3) is equal to the age of the system. As there exists no unique definition for the age of a halo, White & Frenk (1991) proposed to approximate this time by the Hubble time, $t_{\text{H}}$, which is expected to be correct to within a factor of a few. Such a definition, however, neglects the fact that halos grow violently and are unlikely to be in equilibrium for their entire history. To account for this, some authors have instead taken the the cooling time to be the current *equilibrium* age of the system. Somerville & Primack (1999) approximated the equilibrium age of each halo by the time since it last had a major merger. Here we follow Springel et al. (2001a) and Yoshida et al. (2002) and instead approximate $t_{\text{cool}}$ by the halo dynamical time, $R_{\text{vir}}/V_{\text{vir}} \propto t_{\text{H}}$, which represents the mean time scale over which the hot gas has been able to cool quasi-statically. Note that this definition differs from the one originally given by White & Frenk (1991) by a factor of $\sim 10$, resulting in an enhancement to the cooling rate (below) by a factor of $\sim 3$. Unfortunately, the significant uncertainties in the numerical coefficients of the cooling model, combined with the simplifying assumptions about infall geometry, make the cooling rate uncertain to at least this order anyway. Interestingly, our model appears to favour a higher cooling rate, especially at earlier times, which we find is needed to adequately reproduce the red sequence luminosity function (Section 6.4.2).

Using the above definition, a cooling rate can now be determined through a simple continuity equation,

$$\dot{m}_{\text{cool}} = 4\pi\rho_g(r_{\text{cool}})r_{\text{cool}}^2 \dot{r}_{\text{cool}} . \tag{6.4}$$

Despite its simplicity, this equation is a good approximation to the rate at which gas is deposited at the centre in the Bertschinger (1989) similarity solution for a cooling flow. Putting it all together we take the cooling rate within a halo containing a hot gas atmosphere to be

$$\dot{m}_{\text{cool}} = 0.5\, m_{\text{hot}} \frac{r_{\text{cool}} V_{\text{vir}}}{R_{\text{vir}}^2} . \tag{6.5}$$

We assume this equation to be valid when $r_{\text{cool}} < R_{\text{vir}}$. This is the criterion which White & Frenk (1991) proposed to separate the *static hot halo regime* from the *rapid cooling regime*. It was checked quantitatively by the detailed high resolution spherical infall calculations of Forcada-Miró & White (1997).

In low mass haloes or at high redshifts the formal cooling radius lies outside the virial radius $r_{\text{cool}} > R_{\text{vir}}$. The post-shock gas then cools in less than one sound crossing time and cannot maintain the pressure needed to support an accretion shock at large radius. The infall models of Forcada-Miró & White (1997) show that in this situation the accretion shock moves inwards, the post-shock temperature *increases* and the mass stored in the post-shock hot atmosphere *decreases*, because the post-shock gas rapidly cools onto the central object. In effect, all infalling material is accreted immediately onto the central disk. In this *rapid cooling regime* we therefore set the cooling rate onto the central object to be equal to the rate at which new diffuse gas is added to the halo.
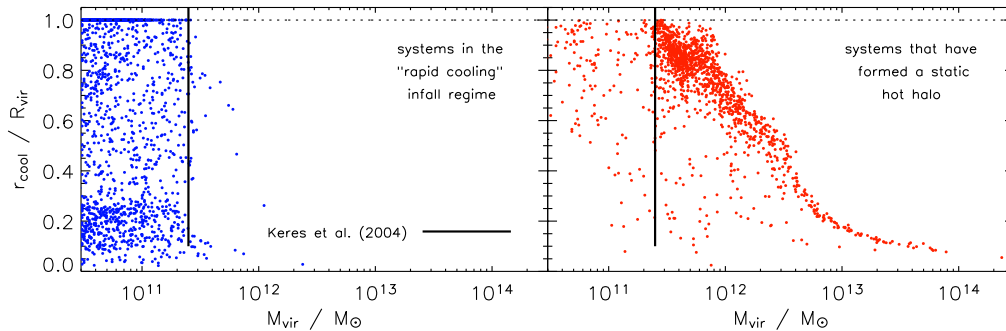
**Figure 6.2:** The ratio of the cooling radius to virial radius for each virialised system at
$z = 0$ plotted against its dark matter virial mass. Systems identified to be
in the 'rapid cooling' regime are shown in the left panel, while those that
have formed a static hot halo are shown on the right (Section 6.3.2). A sharp
transition between the two regimes is seen close to that found by Keres et al.
(2004), marked by the solid vertical line.

### Rapid cooling or cold accretion?

Although much simplified, the above model was shown by Yoshida et al. (2002) and Helly
et al. (2003) to give reasonably accurate, object-by-object predictions for the cooling and
accumulation of gas within the galaxies that formed in their *N*-body+SPH simulations.
These neglected star-formation and feedback effects in order to test the cooling model
alone. In Fig. 6.2 we show the ratio $r_{\rm cool}/R_{\rm vir}$ as a function of virial mass for haloes
in the 'rapid cooling' regime (left panel) and in the 'static halo' regime (right panel) at
$z = 0$ for our 'best' galaxy formation model. The two regimes are distinguished by the
dominant gas component in each halo: when the mass of hot halo gas exceeds that of cold
disk gas, we say the galaxy has formed a static halo, otherwise the system is taken to be
in the rapid cooling phase. Many haloes classified as 'rapidly cooling' by this criterion
have $r_{\rm cool} < R_{\rm vir}$, which would apparently indicate a static hot halo. This is misleading,
however, as systems where cooling is rapid deposit infalling gas onto the central galactic
disk on a short timescale until they have a low-mass residual halo which satisfies $r_{\rm cool} \sim$
$R_{\rm vir}$. This then persists until the next infall event. Averaging over several cycles of this
behaviour, one finds that the bulk of the infalling gas cools rapidly. This is why we choose
to classify systems by their dominant gas component. Note also that a massive hot halo
forms immediately once cooling becomes inefficient, just as in the 1-D infall simulations
of Forcada-Miró & White (1997) and Birnboim & Dekel (2003). Our classification is thus
quite robust.

   The transition between the 'rapid cooling' and 'static halo' regimes is remarkably well
defined. At $z = 0$ it occurs at a halo virial mass of $2$–$3 \times 10^{11} M_\odot$. This is close to the
transition mass found for the same cosmology by Birnboim & Dekel (2003) using spheri-

cally symmetric simulations, and by Keres et al. (2004) using fully 3-D simulations. Both these sets of authors refer to the 'rapid cooling' regime as the 'cold infall'. This is, in fact, a misnomer. In this mode the accretion shock occurs closer to the central object, and so deeper in its potential well than when there is a static hot halo. As a result, the pre-shock velocity of infalling gas is greater in the rapid cooling case, resulting in a *larger* post-shock temperature. The two modes do not differ greatly in the temperature to which infalling gas is shocked, but rather in how long (compared to the system crossing time) the gas spends at the post-shock temperature before its infall energy is lost to radiation. Finally, we note that the existence and importance of these two modes was the major insight of the original work of Silk (1977), Binney (1977) and Rees & Ostriker (1977) and has been built into all modern theories for galaxy formation. A detailed discussion can be found, for example, in White & Frenk (1991).

### 6.3.3 Reionization

Accretion and cooling in low mass haloes is required to be inefficient to explain why dwarf galaxies contain a relatively small fraction of all condensed baryons (White & Rees 1978). This inefficiency may in part result from photoionisation heating of the intergalactic medium (IGM) which suppresses the concentration of baryons in shallow potentials (Efstathiou 1992). More recent models identify the possible low-redshift signature of such heating in the faint end of the galaxy luminosity function, most notably in the abundance of the dwarf satellite galaxies in the local group (e.g. Tully et al. 2002; Benson et al. 2002).

Gnedin (2000) showed that the effect of photoionization heating on the gas content of a halo of mass $M_{\rm vir}$ can be modelled by defining a characteristic mass scale, the so called *filtering mass*, $M_F$, below which the gas fraction $f_b$ is reduced relative to the universal value:

$$f_{\rm b}^{\rm halo}(z, M_{\rm vir}) = \frac{f_{\rm b}^{\rm cosmic}}{(1 + 0.26\, M_F(z)/M_{\rm vir})^3} \;. \tag{6.6}$$

The filtering mass is a function of redshift and changes most significantly around the epoch of reionization. It was estimated by Gnedin using high-resolution SLH-P$^3$M simulations. Kravtsov et al. (2004) provided an analytic model for these results which distinguishes three 'phases' in the evolution of the IGM: $z > z_0$, the epoch before the first HII regions overlap; $z_0 < z < z_r$, the epoch when multiple HII regions overlap; $z < z_r$, the epoch when the medium is almost fully reionized. They find that choosing $z_0 = 8$ and $z_r = 7$ provides the best fit to the numerically determined filtering mass. We adopt these parameters and keep them fixed throughout our paper. See Appendix B of Kravtsov et al. (2004) for a full derivation and description of the analytic model.

### 6.3.4 Black hole growth, AGN outflows, and cooling suppression

There is a growing body of evidence that active galactic nuclei (AGN) are a critical piece in the galaxy formation puzzle. Our principal interest in this paper is their role in suppressing

cooling flows, thereby modifying the luminosities, colours, stellar masses and clustering of the galaxies that populate the bright end of the galaxy luminosity function. To treat this problem, we first need a physical model for the growth of black holes within our galaxies.

**The 'quasar mode'**

In our model (which is based closely on that of Kauffmann & Haehnelt 2000) supermassive black holes grow during galaxy mergers both by merging with each other and by accretion of cold disk gas. We assume that the gas mass accreted during a merger is proportional to the total cold gas mass present, but with an efficiency which is lower for smaller mass systems and for unequal mergers. Specifically,

$$\Delta m_{\mathrm{BH,Q}} = \frac{f'_{\mathrm{BH}}\, m_{\mathrm{cold}}}{1 + (280\,\mathrm{km\,s^{-1}}/V_{\mathrm{vir}})^2} \, , \tag{6.7}$$

where we have changed the original parameterisation by taking

$$f'_{\mathrm{BH}} = f_{\mathrm{BH}}\,(m_{\mathrm{sat}}/m_{\mathrm{central}}) \, . \tag{6.8}$$

Here $f_{\mathrm{BH}} \approx 0.03$ is a constant and is chosen to reproduce the observed local $m_{\mathrm{BH}} - m_{\mathrm{bulge}}$ relation (Magorrian et al. 1998; Marconi & Hunt 2003; Häring & Rix 2004). In contrast to Kauffmann & Haehnelt (2000) we allow black hole accretion during both major *and* minor mergers although the efficiency in the latter is lower because of the $m_{\mathrm{sat}}/m_{\mathrm{central}}$ term. Thus, any merger-induced perturbation to the gas disk (which might come from a bar instability or a merger-induced starburst – see Section 6.3.7) can drive gas onto the central black hole. In this way, minor merger growth of the black hole parallels minor merger growth of the bulge. The fractional contribution of minor mergers to both is typically quite small, so that accretion driven by major mergers is the dominant mode of black hole growth in our model. We refer to this as the 'quasar mode'. [Note that a more schematic treatment of black hole growth would suffice for the purposes of this paper, but in Springel et al (2005) and in future work we wish to examine the build-up of the black hole population within galaxies in considerably more detail.]

**The 'radio mode'**

In our model, low energy 'radio' activity is the result of hot gas accretion onto a central supermassive black hole once a static hot halo has formed around the black hole's host galaxy. We assume this accretion to be continual and quiescent and to be described by a simple phenomenological model:

$$\dot{m}_{\mathrm{BH,R}} = \kappa_{\mathrm{AGN}} \Big( \frac{m_{\mathrm{BH}}}{10^8 M_\odot} \Big) \Big( \frac{f_{\mathrm{hot}}}{0.1} \Big) \Big( \frac{V_{\mathrm{vir}}}{200\,\mathrm{km\,s^{-1}}} \Big)^3 \, , \tag{6.9}$$

where $m_{\mathrm{BH}}$ is the black hole mass, $f_{\mathrm{hot}}$ is the fraction of the total halo mass in the form of hot gas, $V_{\mathrm{vir}} \propto T_{\mathrm{vir}}^{1/2}$ is the virial velocity of the halo, and $\kappa_{\mathrm{AGN}}$ is a free parameter with units

of $M_\odot \, yr^{-1}$ with which we control the efficiency of accretion. We find below that $\kappa_{AGN} = 6\times$ $10^{-6} M_\odot \, yr^{-1}$ accurately reproduces the turnover at the bright end of the galaxy luminosity function. Note that $f_{hot} V_{vir}^3 t_H$ is proportional to the total mass of hot gas, so that our formula is simply the product of the hot gas and black hole masses multiplied by a constant efficiency and divided by the Hubble time $t_H$. In fact, we find $f_{hot}$ to be approximately constant for $V_{vir} \gtrsim 150 \, km \, s^{-1}$, so the dependence of $\dot{m}_{BH,R}$ on this quantity has little effect. The accretion rate given by Eq. 6.9 is typically orders-of-magnitude below the Eddington limit. In Section 6.5 we discuss physical accretion models which may reproduce this phenomenology.

We assume that 'radio mode' feedback injects sufficient energy into the surrounding medium to reduce or even stop the cooling flow described in Section 6.3.2. We take the mechanical heating generated by the black hole accretion of Eq. 6.9 to be

$$L_{BH} = \eta \, \dot{m}_{BH} \, c^2 \, , \tag{6.10}$$

where $\eta = 0.1$ is the standard efficiency with which mass is assumed to produce energy near the event horizon, and $c$ is the speed of light. This injection of energy compensates in part for the cooling, giving rise to a modified infall rate (Eq. 6.5) of

$$\dot{m}'_{cool} = \dot{m}_{cool} - \frac{L_{BH}}{\frac{1}{2} V_{vir}^2} \, . \tag{6.11}$$

For consistency we never allow $\dot{m}'_{cool}$ to fall below zero. It is worth noting that $\dot{m}_{cool} \propto f_{hot}^{3/2} \, \Lambda(V_{vir})^{1/2} \, V_{vir}^2 \, t_H^{-1/2}$ (Eq. 6.5) and $\dot{m}_{heat} \equiv 2 L_{BH}/V_{vir}^2 \propto m_{BH} \, f_{hot} \, V_{vir}$ (Eq. 6.11), so that

$$\frac{\dot{m}_{heat}}{\dot{m}_{cool}} \propto \frac{m_{BH} \, t_H^{1/2}}{f_{hot}^{1/2} \, \Lambda(V_{vir})^{1/2} \, V_{vir}} \, . \tag{6.12}$$

(These scalings are exact for an EdS universe; we have omitted weak coefficient variations in other cosmologies.) Thus in our model the effectiveness of radio AGN in suppressing cooling flows is greatest at late times and for large values of black hole mass. This turns out to be the qualitative behaviour needed for the suppression of cooling flows to reproduce successfully the luminosities, colours and clustering of low redshift bright galaxies.

**The growth of supermassive black holes**

Fig. 6.3 shows the evolution of the mean black hole accretion rate per unit volume averaged over the entire Millennium Simulation. We separate the accretion into the 'quasar' and 'radio' modes described above (solid and dashed lines respectively). Black hole mass growth in our model is dominated by the merger-driven 'quasar mode', which is most efficient at redshifts of two to four, dropping by a factor of five by redshift zero. This behaviour has similar form to but is weaker than the observed evolution with redshift of the bright quasar population (e.g. Hartwick & Schade 1990). (See also the discussion in Kauffmann & Haehnelt 2000). In contrast, our 'radio mode' is significant only at late
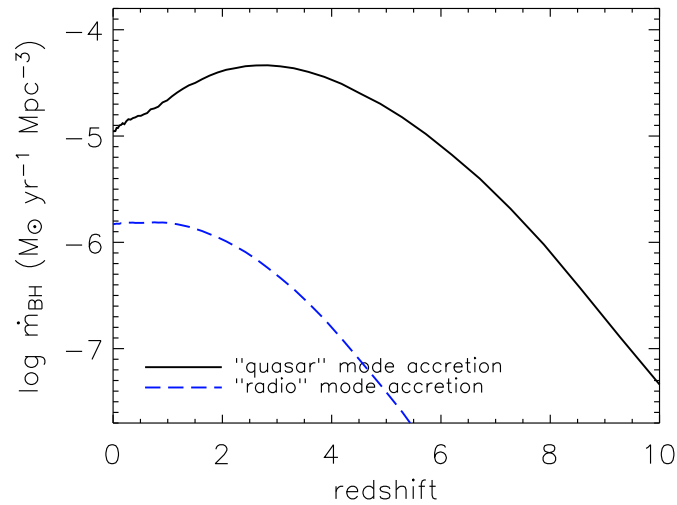
**Figure 6.3:** The black hole accretion rate density, $\dot{m}_{BH}$, as a function of redshift for both the 'quasar' and the 'radio' modes discussed in Section 6.3.4. This figure shows that the growth of black holes is dominated by the 'quasar mode' at high redshift and falls off sharply at $z \lesssim 2$. In contrast, the 'radio mode' becomes important at low redshifts where it suppresses cooling flows, but is not a significant contributor to the overall black hole mass budget.

times, as expected from the scaling discussed above, and for the high feedback efficiency assumed in Eq. 6.10 it contributes only 5% of the final black hole mass density. We will show, however, that the outflows generated by this accretion can have a major impact on the final galaxy properties. Finally, integrating the accretion rate density over time gives a present day black hole mass density of $3 \times 10^5 M_\odot \mathrm{Mpc}^3$, consistent with recent observational estimates (Yu & Tremaine 2002; Merloni 2004).

The relationship between black hole mass and bulge mass is plotted in Fig. 6.4 for the local galaxy population in our 'best' model. In this figure, the solid line shows the best fit to the observations given by Häring & Rix (2004) for a sample of 30 nearby galaxies with well measured bulge and black hole masses. Their results only probe masses over the range bounded by the dashed lines. Our model galaxies produces a good match to these observations with comparable scatter in the observed range (see their Fig. 2).

### 6.3.5 Star formation

We use a simple model for star formation similar to those adopted by earlier authors. We assume that all star formation occurs in cold disk gas, either quiescently or in a burst (see Section 6.3.7). Based on the observational work of Kennicutt (1998), we adopt a threshold surface density for the cold gas below which no stars form, but above which gas starts to collapse and form stars. According to Kauffmann (1996), this critical surface density may
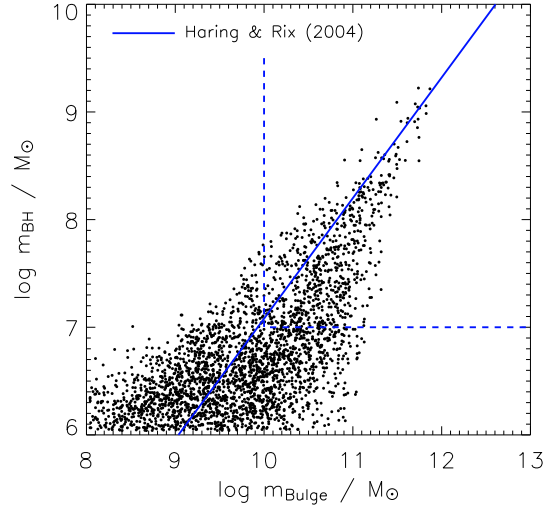
**Figure 6.4:** The black hole-bulge mass relation for model galaxies at the present day. The local observational result of Häring & Rix (2004) is given by the solid line, where the dashed box shows the approximate range over which their fi t was obtained.

be approximated by

$$\Sigma_{\text{crit}}(\text{M}_\odot\text{pc}^{-2}) = 0.59\,\text{V}(\text{kms}^{-1})/\text{R}(\text{kpc})\,. \tag{6.13}$$

We convert this critical surface density into a critical mass by assuming the cold gas mass to be evenly distributed over the disk. The resulting critical cold gas mass is:

$$m_{\text{crit}} = 3.8 \times 10^9 \Big(\frac{V_{\text{vir}}}{200\,\text{km s}^{-1}}\Big)\Big(\frac{r_{\text{D}}}{10\,\text{kpc}}\Big)\text{M}_\odot\,, \tag{6.14}$$

where we assume the disk scale length to be $r_s = (\lambda/\sqrt{2})R_{\text{vir}}$ (Mo et al. 1998), and set the outer disk radius to $r_{\text{D}} = 3r_s$, based on the properties of the Milky Way (van den Bergh 2000). Here $\lambda$ is the spin parameter of the dark halo in which the galaxy resides (Bullock et al. 2001), measured directly from the simulation. When the mass of cold gas in a galaxy is greater than this critical value we assume the star formation rate to be

$$\dot{m}_* = \alpha_{\text{SF}}\,(m_{\text{cold}} - m_{\text{crit}})\,/\,t_{\text{dyn,D}}\,, \tag{6.15}$$

where the efficiency $\alpha_{\text{SF}}$ is typically set so that 5 to 15 percent of the gas is converted into stars in a disk dynamical time $t_{\text{dyn,D}}$, which we define to be $r_{\text{D}}/V_{\text{vir}}$. This star formation model produces a global star formation history consistent with the observed star formation density of the universe out to at least $z=3$, as shown in Fig. 6.5.
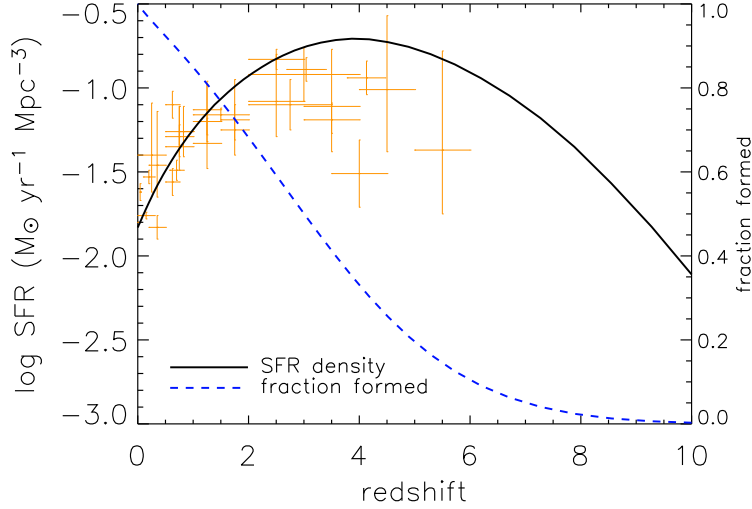
**Figure 6.5:** The star formation rate density of the universe as a function of redshift. The symbols show a compilation of observational results taken from Fig. 12 of Springel & Hernquist (2003b). The solid line shows our 'best' model, which predicts that galaxies form much of their mass relatively early. The dashed line (and right axis) indicate the increase in stellar mass with redshift. Approximately 50% of all stars form by $z = 3$.

When implemented in our model, Eq. 6.15 leads to episodic star formation that self-regulates so as to maintain the critical surface density of Eq. 6.13. This naturally reproduces the observed spiral galaxy gas fractions without the need for additional parameterisation, as we demonstrate in the top panel of Fig. 6.6 using model Sb/c galaxies identified as objects with bulge-to-total luminosity: $1.5 \leq M_{\text{I,bulge}} - M_{\text{I,total}} \leq 2.5$.

## 6.3.6 Supernova feedback

As star formation proceeds, newly formed massive stars rapidly complete their evolution and end their life as supernovae. These events inject gas, metals and energy into the surrounding medium, reheating cold disk gas and possibly ejecting gas even from the surrounding halo.

The observations of Martin (1999) suggest modelling the amount of cold gas reheated by supernovae as

$$\Delta m_{\text{reheated}} = \epsilon_{\text{disk}} \Delta m_* , \qquad (6.16)$$

where $\Delta m_*$ is the mass of stars formed over some finite time interval and $\epsilon_{\text{disk}}$ is a parameter which we fix at $\epsilon_{\text{disk}} = 3.5$ based on the observational data. The energy released in this interval can be approximated by

$$\Delta E_{\text{SN}} = 0.5 \, \epsilon_{\text{halo}} \, \Delta m_* V_{\text{SN}}^2 , \qquad (6.17)$$
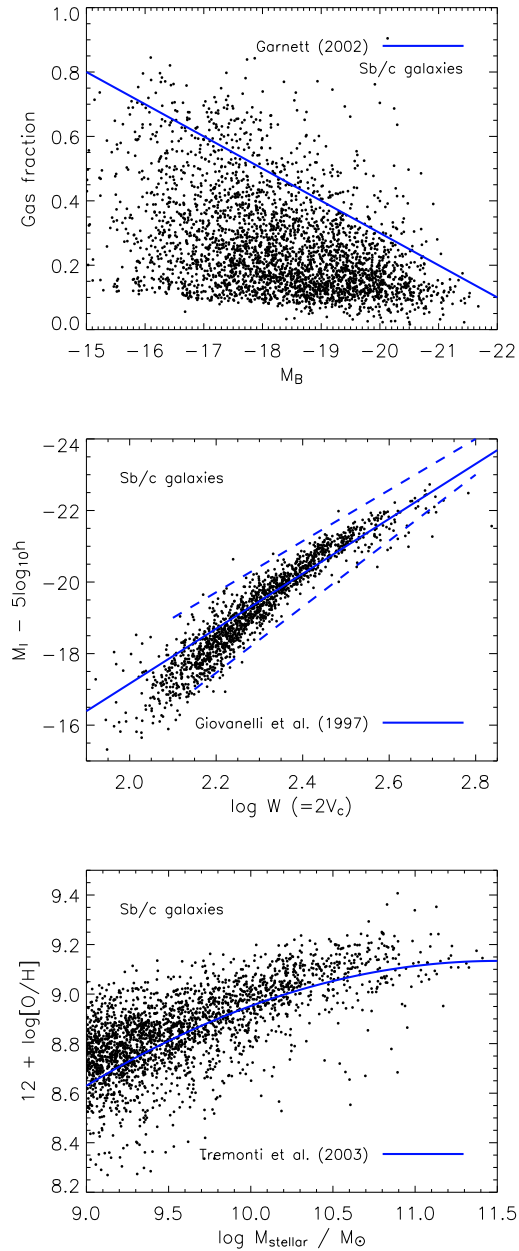
**Figure 6.6:** Selected results for Sb/c galaxies (identified by bulge-to-total luminosity, see Section 6.3.5) for our best model. (top) Gas fractions as a function of B-band magnitude. The solid line is a representation of the mean behaviour in the (incomplete) sample of Garnett (2002). (middle) The Tully-Fisher relation, where the disk circular velocity, $V_c$, is approximated by $V_{vir}$ for the dark halo. The solid line with surrounding dashed lines represents the mean result and scatter found by Giovanelli et al. (1997). (bottom) Cold gas metallicity as a function of total stellar mass. The solid line represents the result of Tremonti et al. (2004).

115

where $0.5\,V_{SN}^2$ is the mean energy in supernova ejecta per unit mass of stars formed, and $\epsilon_{halo}$ parametrises the efficiency with which this energy is able to reheat disk gas. Based on a standard initial stellar mass function and standard supernova theory we take $V_{SN} = 630\,\text{km}\,\text{s}^{-1}$. In addition, for our 'best' model we adopt $\epsilon_{halo} = 0.35$. If the reheated gas were added to the hot halo without changing its specific energy, its total thermal energy would change by

$$\Delta E_{hot} = 0.5\,\Delta m_{reheated}\,V_{vir}^2\,. \tag{6.18}$$

Thus the *excess* energy in the hot halo after reheating is just $\Delta E_{excess} = \Delta E_{SN} - \Delta E_{hot}$. When $\Delta E_{excess} < 0$ the energy transferred with the reheated gas is insufficient to eject any gas out of the halo and we assume all hot gas remains associated with the halo. When excess energy is present, i.e. $\Delta E_{excess} > 0$, we assume that some of the hot gas is ejected from the halo into an external 'reservoir'. Specifically, we take

$$\Delta m_{ejected} = \frac{\Delta E_{excess}}{E_{hot}} m_{hot} = \Big(\epsilon_{halo}\frac{V_{SN}^2}{V_{vir}^2} - \epsilon_{disk}\Big)\Delta m_*\,, \tag{6.19}$$

where $E_{hot} = 0.5\,m_{hot}V_{vir}^2$ is the total thermal energy of the hot gas, and we set $\Delta m_{ejected} = 0$ when this equation gives negative values (implying $\Delta E_{excess} < 0$ discussed above). This is similar to the traditional semi-analytic feedback recipe, $\Delta m_{ejected} \propto \Delta m_*/V_{vir}^2$, but with a few additions. For small $V_{vir}$ the entire hot halo can be ejected and then $\Delta m_{ejected}$ must saturate at $\Delta m_{reheated}$. Conversely, no hot gas can be ejected from the halo for $V_{vir}^2 > \epsilon_{halo}V_{SN}^2/\epsilon_{disk}$, i.e. for halo circular velocities exceeding about $200\,\text{km}\,\text{s}^{-1}$ for our favoured parameters.

Ejected gas leaves the galaxy and its current halo in a wind or 'super-wind', but it need not be lost permanently. As the dark halo grows, some of the surrounding ejecta may fall back in and be reincorporated into the cooling cycle. We follow Springel et al. (2001a) and De Lucia et al. (2004) and model this by assuming

$$\dot{m}_{ejected} = -\gamma_{ej}\,m_{ejected}\,/\,t_{dyn}\,, \tag{6.20}$$

where $\gamma_{ej}$ controls the amount of reincorporation per dynamical time; typically we take $\gamma_{ej} = 0.3$ to $1.0$. Such values imply that all the ejected gas will return to the hot halo in a few halo dynamical times.

The prescriptions given in this section are simple, as well as physically and energetically plausible, but they have little detailed justification either from observation or from numerical simulation. They allow us to track in a consistent way the exchange of each halo's baryons between our four phases (stars, cold disk gas, hot halo gas, ejecta), but should be regarded as a rough attempt to model the complex astrophysics of feedback which will surely need significant modification as the observational phenomenology of these processes is explored in more depth. In particular, there is substantial evidence for strong hydrodynamic feedback from optical/UV and X-ray AGN (Arav et al. 2001; de Kool et al. 2001; Reeves et al. 2003; Crenshaw et al. 2003). We have not yet explicitly incorporated such feedback in our modelling, and it may well turn out to be important (see, for example,

the recent simulations of di Matteo et al. 2005)). We assume 'quasar mode' accretion to be closely associated with starbursts, so this feedback channel may be partially represented in our models by an enhanced effective feedback efficiency associated with star formation and supernovae.

**The growth of stellar mass**

Supernova feedback and star formation act together to regulate the stellar growth of a galaxy. This is especially important for $L < L^*$ galaxies, where feedback can eject most of the baryons from the system, reducing the supply of star-forming material for time periods much longer than the cooling/supernova heating cycle. In the middle panel of Fig. 6.6 we plot the Tully-Fisher relation for model Sb/c galaxies (see Section 6.3.5). The Tully-Fisher relation is strongly influenced by the link between star formation and supernova heating. The circular velocity of a galactic disk is (to first order) proportional to the virial velocity of the host dark matter halo and thus to its escape velocity. In our model (and most others) this is closely related to the ability of the galaxy to blow a wind. The luminosity of a galaxy is determined by its ability to turn its associated baryons into stars. The overall efficiency of this process in the face of supernova and AGN feedback sets the amplitude of the Tully-Fisher relation, while the way in which the efficiency varies between systems of different circular velocity has a strong influence on the slope.

The Tully-Fisher relation predicted by our model (middle panel of Fig. 6.6) is a reasonable match to the observational data of Giovanelli et al. (1997), demonstrating that our simple star formation and feedback recipes can adequately represent the growth of stellar mass across a wide range of scales. We find clear deviations from power law behaviour for $\log W \lesssim 2.3$ (approximately $V_c \lesssim 100\,\mathrm{km\,s^{-1}}$), where the efficiency of removing gas from low mass systems combines with our threshold for the onset of star formation to reduce the number of stars that can form. The resulting downward bend is qualitatively similar to that pointed out in real data by McGaugh et al. (2000). These authors show that including the gaseous component to construct a 'baryonic' Tully-Fisher relation brings the observed points much closer to a power-law, and the same is true in the model we present here. Limiting star formation in galaxies that inhabit shallow potentials has a strong effect on the faint-end of the galaxy luminosity function, as will be seen in Section. 6.4.2.

## 6.3.7 Galaxy morphology, merging and starbursts

In the model we discuss here, the morphology of a galaxy is assumed to depend only on its bulge-to-total luminosity ratio, which in turn is determined by three distinct physical processes: disk growth by accretion, disk buckling to produce bulges, and bulge formation through mergers. We treat disk instabilities using the simple analytic stability criterion of Mo et al. (1998); the stellar disk of a galaxy becomes unstable when the following inequality is met,

$$\frac{V_c}{(Gm_{\mathrm{D}}/r_{\mathrm{D}})^{1/2}} \leq 1 \,, \tag{6.21}$$

where we approximate the circular velocity of the disk by $V_c = V_{\mathrm{vir}}$. For each galaxy at each time-step we evaluate the left-hand side of Eq. 6.21, and if it is smaller than unity we transfer enough stellar mass from disk to bulge (at fixed $r_{\mathrm{D}}$) to restore stability.

Galaxy mergers shape the evolution of galaxies, affecting both their morphology and (through induced starbursts) their star formation history. Mergers can occur in our model between the central galaxy of a dark halo or subhalo and a satellite galaxy which has lost its own dark subhalo. Substructure is followed in the Millennium Run down to a 20 particle limit, which means that the orbit of a satellite galaxy within a larger halo is followed explicitly until its subhalo mass drops below $1.7 \times 10^{10} h^{-1} M_{\odot}$. After this point, the satellite's position and velocity are represented by those of the most bound particle of the subhalo at the last time it was identified. At the same time, however, we start a merger 'clock' and estimate a merging time for the galaxy using the dynamical friction formula of Binney & Tremaine (1987),

$$t_{\mathrm{friction}} = 1.17 \frac{V_{\mathrm{vir}} r_{\mathrm{sat}}^2}{G m_{\mathrm{sat}} \ln \Lambda} \; . \tag{6.22}$$

This formula is valid for a satellite of mass $m_{\mathrm{sat}}$ orbiting in an isothermal potential of circular velocity $V_{\mathrm{vir}}$ at radius $r_{\mathrm{sat}}$. We take $m_{\mathrm{sat}}$ and $r_{\mathrm{sat}}$ to be the values measured for the galaxy at the last time its subhalo could be identified. The Coulomb logarithm is approximated by $\ln \Lambda = \ln(1 + M_{\mathrm{vir}}/m_{\mathrm{sat}})$.

The outcome of the merger will depend on the baryonic mass ratio of the two progenitors . When one dominates the process, i.e. a small satellite merging with a larger central galaxy, the stars of the satellite are added to the bulge of the central galaxy and a minor merger starburst (see below) will result. The cold gas of the satellite is added to the disk of the central galaxy along with any stars that formed during the burst. Such an event is called a *minor merger*.

If, on the other hand, the masses of the progenitors are comparable a *major merger* will result. Under these circumstances the starburst is more significant, with the merger destroying the disks of both galaxies to form a spheroid in which all stars are placed. The dividing line between a major and minor merger is given by the parameter $T_{\mathrm{merger}}$: when the mass ratio of the merging progenitors is larger than $T_{\mathrm{merger}}$ a major merger results, otherwise the event is a minor merger. Following Springel et al. (2001a) we choose $T_{\mathrm{merger}} = 0.3$ and keep this fixed throughout.

Our starburst implementation is based on the 'collisional starburst' model of Somerville et al. (2001). In this model, a fraction $e_{\mathrm{burst}}$ of the combined cold gas from the two galaxies is turned into stars as a result of the merger:

$$e_{\mathrm{burst}} = \beta_{\mathrm{burst}} (m_{\mathrm{sat}}/m_{\mathrm{central}})^{\alpha_{\mathrm{burst}}} \; , \tag{6.23}$$

where the two parameters are taken as $\alpha_{\mathrm{burst}} = 0.7$ and $\beta_{\mathrm{burst}} = 0.56$. This model provides a good fit to the numerical results of Cox et al. (2004) and also Mihos & Hernquist (1994, 1996) for merger mass ratios ranging from 1:10 to 1:1.

### 6.3.8 Spectroscopic evolution and dust

The photometric properties of our galaxies are calculated using stellar population synthesis models from Bruzual & Charlot (1993). Our implementation is fully described in De Lucia et al. (2004) and we refer the reader there (and to references therein) for further details.

To include the effects of dust when calculating galaxy luminosities we apply the simple 'plane-parallel slab' model of Kauffmann et al. (1999). This model is clearly oversimplified, but it permits us to make a reasonable first-order correction for dust extinction in actively star-forming galaxies. For the details of this model we refer the reader to Kauffmann et al. (1999) and to references therein.

### 6.3.9 Metal enrichment

Our treatment of metal enrichment is essentially identical to that described in De Lucia et al. (2004). In this model a yield $Y$ of heavy elements is returned for each solar mass of stars formed. These metals are produced primarily in the supernovae which terminate the evolution of short-lived, massive stars. In our model we deposit them directly into the cold gas in the disk of the galaxy. (An alternative would clearly be to add some fraction of the metals directly to the hot halo. Limited experiments suggest that this makes little difference to our main results.) We also assume that a fraction $R$ of the mass of newly formed stars is recycled immediately into the cold gas in the disk, the so called 'instantaneous recycling approximation' (see Cole et al. 2000). For full details on metal enrichment and exchange processes in our model see De Lucia et al. (2004). In the bottom panel of Fig. 6.6 we show the metallicity of cold disk gas for model Sb/c galaxies (selected, as before, by bulge-to-total luminosity, as described in Section 6.3.5) as a function of total stellar mass. For comparison, we show the result of Tremonti et al. (2004) for mean HII region abundances in SDSS galaxies.

## 6.4 Results

In this section we examine how the suppression of cooling flows in massive systems affects galaxy properties. As we will show, the effects are only important for high mass galaxies. Throughout our analysis we use the galaxy formation model outlined in the previous sections with the parameter choices of Table 6.1 except where explicitly noted.

### 6.4.1 The suppression of cooling flows

We begin with Fig. 6.7, which shows how our 'radio mode' heating model modifies gas condensation. We compare mean condensation rates with and without the central AGN heating source as a function of halo virial velocity (solid and dashed lines respectively). Recall that virial velocity provides a measure of the equilibrium temperature of the system through $T_{\mathrm{vir}} \propto V_{\mathrm{vir}}^2$, as indicated by the scale on the top axis. The four panels show the behaviour at four redshifts between six and the present day. The vertical dotted line in
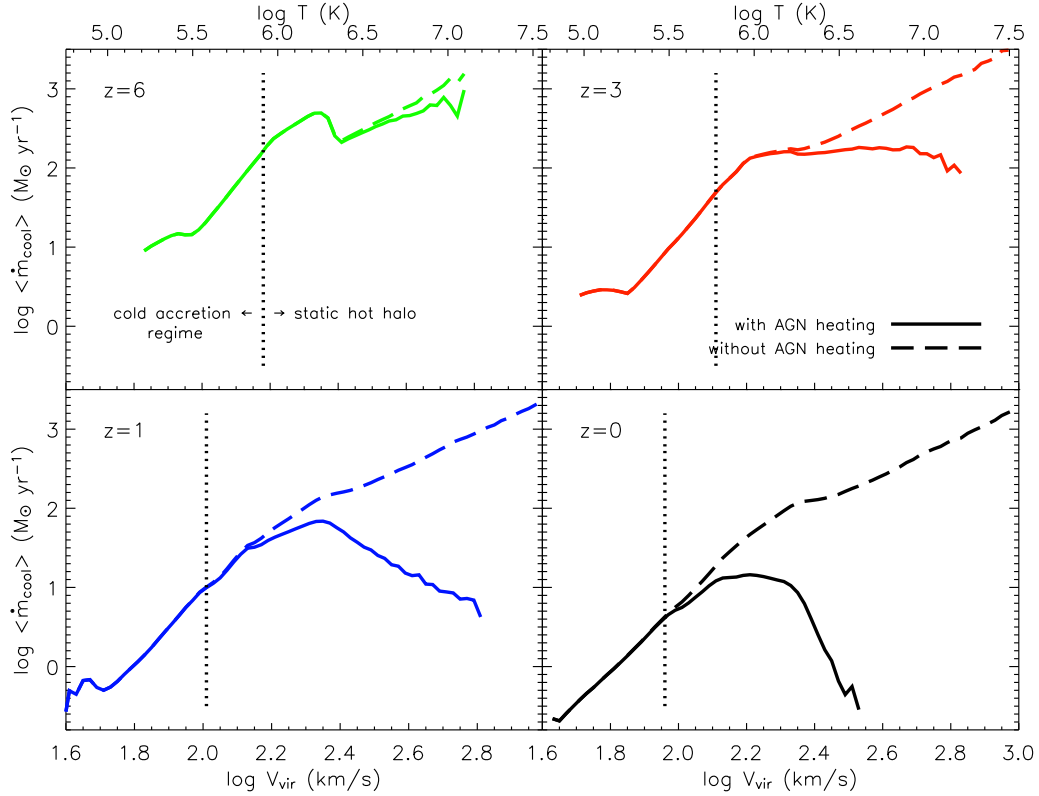
**Figure 6.7:** The mean condensation rate, $\langle \dot{m}_{cool} \rangle$ as a function of halo virial velocity $V_{vir}$ at redshifts of 6, 3, 1, and 0. Solid and dashed lines in each panel represent the condensation rate with and without 'radio mode' feedback respectively, while the vertical dotted lines show the transition between the rapid cooling and static hot halo regimes, as discussed in Section 6.3.2. This figure demonstrates that cooling flow suppression is most efficient in our model for haloes with $V_{vir} > 150\,\mathrm{km\,s^{-1}}$ and at $z \leq 3$.

each panel marks haloes for which $r_{cool} = R_{vir}$, the transition between systems that form static hot haloes and those where infalling gas cools rapidly onto the central galaxy disk (see section 6.3.2 and Fig. 6.2). This transition moves to haloes of lower temperature with time, suggesting a 'down-sizing' of the characteristic mass of actively star-forming galaxies. At lower $V_{vir}$ gas continues to cool rapidly, while at higher $V_{vir}$ new fuel for star formation must come from cooling flows which are affected by 'radio mode' heating.

The effect of 'radio mode' feedback is clearly substantial. Suppression of condensation becomes increasingly effective with increasing virial temperature and decreasing redshift. The effects are large for haloes with $V_{vir} \gtrsim 150\,\mathrm{km\,s^{-1}}$ ($T_{vir} \gtrsim 10^6\mathrm{K}$) at $z \lesssim 3$. Condensation stops almost completely between $z = 1$ and the present in haloes with $V_{vir} > 300\,\mathrm{km\,s^{-1}}$

($T_{\mathrm{vir}} > 3 \times 10^6$K). Such systems correspond to the haloes of groups and clusters which are typically observed to host massive elliptical or CD galaxies at their centres. Our scheme thus produces results which are qualitatively similar to the *ad hoc* suppression of cooling flows assumed in previous models of galaxy formation. For example, Kauffmann et al. (1999) switched off gas condensation in all haloes with $V_{\mathrm{vir}} > 350\,\mathrm{km\,s^{-1}}$, while Hatton et al. (2003) stopped condensation when the bulge mass exceeded a critical threshold.

## 6.4.2 Galaxy properties with and without AGN heating

The suppression of cooling flows in our model has a dramatic effect on the bright end of the galaxy luminosity function. In Fig. 6.8 we present K- and b$_{\mathrm{J}}$-band luminosity functions (left and right panels respectively) with and without 'radio mode' feedback (solid and dashed lines respectively). The luminosities of bright galaxies are reduced by up to two magnitudes when the feedback is switched on, and this induces a relatively sharp break in the luminosity function which matches the observations well. We demonstrate this by overplotting K-band data from Cole et al. (2001) and Huang et al. (2003) in the left panel, and b$_{\mathrm{J}}$-band data from Norberg et al. (2002) in the right panel. In both band-passes the model is quite close to the data over the full observed range. We comment on some of the remaining discrepancies below.

Our feedback model also has a significant effect on bright galaxy colours, as we show in Fig. 6.9. Here we plot the B−V colour distribution as a function of stellar mass, with and without the central heating source (top and bottom panels respectively). In both panels we have colour-coded the galaxy population by morphology as estimated from bulge-to-total luminosity ratio (split at $L_{\mathrm{bulge}}/L_{\mathrm{total}} = 0.4$). Our morphological resolution limit is marked by the dashed line at a stellar mass of $\sim 4 \times 10^9 M_\odot$; this corresponds approximately to a halo of 100 particles in the Millennium Run. Recall that a galaxy's morphology depends both on its past merging history and on the stability of its stellar disk in our model. Both mergers and disk instabilities contribute stars to the spheroid, as described in Section 6.3.7. The build-up of haloes containing fewer than 100 particles is not followed in enough detail to model these processes robustly.

A number of important features can be seen in Fig. 6.9. Of note is the bi-modal distribution in galaxy colours, with a well-defined red sequence of appropriate slope separated cleanly from a broader 'blue cloud'. It is significant that the red sequence is composed predominantly of early-type galaxies, while the blue cloud is comprised mostly of disk-dominated systems. This aspect of our model suggests that that the physical processes which determine morphology (i.e. merging, disk instability) are closely related to those which control star formation history (i.e. gas supply) and thus determine galaxy colour. The red and blue sequences both display a strong metallicity gradient from low to high mass (c.f. Fig. 6.6), and it is this which induces a 'slope' in the colour-magnitude relations which agrees well with observation (e.g. Baldry et al. 2004).

By comparing the upper and lower panels in Fig. 6.9 we can see how 'radio mode' feedback modifies the luminosities and colours of high mass galaxies. Not surprisingly, the brightest and most massive galaxies are also the reddest when cooling flows are sup-
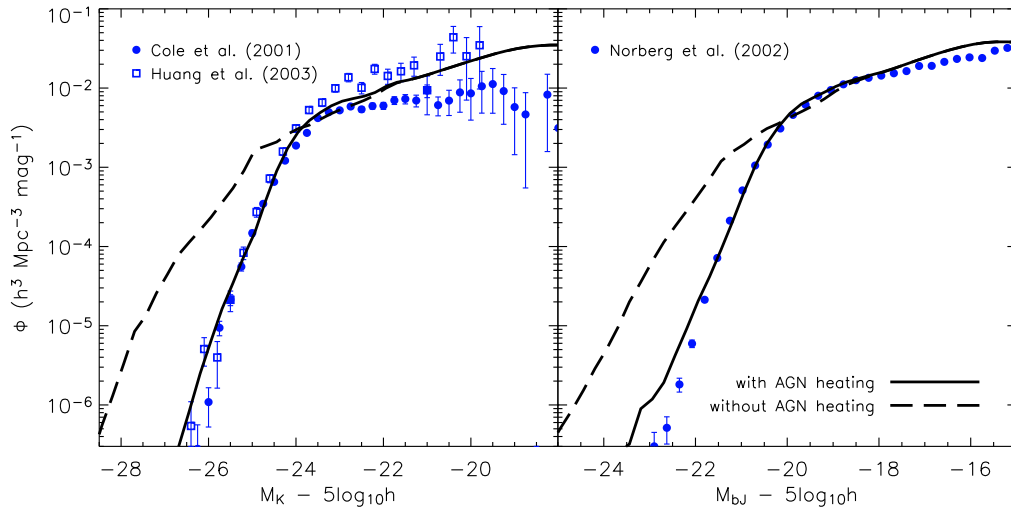
**Figure 6.8:** Galaxy luminosity functions in the K (left) and b$_J$ (right) photometric bands, plotted with and without 'radio mode' feedback (solid and long dashed lines respectively – see Section 6.3.4). Symbols indicate observational results as listed in each panel. As can be seen, the inclusion of AGN heating produces a good fit to the data in both colours. Without this heating source our model overpredicts the luminosities of massive galaxies by about two magnitudes and fails to reproduce the sharp bright end cut-offs in the observed luminosity functions.

pressed, whereas they are brighter, more massive and much bluer if cooling flows continue to supply new material for star formation. AGN heating cuts off the gas supply to the disk from the surrounding hot halo, truncating star formation and allowing the existing stellar population to redden. However, these massive red galaxies do continue to grow through merging. (The gas required to fuel starbursts is rapidly used up in the absence of continuing condensation.) Through this mechanism the most massive cluster galaxies are able to gain a factor of two or three in mass without significant star formation, similar to that recently observed Bell et al. (2005). This late-stage (i.e. $z \lesssim 1$) hierarchical growth moves objects to higher mass without changing their colours.

It is also interesting to examine effect of AGN heating on the stellar ages of galaxies. In Fig. 6.10 the solid and dashed lines show mean stellar age as a function of stellar mass for models with and without 'radio mode' feedback, while error bars indicate the *rms* scatter around the mean. Substantial differences are seen for galaxies with $M_{\mathrm{stellar}} \gtrsim 10^{11} M_\odot$: the mean age of the most massive galaxies approaching 12 Gyr when cooling flows are suppressed but remaining around 8 Gyr when feedback is switched off. Such young ages are clearly inconsistent with the old stellar populations observed in the majority of massive cluster ellipticals.
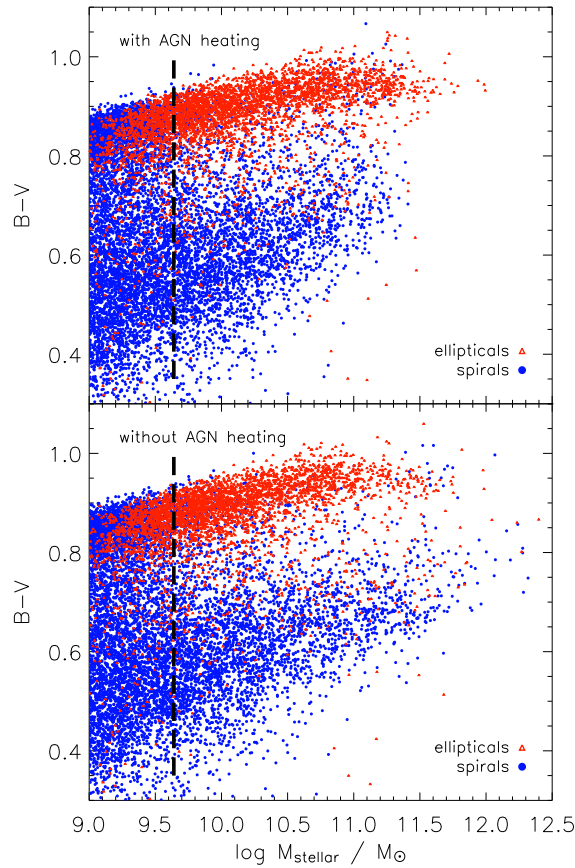
**Figure 6.9:** The $B-V$ colours of model galaxies plotted as a function of their stellar mass with (top) and without (bottom) 'radio mode' feedback (see Section 6.3.4). A clear bi-modality in colour is seen in both panels, but without a heating source the most massive galaxies are blue rather than red. Only when heating is included are massive galaxies as red as observed. Triangles (red) and circles (blue) correspond to early and late morphological types respectively, as determined by bulge-to-total luminosity ratio (see Section 6.4.2). The thick dashed lines mark the resolution limit to which morphology can reliably be determined in the Millennium Run.

The colour bi-modality in Fig. 6.9 is so pronounced that it is natural to divide our model galaxies into red and blue populations and to study their properties separately. We do this by splitting at $B-V = 0.8$, an arbitrary but natural choice. Fig. 6.11 shows separate $b_J$ luminosity functions for the resulting populations. For comparison we overplot observational results from Madgwick et al. (2002) for 2dFGRS galaxies split by spectral type. Their luminosity functions are essentially identical to that of Cole et al. (2005), who split

123
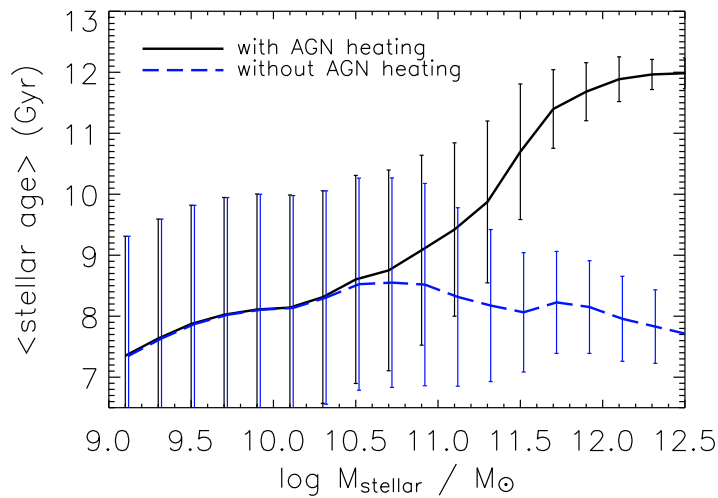
**Figure 6.10:** Mean stellar ages of galaxies as a function of stellar mass for models with and without 'radio mode' feedback (solid and dashed lines respectively). Error bars show the *rms* scatter around the mean for each mass bin. The suppression of cooling flows raises the mean age of high-mass galaxies to large values, corresponding to high formation redshifts.

the 2dFGRS catalogue by $b_J$-$r_F$ colour. It thus can serve to indicate the observational expectations for populations of different colour. The broad behaviour of the red and blue populations is similar in the model and in the 2dFGRS. The faint-end of the luminosity function is dominated by late-types, whereas the bright end has an excess of early-types. The two populations have equal abundance about half to one magnitude brighter than $M^*_{b_J}$ (Norberg et al 2002).

Fig. 6.11 also shows some substantial differences between model and observations. The red and blue populations differ more in the real data than they do in the model. There is a tail of very bright blue galaxies in the model, which turn out to be objects undergoing strong, merger-induced starbursts. These correspond in abundance, star formation rate and evolutionary state to the observed population of Ultraluminous Infrared Galaxies (ULIRG's) with the important difference that almost all the luminosity from young stars in the real systems is absorbed by dust and re-emitted in the mid- to far-infrared (Sanders & Mirabel 1996). Clearly we need better dust modelling than our simple 'slab' model (Section 6.3.8) in order to reproduce the properties of such systems adequately. If we suppress starbursts in bright galaxy mergers we find that the blue tail disappears and the observed behaviour recovered. A second and substantial discrepancy is the apparent overproduction faint red galaxies in our model, as compared to the 2dF measurements (however see Popesso et al. 2005; Gonzalez et al. 2005). Further work is clearly needed to understand the extent and significance of this difference.
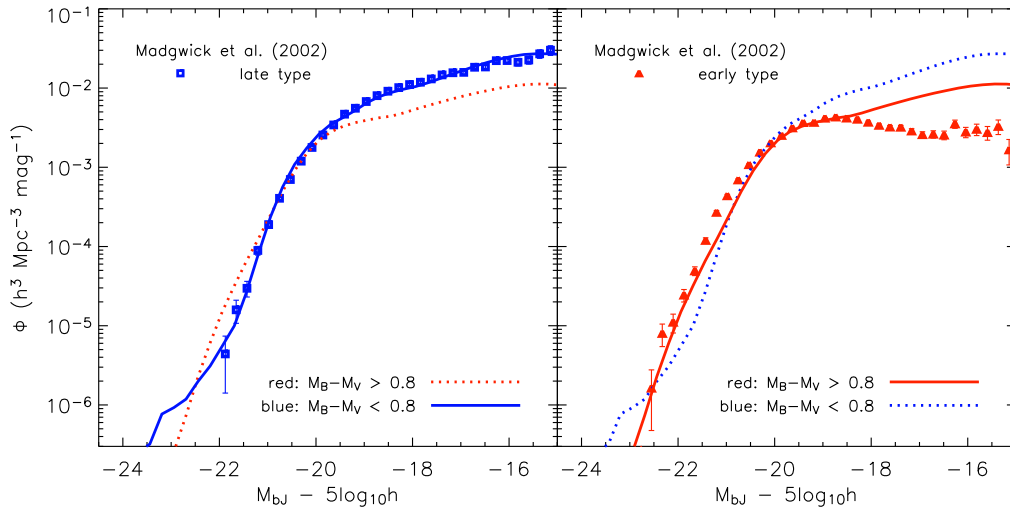
**Figure 6.11:** The b$_J$-band galaxy luminosity function split by colour at B$-$V $=$ 0.8 (Fig. 6.9) into blue (left panel) and red (right panel) sub-populations (solid lines). The dotted lines in each panel repeat the opposite colour luminosity function for reference. Symbols indicate the observational results of Madgwick et al. (2002) for early and late-type 2dFGRS galaxies, split according to spectral type. Although our model split by colour captures the broad behaviour of the observed type-dependent luminosity functions, there are important differences which we discuss in Section 6.4.2.

## 6.5 Physical models of AGN feedback

Our phenomenological model for 'radio mode' feedback (Section 6.3.4) is not grounded in any specific model for hot gas accretion onto a black hole or for the subsequent generation and thermalization of energy through radio outflows. Rather it is based on the observed properties of cooling flows and their central radio sources, and on the need for a source of feedback which can suppress gas condensation onto massive galaxies without requiring the formation of new stars. We have so far focused on the effects of such feedback without discussing how it might be realised. In this section we present two physical arguments which suggest how accretion onto the central black hole may lead to activity in a way which could justify the parameter scalings we have adopted.

### 6.5.1 Cold cloud accretion

A simple picture for cooling flow evolution, based on the similarity solution of Bertschinger (1989) for an unperturbed halo in isolation, can be summarised as follows. Cooling flows develop in any halo where the cooling time of the bulk of the hot gas is longer than the

age of the system so that a static hot halo can form. Such haloes usually have a strong central concentration and we approximate their structure by a singular isothermal sphere. The inner regions then have a local cooling time shorter than the age of the system, and the gas they contain radiates its binding energy and flows inwards. The flow region is bounded by the cooling radius $r_{cool}$ where the local cooling time is equal to the age of the system (see section 6.3.2). This radius increases with time as $t^{1/2}$. As Bertschinger showed, the temperature of the gas *increases* by about 20% as it starts to flow inwards, and its density profile flattens to $\rho_g \propto r^{-3/2}$. Initially, the flow is subsonic and each gas shell sinks stably and isothermally in approximate hydrostatic equilibrium. As it sinks, however, its inward velocity accelerates because its cooling time shrinks more rapidly than the sound travel time across it, and at the sonic radius, $r_{sonic}$, the two become equal. At this point the shell goes into free fall, its temperature decreases rapidly and it may fragment as a result of thermal instability (Cowie et al. 1980; Nulsen 1986; Balbus & Soker 1989). The dominant component of the infalling gas is then in the form of cold clouds and is no longer self-coupled by hydrodynamic forces. Different clouds pursue independent orbits, some with pericentres perhaps orders of magnitude smaller than $r_{sonic}$. If these lie within the zone of influence of the black hole, $r_{BH} = Gm_{BH}/V_{vir}^2$, we assume that some of the cold gas becomes available for fuelling the radio source; otherwise we assume it to be added to the cold gas disk.

The parameter scalings implied by this picture can be estimated as follows. The sound travel time across a shell at the cooling radius is shorter than the cooling time by a factor $\sim r_{cool}/R_{vir}$. At smaller radii the ratio of cooling time to sound travel time decreases as $r^{1/2}$ so that $r_{sonic}/r_{cool} \sim (r_{cool}/R_{vir})^2$ implying $r_{sonic} \sim r_{cool}^3/R_{vir}^2$. If we adopt $r_{sonic} < 10^4 r_{BH} \sim r_{disk}$ as the condition for effective fuelling of the radio source, we obtain

$$m_{BH} > 10^{-4} M_{vir} (r_{cool}/R_{vir})^3 \tag{6.24}$$

as the corresponding minimum black hole mass for fragmented clouds to be captured. Under such conditions, only a small fraction ($\sim 0.01\%$) of the cooling flow mass need be accreted to halt the flow. The ratio in parentheses on the right-hand side of this equation scales approximately as $r_{cool}/R_{vir} \propto (m_{hot}/M_{vir})^{1/2} t_H^{-1/2} V_{vir}^{-1}$, so the minimum black hole mass scales approximately as $(m_{hot}/M_{vir})^{3/2} t_H^{-1/2}$ and is almost independent of $V_{vir}$. In our model, the growth of black holes through mergers and 'quasar mode' accretion produces a population where mass increases with time and with host halo mass. As a result, effective fuelling takes place primarily in the more massive haloes and at late times for this 'cold cloud' prescription.

To test this particular model we switch off our standard phenomenological treatment of 'radio mode' feedback (section 6.3.4), assuming instead that feedback occurs only when Eq. 6.24 is satisfied and that in this case it is sufficient to prevent further condensation of gas from the cooling flow. All other elements of our galaxy and black hole formation model are unchanged. The resulting cooling flow suppression is similar to that seen in Fig. 6.7, and all results presented in Section 6.3 and 6.4 are recovered. An illustration of this is given by Fig. 6.12, where we compare the K-band luminosity function from this particular
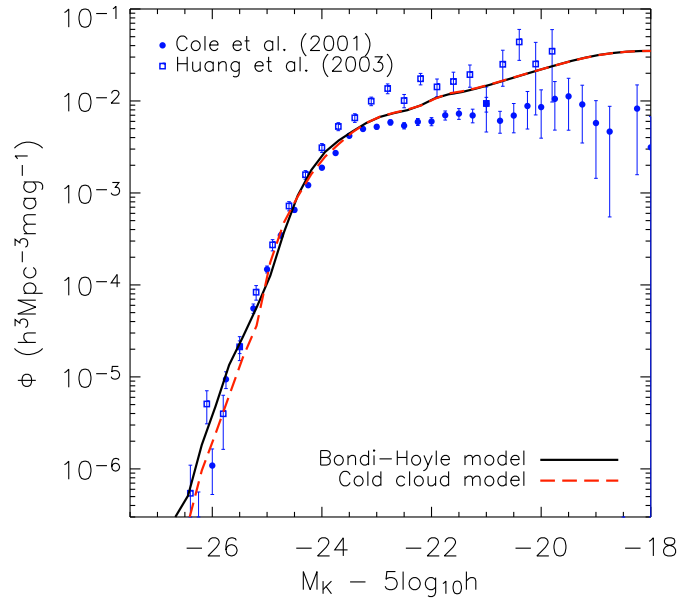
**Figure 6.12:** The observed K-band galaxy luminosity function is compared with the results from models using the two physical prescriptions for 'radio mode' accretion discussed in Section 6.5: the Bondi-Hoyle accretion model (solid line) and the cold cloud accretion model (dashed line). Symbols indicate observational data from Cole et al. (2001) and Huang et al. (2003). Both models can produce a luminosity function which matches observation well.

model (the dashed line) to the observational data (c.f. also Fig. 6.8). The model works so well, of course, because the numerical coefficient in Eq. 6.24 is uncertain and we have taken advantage of this to choose a value which puts the break in the luminosity function at the observed position. This adjustment plays the role of the efficiency parameter $\kappa_{AGN}$ in our standard analysis (see Eq. 6.9).

## 6.5.2 Bondi-Hoyle accretion

Our second physical model differs from the first in assuming that accretion is not from the dominant, cold cloud component which forms within the sonic radius, but rather from a subdominant hot component which fills the space between these clouds. The clouds themselves are assumed to be lost to the star-forming disk. The density profile of the residual hot component was estimated by Nulsen & Fabian (2000) from the condition that the cooling time of each radial shell should remain equal to the sound travel time across it as it flows inwards. This requires the density of the hot component to vary as $1/r$ within $r_{sonic}$ and thermal instabilities must continually convert material into condensed clouds in order to maintain this structure as the hot gas flows in.

The rate at which hot gas is accreted onto the black hole can then be estimated from the Bondi-Hoyle formula (Bondi 1952; Edgar 2004):

$$\dot{m}_{\text{Bondi}} = 2.5\pi G^2 \frac{m_{\text{BH}}^2 \rho_0}{c_s^3} \; . \tag{6.25}$$

Here $\rho_0$ is the (assumed uniform) density of hot gas around the black hole, and in all that follows we approximate the sound speed, $c_s$, by the virial velocity of the halo, $V_{\text{vir}}$. Of course, the density distribution of gas surrounding the black hole is *not* uniform so the question immediately arises as to what density we should choose. We follow a suggestion of E. Churazov and use the value predicted by the 'maximum cooling flow' model of Nulsen & Fabian (2000) at the Bondi radius $r_{Bondi} \equiv 2GM_{\text{BH}}/c_s^2 = 2r_{\text{BH}}$, the conventional boundary of the sphere of influence of the black hole. We therefore equate the sound travel time across a shell at this radius to the local cooling time there:

$$\frac{2r_{\text{Bondi}}}{c_s} \approx \frac{4Gm_{\text{BH}}}{V_{\text{vir}}^3} = \frac{3}{2} \frac{\bar{\mu} m_p kT}{\rho_g(r_{\text{Bondi}})\Lambda(T, Z)} \; . \tag{6.26}$$

Solving for the density gives

$$\rho_0 = \rho_g(r_{\text{Bondi}}) = \frac{3\mu m_p}{8G} \frac{kT}{\Lambda} \frac{V_{\text{vir}}^3}{m_{\text{BH}}} \; . \tag{6.27}$$

Combining Eq. 6.27 with 6.25 provides us with the desired estimate for the hot gas accretion rate onto the black hole:

$$\dot{m}_{\text{Bondi}} \approx G\mu m_p \frac{kT}{\Lambda} m_{\text{BH}} \; . \tag{6.28}$$

Notice that this rate depends only on the black hole mass and on the virial temperature of the halo. It is independent both of time and of $m_{\text{hot}}/M_{\text{vir}}$, the hot gas fraction of the halo. It is valid as long as $r_{\text{Bondi}} < r_{\text{sonic}}$, which is always the case in our models.

To investigate the effects of this model we replace the phenomenological 'radio mode' accretion rate of Eq. 6.9 with that given by Eq. 6.28. Since the latter has no adjustable efficiency, we use the energy generation parameter $\eta$ of Eq. 6.10 to control the effectiveness of cooling flow suppression. (This was not necessary before since $\eta$ always appeared in the product $\eta \kappa_{\text{AGN}}$, where $\kappa_{\text{AGN}}$ is the efficiency parameter of Eq. 6.9.) With this change of black hole accretion and taking $\eta = 0.03$, we are able to recover the results of Sections 6.3 and 6.4 without changing any other aspects of our galaxy and black hole formation model. The final galaxy population is, in fact, almost identical to that presented in previous sections. This is not surprising, perhaps, since Eq. 6.28 has very similar scaling properties to Eq. 6.9. In Fig. 6.12 we illustrate the success of the model by overplotting its prediction for the K-band luminosity function (the solid line) on the observational data and on the prediction of the cold cloud accretion model of the last subsection. The two models agree very closely both with each other and with our standard phenomenological model (see Fig. 6.8).

## 6.6 Conclusions

AGN feedback is an important but relatively little explored element in the co-evolution of galaxies and the supermassive black holes at their centres. In this paper we set up machinery to study this co-evolution in unprecedented detail using the very large Millennium Run, a high-resolution simulation of the growth of structure in a representative region of the concordance $\Lambda$CDM cosmology. Most of our modelling follows earlier work, but in an important extension we introduce a 'radio' feedback mode, based on simple physical models and on the observed phenomenology of radio sources in cooling flows, which suppresses gas condensation at the centres of massive haloes without requiring the formation of new stars. Our modelling produces large catalogues of galaxies and supermassive black holes which can be used to address a very wide range of issues concerning the evolution and clustering of galaxies and AGN. Some clustering results were already presented in Springel et al. (2005). In the present paper, however, we limit ourselves to presenting the model in some detail and to investigating the quite dramatic effects which 'radio mode' feedback can have on the luminosities and colours of massive galaxies. Our main results can be summarised as follows:

(i) We study the amount of gas supplied to galaxies in each of the two gas infall modes discussed by White & Frenk (1991): the 'static halo' mode where postshock cooling is slow and a quasistatic hot atmosphere forms behind the accretion shock; and the 'rapid cooling' mode where the accretion shock is radiative and no such atmosphere is present. We distinguish these modes using the criterion of White & Frenk (1991) which was tested by the 1-D Lagrangian grid simulations of Forcada-Miró & White (1997) and the SPH simulations of Yoshida et al. (2002) and Helly et al. (2003). Our results show a sharp transition between the two regimes at a halo mass of $2$–$3 \times 10^{11} M_\odot$ (see also Birnboim & Dekel 2003 and Keres et al. 2004). This division moves from higher to lower $V_{\mathrm{vir}}$ with time (corresponding approximately to constant $M_{\mathrm{vir}}$), suggesting a 'down-sizing' of star-formation activity as large systems progressively lose their supply of new gas from the rapid cooling regime, and instead must rely on cooling flows to replenish their star-formation reservoirs.

(ii) We have built a detailed model for cooling, star formation, supernova feedback, galaxy mergers and metal enrichment based on the earlier models of Kauffmann et al. (1999), Springel et al (2001a) and De Lucia et al. (2004). Applied to the Millennium Run this model reproduces many of the observed properties of the local galaxy population: the Tully-Fisher, cold gas fraction/stellar mass and cold gas metallicity/stellar mass relations for Sb/c spirals (Fig. 6.6); the field galaxy luminosity functions (Fig. 6.8 & 6.11); the colour-magnitude distribution of galaxies (Fig. 6.9); and the increase in mean stellar age with galaxy mass (Fig. 6.10). In addition the model produces a global star formation history in reasonable agreement with observation (Fig. 6.5). We also show in Springel et al. (2005) that the $z = 0$

clustering properties of this population are in good agreement with observations.

(iii) Our black hole implementation extends the previous work of Kauffmann & Haehnelt (2000) by assuming three modes of AGN growth: merger-driven accretion of cold disk gas in a 'quasar mode', merging between black holes, and 'radio mode' accretion when a massive black hole finds itself at the centre of a static hot gas halo. The 'quasar mode' is the dominant source for new black hole mass and is most active between redshifts of four and two. The 'radio mode' grows in overall importance until $z=0$ and is responsible for the feedback which shuts off the gas supply in cooling flows. This model reproduces the black hole mass/bulge mass relation observed in local galaxies (Fig. 6.4). The global history of accretion in the 'quasar mode' is qualitatively consistent with the evolution inferred from the optical AGN population (Fig. 6.3).

(iv) Although the overall accretion rate is low, 'radio mode' outflows can efficiently suppress condensation in massive systems (Fig. 6.7). As noted by many authors who have studied the problem in more detail than we do, this provides an energetically feasible solution to the long-standing cooling flow 'problem'. Our analysis shows that the resulting suppression of gas condensation and star formation can produce luminosity functions with very similar bright end cut-offs to those observed (Fig. 6.8), as well as colour-magnitude distributions in which the most massive galaxies are red and old, as observed, rather than blue and young (Figs 6.9 and 6.10).

(v) The $B-V$ colour distribution of galaxies is bi-modal at all galaxy masses. Galaxies with early-type bulge-to-disk ratios are confined to the red sequence, as are the most massive galaxies, and the most massive galaxies are almost all bulge-dominated, as observed in the real universe (Fig. 6.9). This bi-modality provides a natural division of model galaxies into red and blue subpopulations. The colour-dependent luminosity functions are qualitatively similar to those found for early and late-type galaxies in the 2dFGRS (Fig. 6.11), although there are significant discrepancies. After exhausting their cold gas, massive central galaxies grow on the red sequence through 'burstless' merging, gaining a factor of two or three in mass without significant star formation i(Bell et al. 2005). Such hierarchical growth does not change a galaxy's colour significantly, moving it brightward almost parallel to the colour-magnitude relation.

(vi) We present two physical models for black hole accretion from cooling flow atmospheres. We suppose that this accretion is responsible for powering the radio outflows seen at the centre of almost all real cooling flows. The models differ in their as-

sumptions about how gas accretes from the inner regions of the cooling flow, where it is thermally unstable and dynamically collapsing. One assumes accretion of cold gas clouds if these come within the sphere of influence of the black hole, while the other assumes Bondi-like accretion from the residual diffuse hot gas component. The two models produce $z = 0$ galaxy populations similar both to that of our simple phenomenological model for 'radio mode' feedback and to the observed population (see Fig. 6.12). Our main results are thus not sensitive to the details of the assumed accretion models.

The presence of heating from a central AGN has long been suspected as the explanation for the apparent lack of the gas condensation in cluster cooling flows. We have shown that including a simple treatment of this process in galaxy formation models not only 'solves' the cooling flow problem, but also dramatically affects the properties of massive galaxies, inducing a cut-off similar to that observed at the bright end of the galaxy luminosity function, and bringing colours, morphologies and stellar ages into much better agreement with observation than is the case for models without such feedback. We will extend the work presented here in a companion paper, where we investigate the growth of supermassive black holes and the related AGN activity as a function of host galaxy properties out to high redshift. The catalogues of galaxies and supermasive black holes produced by our modelling machinery are also being used for a very wide range of projects related to understanding formation, evolution and clustering processes, as well as for interpreting observational samples.

# 7 Concluding remarks

In this thesis, we have used the local galaxy population to examine both the large-scale density field and the population of galaxies that live within it. This analysis was broken up into three sections. In the first half, Chapters 2, 3, and 4, we examined the higher order clustering properties of the two degree field galaxy redshift survey (2dFGRS) galaxy distribution. In Chapter 5, we proceeded to use the 2dFGRS to examine the luminosity distribution of galaxies in environments ranging from sparse voids to the densest clusters. Finally, in Chapter 6, we presented a model of galaxy formation which included AGN radio feedback and used this to study the suppression of cooling flows in massive cluster systems. With this, we could quantify the effect such cooling flow suppression has on the properties of the local galaxy population. We now summarise the results of this work and the future directions we plan to take it.

## 7.1 Summary of results

Our study of higher order galaxy clustering began in Chapter 2, where we used the Two Degree Field Galaxy Redshift Survey (2dFGRS) to measure the higher order clustering moments of the local $L_*$ galaxy population. This volume limited sample contained a total of 44,931 galaxies within the magnitude range $-19 > M_{b_J} - 5\log_{10} h > -20$ and survey volume defined by $0.02 < z < 0.13$. Our aim was to test whether the $p$-point galaxy correlation functions, $\bar{\xi}_p$, can be written in terms of the two point correlation function or variance, $\bar{\xi}_p = S_p \, \bar{\xi}_2^{p-1}$, for some appropriate hierarchical scaling constants $S_p$. This is the so-called hierarchical scaling hypothesis and is expected if an initially Gaussian distribution of density fluctuations evolves under the action of gravitational instability. We showed that hierarchical scaling is obeyed in the 2dFGRS $L_*$ sample up to order 6 (Fig. 3.4), which is the limit to which we can measure the higher order moments with statistical significance. For all cell radii considered, $0.3 < R\,(h^{-1}\mathrm{Mpc}) < 30$, the measured variance was found to be in excellent agreement with the predictions from a $\Lambda$CDM N-body simulation (Fig. 3.2). However, the higher order correlation functions of $L_*$ galaxies have a significantly smaller amplitude than is predicted for the dark matter on scales $R < 10 h^{-1}\mathrm{Mpc}$. This implies that a non-linear bias exists between the dark matter and $L_*$ galaxies on these scales (see also Chapter 3). Finally, in this chapter we showed that the presence of two rare, massive superclusters in the 2dFGRS (Fig. 3.1) has an impact on the higher order clustering moments of the $L_*$ galaxy population measured on large scales (Fig. 3.3).

In Chapter 3, we extended this analysis by measuring the higher order moments of the 2dFGRS galaxy distribution as a function of galaxy luminosity. We had the full 2dFGRS available, approximately 200,000 galaxies, and constructed volume limited samples covering the magnitude range $-17 > M_{b_J} - 5\log_{10} h > -22$ in one magnitude width bins. Together, these volume limited catalogues allowed us to probe the universe out to scales of $z \approx 0.3$ ($\sim 750 h^{-1}$Mpc). We showed that, in an extension to the results of Chapter 2, galaxies of *all* luminosities obey hierarchical scaling, up to $6^{\text{th}}$ order (Fig. 3.5). This behaviour was found to hold on scales ranging from those where the underlying density fluctuations have become strongly nonlinear all the way through to the quasi-linear regime. The hierarchical amplitudes, $S_p = \bar{\xi}_p / \bar{\xi}_2^{p-1}$, were measured to be approximately independent of the cell radius used to smooth the galaxy distribution on small to medium scales (Fig. 3.6). On larger scales we found that the higher order moments could be strongly affected by the presence of the two massive superstructures in the galaxy distribution (Fig. 3.8 and 3.9), as found for the $L_*$ sample in Chapter 2. By tracking the evolution of $S_3$ across different volume limited samples, we showed that the skewness has a weak dependence on luminosity, which we approximated by a linear dependence on log luminosity (Fig. 3.10). The higher order $S_p$'s also suggested a similar luminosity dependence, but we unfortunately lacked the statistics across the full magnitude range to demonstrate this definitively. We discussed the implications of our results for simple models of linear and non-linear bias that relate the galaxy distribution to the underlying mass. A simple linear biasing model was shown to be an inadequate description of the higher order results, suggesting that non-linear biasing is present in the clustering moments of the 2dFGRS galaxy distribution (Fig. 3.10). The results of this chapter generalise those found in Chapter 2.

Chapter 4 was the final chapter in our study of higher order clustering in the 2dFGRS. Here we measured the reduced void probability function (VPF) for the same volume limited galaxy samples from Chapter 3, covering the absolute magnitude range $M_{b_J} - 5\log_{10} h = -18$ to $-22$. This statistic is valuable because, theoretically, the VPF connects the distribution of voids to the moments of galaxy clustering of *all* orders. It provides a different measure of hierarchical scaling: when plotting the reduced VPF against the scaling variable $\bar{N}\bar{\xi}$, all volume limited samples, containing galaxies of different magnitudes, mean number densities, and clustering amplitude, should all fall onto a common curve if hierarchical scaling exists in the moments of the galaxy probability distribution function (PDF). In addition, different hierarchical models of galaxy clustering (i.e. hierarchical PDFs) make different predictions for the reduced VPF (Fig. 4.1), and our measurement allowed us to discriminate between these. Reassuringly, the reduced VPF measured from the 2dFGRS was found to be in excellent agreement with the paradigm of hierarchical scaling of the galaxy clustering moments (Fig. 4.3), consistent with the results of the previous two chapters. The accuracy of our measurement was such that we can now rule out, at a very high significance, many popular models for galaxy clustering, including the lognormal distribution. We demonstrated that the negative binomial model gives a very good approximation to the 2dFGRS data over a wide range of scales, out to at least $20 h^{-1}$Mpc (Fig. 4.4). Conversely, the reduced VPF for dark matter in a $\Lambda$CDM universe does appear to be lognormal on small scales but was seen to deviate significantly beyond $\sim 4 h^{-1}$Mpc.

We found little dependence of the 2dFGRS reduced VPF on galaxy luminosity. We saw that the results of this chapter had an added robustness in that the reduced VPF is not sensitive to the two massive superclusters in the survey volume which were seen to so significantly affect the larger-scale higher order measurements in Chapters 2 and 3. This is because the reduced VPF more favourably weights the low and intermediate counts in the PDF and not the tail where the rare high density peaks are seen. Finally, because the 2dF-GRS contains inherent spectroscopic incompleteness, corrections were needed for missed galaxies when undertaking the counts-in-cells analysis. Since weighting galaxy *counts* will no longer work (how does one weight no galaxies?), we developed a new *volume* weighting technique to account for this. Using mock catalogues, we demonstrated that our method effectively corrects spectroscopic incompleteness in the cell counts on all scales that were considered.

In summary, Chapters 2 and 3 demonstrated to high significance that the clustering moments of the 2dFGRS galaxy PDF are hierarchical, implying that the initial matter density field, from which the present day structure evolved, is Gaussian. Chapter 4 used this behaviour to place constraints on the "actual" hierarchical model of galaxy clustering, of which there are currently many in the literature. We showed that the negative binomial model provides a remarkably good fit to the scaling behaviour of the local redshift space galaxy distribution and ruled out all other clustering models at a high statistical significance. Unfortunately, there is currently no adequate physical motivation for the negative binomial model (but see Section 7.2 below).

In Chapter 5, we shifted our focus to now use the 2dFGRS to measure the dependence of the $b_J$-band galaxy luminosity function on large-scale environment. This was defined by density contrast in spheres of radius $8h^{-1}$Mpc, and on spectral type, determined from principal component analysis. To obtain both luminosity function shapes *and* normalisations we developed a new hybrid step-wise maximum likelihood/count-in-cells technique and showed that this accurately reproduced existing field, cluster, and spectral type published luminosity functions (Fig. 5.1). The galaxy populations identified in environments at both extremes of density were found to differ significantly from that at the mean density (Fig. 5.3 and 5.4). The population in voids is dominated by late types and shows, relative to the mean, a deficit of galaxies that becomes increasingly pronounced at magnitudes brighter than $M_{b_J} - 5\log_{10} h \lesssim -18.5$. In contrast, cluster regions have a relative excess of very bright early-type galaxies with $M_{b_J} - 5\log_{10} h \lesssim -21$. Differences in the mid to faint-end population between environments were significant: at $M_{b_J} - 5\log_{10} h = -18$ early and late-type cluster galaxies show comparable abundances, whereas in voids the late types dominated by almost an order of magnitude (Fig. 5.5). We found that the luminosity functions measured in all density environments, from voids to clusters, could be approximated by Schechter functions, with parameters that varied smoothly with local density, but in a fashion that differed strikingly for early and late-type galaxies (Fig. 5.6 and 5.7). Of interest to many galaxy formation models is our measurement that reveals that the faint-end slope of the overall luminosity function depends at most weakly on density environment. Our measurements of the luminosity function in different density environments are now being used for many different purposes, from constraining the statistics of halo occupation

models (Mo et al. 2004) to studying the detailed formation histories of truly isolated void galaxies in the local universe.

Finally, in Chapter 6, we extend our analysis of the local galaxy population by developing a self consistent model of galaxy formation, which we coupled to the Millennium Run ΛCDM N-body simulation. The resolution of the Millennium Run is such that the detailed assembly history of each object in the simulation, as faint as galaxy luminosities approximately equal to the Small Magellanic Cloud, is accurately followed in a volume comparable to that of the 2dFGRS. In our galaxy formation model we supplemented previous treatments of the growth and activity of central black holes with a new model for 'radio' feedback from those AGN that lie at the centre of a quasistatic X-ray emitting atmosphere in a galaxy group or cluster. This AGN feedback mechanism was implemented to suppress the inflow of cooling gas out of such hot atmospheres. Our main results are important to an understanding of how galaxies form and evolve. With this model we showed that one could simultaneously explain (i) the low observed mass drop-out rate in cooling flows, (ii) the exponential cut-off at the bright end of the galaxy luminosity function, and (iii) the fact that the most massive galaxies tend to be bulge-dominated systems in clusters and to contain systematically older stars than lower mass galaxies. This success occurs because static hot atmospheres form only in the most massive structures, and radio feedback (in contrast, for example, to supernova or starburst feedback) can suppress further cooling and thus star formation without itself requiring star formation. We finished Chapter 6 with a discussion of some physical models for black hole accretion which may explain the phenomenology required for our model to be successful.

## 7.2 Future work

This thesis suggests several directions for future research that will complement and extend what has been already been achieved. Such programs are either currently proposed or currently underway, which we will now describe.

### Galaxy clustering

Chapters 2, 3, and 4 measured the higher order clustering of galaxies in the 2dFGRS. This work is currently being extended in three ways. First, we have recently submitted for publication in the Monthly Notices of the Royal Astronomical Society an analysis of the 2dFGRS 3-point galaxy correlation function for the full catalogue and also when split by luminosity and colour (Gaztañaga et al. 2005). Our primary result from this work is that we demonstrate the first statistically significant measurement of galaxy–dark matter non-linear bias, which is found to be non-zero at a $3\sigma$ level.

Second, we have repeated the analysis of Chapters 2, 3 and 4 for sub-populations of each volume limited sample split by $b_J$-$r_F$ galaxy colour. This allows us to investigate the hierarchical nature of early and late-type galaxy populations independently. These new measurements show that the hierarchical amplitudes and both linear and non-linear bias

parameters of red and blue galaxies behave differently and in an unexpected way. Our results are now being written up for publication (Croton et al. 2005, in preparation).

Third, in the near future we plan to investigate both the low and higher order clustering properties of the semi-analytic model galaxy population described in Chapter 6. Here the aim is to use the moments of the galaxy distribution to constrain various aspects of the galaxy formation physics. For example, recent results from the DEEP2 Team suggest that the lowest order clustering properties of galaxies were already in place at $z \sim 1$ and have changed little up to the present day. However, the higher-order clustering may not be so insensitive, and the evolution of specific galaxy properties between $z = 1$ and $0$ may leave a signature in the higher order moments of selected sub-populations that can be measured. If so, models of galaxy formation could be used to identify the physical process (i.e. star formation efficiency, supernova feedback, reionization, etc.) that produce this signature. The identification of such would be vastly useful and allow researchers to use the spatial distribution of a sample of galaxies to indirectly measure physical events which may otherwise be impossible to observe.

### "Void" galaxies

Chapter 5 investigated the environmental dependence of the galaxy luminosity function in the 2dFGRS. We look to extend this work in the near future in both observational and theoretical directions. We have currently secured Hubble Space Telescope time for 10 orbits during cycle 14 to undertake V and I-band deep imaging of selected early-type extreme-void galaxies ($\delta_8 < -0.9$), identified using the 2dFGRS sample described in Chapter 5. We expect to derive the isophotal shape of each galaxy and resolve their sub-components (disks, dust lanes, star-forming regions, etc.) which will provide insight into their formation histories. These observations will be complemented with detailed modelling of mock void galaxy populations using the galaxy formation model described in Chapter 6. By tuning the model to match key observations, the explicit history of each mock void galaxy can be traced from high redshift to the present. In this way, events in the history of each galaxy which lead to a particular observational end can be isolated and studied in detail.

### Galaxy formation modelling

Finally, the galaxy formation modelling undertaken in Chapter 6 opens up many future research directions. We summarise only the most interesting here but point out that this model, in conjunction with the Millennium Run simulation, is currently being used for a number of diverse projects by researchers both at the Max Planck Institute for Astrophysics and in other institutions globally.

First, using our semi-analytic model galaxy population, we have investigated the black hole mass–bulge mass relation and its possible evolution with redshift. This work has been written up for publication (Croton & White 2005, in preparation). We show in this paper that if mergers are the primary drivers for both black hole and bulge growth (which is the the current assumption in most simple models of galaxy formation), then disrupted

disks can drive evolution in $m_{\mathrm{BH}}$–$m_{\mathrm{bulge}}$. This effect may be seen in future high redshift observations.

Second, recent results by Gao et al. (2005) have demonstrated that a fundamental assumption in current halo occupation models (e.g. Cooray & Sheth 2002) may be wrong. This assumption is that the mass of a dark matter halo alone determines the properties of the galaxies that lie inside it. Gao et al. showed that low mass halos which form at early epochs cluster differently from those that form at latter times, even when at redshift zero their virial masses are identical. If correct, this behaviour should also be seen in the galaxy population. Initial results using the galaxy formation model and Millennium Run simulation described in Chapter 6 reveal that this is indeed the case. We are now looking into this property of the galaxy population in greater detail. Such tests are important given the current popularity of the the halo occupation methodology.

# Acknowledgements

So this thesis is finally finished, but funnily I feel like I've just begun! However I certainly didn't get here alone, so now is my chance to show my appreciation to all those who have helped me along the way, in one way or another.

First, I have to acknowledge those who probably don't get acknowledged as much as they should, although we'd all be lost without them! Kate O'Shea, Maria Depner, Cornelia Rickl, Gabi Kratschmann, and everyone "down below" in personnel - you were all way more organised than I was, and I can't tell you how much I appreciated that. And for all your help, smiles, and patience with this clumsy auslander. It really helped! Also, I can't go on without thanking Bernt Christandl, Hans-Werner Paulsen, Norbert Gruener, and all those in computational support at MPA. Sorry I kept forgetting to bring the new mac G4 powerbook back. I *swear* I meant to!

I would like to take this opportunity to express my appreciation to the directors of the International Max Planck Research School on Astrophysics, and also its administrator, Werner Becker. I think you have set up a wonderful program and I have benefited enormously from the hard work you have all put in. In addition, much of my time so far has been spent analysing observational data taken as part of the Two Degree Field Galaxy Redshift Survey (Chapters 2–5). I would like to acknowledge the efforts of all those responsible for the smooth running of the survey, and for the opportunity to have access to such a fantastic data set. It was a real privilege. This also goes for those involved in the Virgo Supercomputing Consortium, through whom the Millennium Run simulation was undertaken at the Computing Centre of the Max-Planck Society in Garching. I am most appreciative to have had access to such state-of-the-art science, and without which much of my work in Chapter 6 (and ongoing) would not have been possible.

There has been no single person so far from whom I've learnt more than my supervisor, Simon White. This is actually a significant understatement, as much of what I've picked up can't be formulated through equations, or written in scientific journals. It's as much about the *approach* and *attitude* to research as it is to the end results themselves, about finding new ideas and seeing connections between seemly disconnected things. As Amina Helmi once said to me, the great (and hard!) thing about working with Simon is that he sets such a high standard. Interestingly, after a while this has just become normal. Simon, thank you for instilling it in me! And thank you for giving me the space to find my own path – I hope it hasn't deviated too far from where you would have wanted me to end up! It really has been the most amazing experience to have been able to work with you.

To my collaborators, whom I now consider just as much friends as I do colleagues: Carlton Baugh, the gentle giant! Your knowledge of beer rivals your knowledge of astronomy, it seems! You are a huge asset to the group at Durham, and you really looked after me every time I visited – I appreciated that and won't forget it. In many ways, early on, both you and Enrique became "second supervisors" for me, and I learnt so much from just watching how you both worked. Thanks for thinking of me every time Australia lost to England in the cricket or rugby! Enrique Gaztañaga, your experience and direction were invaluable. You taught me more about statistics than I think I could write in a book! It was great to have someone share my excitement with about the negative binomial model, whether or not in the end it turns out to be interesting (still may be!). Thanks for a wonderful time in Barcelona – I think I would be very happy retiring there! Peder Norberg, you taught me the value of appendices! I learnt so much from your attention to detail, and I really appreciated how hard you worked when we needed fast results. Thanks for introducing me to the "Kings Cave". Discretionary chips will never be the same! Glennys Farrar, your encouragement with our luminosity function project was a real inspiration. You really got me thinking outside my normal boundaries. Thanks for so wonderfully looking after Linda and I in New York – we had a great time, both exploring the city and at NYU. Volker Springel, you do amazing science which always blows me away, and are continually pushing forward what is considered state-of-the-art. This is exciting to be a part of! Thank you for many words of wisdom, and also for the wonderful movies!

In addition to my collaborators above, I also want to thank those people who have, with overwhelming generosity and patience, taken the time to help me along the way, including much advice and guidance. Thanks to Frank van den Bosch, Saleem Zaroubi, Guinevere Kauffmann, Eugene Churazov, Andrea Merloni, Greg Rudnick, Amina Helmi, John Peacock, Ofer Lahav and Carlos Frenk. Many people also played a big part directing my progress in science in my early years, and the fact that I've made it this far is just as much a testament to them as it is to anything I've done so far: Craig Savage, Paul Francis, Brian Schmidt, Joel Primack, Matthew Colless – I haven't forgotten the lessons you taught me! Thanks to my friends and colleagues here at MPA who, though beer and conversation, helped keep me sane! Jorge Cuadra-Stipetich, Tess Jaffe, Felix Stoehr, Gabriella De Lucia, Gao Liang, Manfred Kitzbichler, Eric Hayashi, Jeremy Blaizot, Brent Groves, Christoph Pfrommer and Mike Revnivtsev.

Finally, to my family, both old and new. Mum and Dad, this is all only possible because you've given me so much. I couldn't have made it this far without your 34 years of unconditional love and support. This thesis is dedicated to my beautiful wife. Linda, you inspire me more than you'll ever know. I love you more than life itself. :-*

# Bibliography

Arav N., de Kool M., Korista K. T., et al., 2001, ApJ, 561, 118

Bagla J. S., 2002, Journal of Astrophysics and Astronomy, 23, 185

Balbus S. A., Soker N., 1989, ApJ, 341, 611

Baldry I. K., Glazebrook K., Brinkmann J., et al., 2004, ApJ, 600, 681

Balian R., Schaeffer R., 1989, A&A, 220, 1

Barnes J., Hut P., 1986, Nature, 324, 446

Baugh C. M., Gaztañaga E., Efstathiou G., 1995, MNRAS, 274, 1049

Baugh C. M., Croton D. J., Gaztañaga E., et al. (the 2dFGRS team), 2004, MNRAS, 351, L44

Begelman M., de Kool M., Sikora M., 1991, ApJ, 382, 416

Bell E. F., Naab T., McIntosh D. H., et al., 2005, MNRAS, submited, astro-ph/0506425

Benoist C., Cappi A., Da Costa L. N., Maurogordato, S., Bouchet F., Schaeffer R., 1999, ApJ, 514, 563

Benson A. J., Cole S., Frenk C. S., Baugh C. M., Lacey C. G., 2000, MNRAS, 311, 793

Benson A. J., Frenk C. S., Baugh C. M., Cole S., Baugh Lacey C. G., 2001, MNRAS, 327, 1041.

Benson A. J., Frenk C. S., Lacey C. G., Baugh C. M., Cole S., 2002, MNRAS, 333, 177

Benson A. J., Bower R. G., Frenk C. S., Lacey C. G., Baugh C. M., Cole S., 2003, ApJ, 599, 38

Benson A. J., Hoyle F., Torres F., Vogeley M. S., 2003, MNRAS, 340, 160

Berlind A. A., Weinberg D. H., Benson A. J., Baugh C. M., Cole S., Davé R., Frenk C. S., Jenkins A., Katz N., Lacey C. G., 2003, ApJ, 593, 1

Bernardeau F., 1994, A&A, 291, 697

Bernardeau F., Colombi S., Gaztañaga E., Scoccimarro R., 2002, Phys. Rep., 367, 1

Bernstein G. M., 1994, ApJ, 424, 569

Bertschinger E., 1989, ApJ, 340, 666

Binney J., 1977, ApJ, 215, 483

Binney J., Tabor G., 1995, MNRAS, 276, 663

Binney J., Tremaine S., 1987, *Galactic dynamics* (Princeton) University Press, 1987, 747 p.

Birnboim Y., Dekel A., 2003, MNRAS, 345, 349

Blanton M. R., Hogg D. W., Bahcall N. A., et al. (SDSS team), 2003a, ApJ, 592, 819

Blanton M. R., Hogg D. W., Bahcall N. A., et al. (SDSS team), 2003b, ApJ, 594, 186

Bode P., Ostriker J. P., Xu G., 2000, ApJS, 128, 561

Bondi H., 1952, MNRAS, 112, 195

Bonometto S. A., Borgani S., Ghigna S., Klypin A., Primack J. R. 1995, MNRAS, 273, 101

Bouchet F. R., Strauss M. A., Davis M., Fisher K. B., Yahil A., Huchra J.P., 1993, ApJ, 417, 36

Bromley B. C., Press W. H., Lin H., Kirshner R. P., 1998, ApJ, 505, 25

Brüggen M., Kaiser C. R., 2002, Nature, 418, 301

Bruzual A. G., Charlot S., 1993, ApJ, 405, 538

Bullock J. S., Dekel A., Kolatt T. S., et al., 2001, ApJ, 555, 240

Burns J. O., Gregory S. A., Holman G. D., 1981, ApJ, 250, 450

Chartas G., Brandt W. N., Gallagher S. C., 2003, ApJ, 595, 85

Christlein D., 2000, ApJ, 545, 145

Churazov E., Sunyaev R., Forman W., Böhringer H., 2002, MNRAS, 332, 729

Cole S., Kaiser N., 1989, MNRAS, 237, 1127.

Cole S., Hatton S., Weinberg D. H., Frenk C. S., 1998, MNRAS, 300, 945

Cole S., Lacey C. G., Baugh C. M., Frenk C. S., 2000, MNRAS, 319, 168

Cole S., Norberg P., Baugh C. M., et al., 2001, MNRAS, 326, 255

Cole S., et al., 2005, MNRAS, submitted, astro-ph/0501174

Coles P., Jones B., 1991, MNRAS, 248, 1

Coles P., Lucchin F., 1995, *Cosmology. The origin and evolution of cosmic structure* (Wiley)

Colombi S., Bouchet F. R., & Schaeffer R., 1994, A&A, 281, 301

Colless M., Dalton G., Maddox S., et al. (the 2dFGRS team), 2001, MNRAS, 328, 1039

Colless M., Peterson B. A, Jackson C, et al. (the 2dFGRS team), 2003, astro-ph/0306581

Conway E., Maddox S., Wild V., et al. (the 2dFGRS team), 2005, MNRAS, 356, 456

Cooray A., Sheth R., 2002, PhR, 372, 1

Cowie L. L., Binney J., 1977, ApJ, 215, 723

Cowie L. L., Fabian A. C., Nulsen P. E. J., 1980, MNRAS, 191, 399

Cowie L. L., Songaila A., Hu E. M., Cohen J. G., 1996, AJ, 112, 839

Cox T. J., Primack J., Jonsson P., Somerville R. S., 2004, ApJL, 607, L87

Crenshaw D. M., Kraemer S. B., George I. M., 2003, ARA&A, 41, 117

Croton D. J., Colless M., Gaztañaga E., et al. (the 2dFGRS team), 2004a, MNRAS, 352, 828

Croton D. J., Gaztañaga E., Baugh C. M., et al. (the 2dFGRS team), 2004b, MNRAS, 352, 1232

Cooray A., Sheth R., 2002, Phys.Rep. 372, 1

Curruthers P., Minn D. V., 1983, Phys. Lett. B, 131, 116

Curruthers P., Shih C. C., 1983, Phys. Lett. B, 127, 242

Davis M., Peebles P. J. E., 1983, ApJ, 267, 465

Davis M., Efstathiou G., Frenk C. S., White S. D. M., 1985, ApJ, 292, 371

Davis M., Meiksin A., Strauss M. A., da Costa L. N., Yahil A., 1988, ApJ, 333, L9

de Kool M., Arav N., Becker R. H., et al., 2001, ApJ, 548, 609

De Lucia G., Kauffmann G., White S. D. M., 2004, MNRAS, 349, 1101

De Propris R., Colless M., Driver S.P., et al. (2dFGRS team), 2003, MNRAS, 342, 725

Di Matteo T., Springel V., Hernquist L., 2005, Nature, 433, 604

Dressler A., 1980, ApJ, 236, 351

Edgar R., 2004, New Astronomy Review, 48, 843

Efstathiou G., Ellis R. S., Peterson B. A., 1988, MNRAS, 232, 431

Efstathiou G., Kaiser N., Saunders W., Lawrence A., Rowan-Robinson M., Ellis R. S., Frenk C. S., 1990, MNRAS, 247, 10P

Efstathiou G., 1992, MNRAS, 256, 43P

Einasto J., Hütsi G., Einasto M., Saar E., Tucker D. L., Müller V., Heinämäki P., & Allam S. S., 2003a, AAP, 405, 425

Einasto J., et al., 2003b, AAP, 410, 425

Eke V. R., Baugh C. M., Cole S., et al. (the 2dFGRS team), 2004, MNRAS, 348, 866

Elizalde E., Gaztãnaga E., 1992, MNRAS, 254, 247

Erdoğdu P., Lahav O., Zaroubi S., et al. (the 2dFGRS team), 2004, MNRAS, 352, 939

Evrard A. E., MacFarland T. J., Couchman H. M. P., et al. (the Virgo Consortium), 2002, ApJ, 573, 7

Fabian A. C., Nulsen P. E. J., 1977, MNRAS, 180, 479

Fabian A. C., Sanders J. S., Allen S. W., et al., 2003, MNRAS, 344, L43

Fan X., Narayanan V. K., Lupton R. H., et al., 2001, AJ, 122, 2833

Feldman, H. A, Frieman, J. A., Fry, J. N., Scoccimarro R., 2001, Phys. Rev. Lett., 86, 1434

Fisher K. B., Davis M., Strauss M. A., Yahil A., Huchra J. 1994, MNRAS, 266, 50

Flores R. A., Primack J. R., 1994, ApJ, 427, L1

Folkes S., Ronen S., Price I., et al. (2dFGRS team), 1999, MNRAS, 308, 459

Forcada-Miró M. I., White S. D. M., 1997, astro-ph/9712204

Fosalba P., Gaztañaga E., 1998, MNRAS, 301, 503

Freeman K. C., 1970, ApJ, 160, 811

Frieman J. A. & Gaztañaga E., 1999, ApJ, 521, L83

Fry, J. N., 1984, ApJ Let, 277, L5

Fry J. N., 1986, ApJ, 306, 358

Fry J. N., Giovanelli R., Haynes M. P., Melott A. L., Scherrer R. J., 1989, ApJ, 340, 11

Fry J. N., Gaztañaga E., 1993, ApJ, 413, 447

Fry J. N., Gaztañaga E., 1994, ApJ, 425, 1

Gao L., Springel V., White S. D. M., 2005, MNRAS, submitted, astro-ph/0506510

Garnett D. R., 2002, ApJ, 581, 1019

Gaztañaga E., 1992, ApJ, 398, L17

Gaztañaga E., Yokoyama J., 1993, ApJ, 403, 450

Gaztañaga E., 1994, MNRAS, 268, 913

Gaztañaga E., Frieman J., 1994, ApJ, 437, L13

Gaztañaga E., Baugh C. M., 1995, MNRAS, 273, L1

Gaztañaga E., Mahonen P., 1996, ApJ, 462, L1.

Gaztañaga E., Fosalba P., 1998, MNRAS, 301, 524

Gaztañaga E., Bernardeau F., 1998, A.& A., 331, 829

Gaztañaga E., Fosalba P., Elizalde E., 2000 ApJ, 539, 522

Gaztañaga E., Juszkiewicz R., 2001, ApJ, 558, L1

Gaztañaga E., 2002, ApJ, 580, 144

Gaztañaga E., Wagg J., 2003, Phys.Rev.D, 68, 21302

Gaztañaga E., Norberg P., Baugh C. M., Croton D. J., 2005, MNRAS, submitted, astro-ph/0506249

Ghigna S., Bonometto S. A., Guzzo L., Giovanello R., Haynes M. P., Klypin A., Primack J. R., 1996, ApJ, 463, 395

Ghigna S., Moore B., Governato F., Lake G., Quinn T., Stadel J., 1998, MNRAS, 300, 146

Giovanelli R., Haynes M. P., da Costa L. N., Freudling W., Salzer J. J., Wegner G., 1997, ApJL, 477, L1+

Gnedin N. Y., 2000, ApJ, 542, 535

Goldberg D. M., Jones T. D., Hoyle F., Rojas R. R., Vogeley M. S., Blanton M. R., 2005, ApJ, 621, 643

Gonzalez R. E., Lares M., Lambas D. G., Valotto C., 2005, A&A, submitted, astro-ph/0507144

Groth E. J., Peebles, P. J. E., 1977, ApJ, 217, 385

Häring N., Rix H., 2004, ApJL, 604, L89

Hartwick F. D. A., Schade D., 1990, ARA&A, 28, 437

Hatton S., Devriendt J. E. G., Ninin S., Bouchet F. R., Guiderdoni B., Vibert D., 2003, MNRAS, 343, 75

Hawkins E., Maddox S., Cole S., et al. (the 2dFGRS team), 2003, MNRAS, 346, 78

Heavens A., Panter B., Jimenez R., Dunlop J., 2004, Nature, 428, 625

Heckman T. M., Armus L., Miley G. K., 1990, ApJS, 74, 833

Helly J. C., Cole S., Frenk C. S., et al., 2003, MNRAS, 338, 913

Hinshaw G., Spergel D. N., Verde L., et al. (the WMAP team), 2003, ApJS, 148, 135

Hivon E., Bouchet F. R., Colombi S., Juszkiewicz R., 1995, Astron. & Astroph., 298, 643

Hockney R. W., Eastwood J. W., 1981, Computer Simulation Using Particles, New York: McGraw-Hill, 1981

Hogg D. W., Blanton M. R., Eisenstein D. J., et al. (SDSS team), 2003, ApJL, 585, L5

Hoyle F., Szapudi I., Baugh C. M., 2000, MNRAS, 317, L51

Hoyle F., Vogeley M. S., 2004, ApJ, 607, 751

Hoyle F., Rojas R. R., Vogeley M. S., Brinkmann J., 2005, ApJ, 620, 618

Huang J.-S., Glazebrook K., Cowie L. L., Tinney C., 2003, ApJ, 584, 203

Hui L., Gaztañaga E., 1999, ApJ, 519, 622

Hütsi G., Einasto J., Tucker D. L., Saar E., Einasto M., Müller V., Heinämäki P., Allam S. S., 2003, A&A, submitted, astro-ph/0212327

Juszkiewicz R., Bouchet F. R., Colombi S., 1993, ApJ, 412, L9

Kaiser C. R., Binney J., 2003, MNRAS, 338, 837

Kaiser N., 1984, ApJ, 284, L9

Kamionkowski M., Kowsowsky A., 1999, Ann. Rev. Nuclear & Particle Science, 49, 77.

Kauffmann G., White S. D. M., Guiderdoni B., 1993, MNRAS, 264, 201

Kauffmann G., 1996, MNRAS, 281, 475

Kauffmann G., Colberg J. M., Diaferio A., White S. D. M., 1999, MNRAS, 303, 188

Kauffmann G., Haehnelt M., 2000, MNRAS, 311, 576

Kauffmann G., Heckman T. M., White S. D. M., et al., 2003, MNRAS, 341, 54

Kauffmann G., White S. D. M., Heckman T. M., Ménard B., Brinchmann J., Charlot S., Tremonti C., Brinkmann J., 2004, MNRAS, 353, 713

Kennicutt R. C., 1998, ApJ, 498, 541

Keres D., Katz N., Weinberg D. H., Dave R., 2004, MNRAS, submited, astro-ph/0407095

Klauder J. R., Sudarshan E. C. G., 1968, *Fundamentals of Quantum Optics* (New York: Benjamin)

Komatsu E., et al. 2003, ApJS, 148, 119

Kormendy J., 1982, in *Morphology and Dynamics of Galaxies*

Kravtsov A. V., Gnedin O. Y., Klypin A. A., 2004, ApJ, 609, 482

Kuo C. L., Ade P. A. R., Bock J. J., et al. (the ACBAR team), 2004, ApJ, 600, 32

Lacey C., Cole S., 1993, MNRAS, 262, 627

Lahav O., Itoh M., Inagaki S., Suto Y., 1993, ApJ, 402, 387

Lahav O., Bridle S. L., Percival W. J., et al. (the 2dFGRS team), 2002, MNRAS, 333, 961

Lin H., Yee H. K. C., Carlberg R. G., Ellingson E., 1996, BAAS, 28, 1412

Longair M. S., 1998, *Galaxy Formation* (Springer)

Loveday J., Peterson B. A., Efstathiou G., Maddox S. J., 1992, ApJ, 390, 338

Loveday J., Maddox S. J., Efstathiou G., Peterson B. A., 1995, ApJ, 442, 457

Madau P., Ferguson H. C., Dickinson M. E., Giavalisco M., Steidel C. C., Fruchter A., 1996, MNRAS, 283, 1388

Maddox S. J., Efstathiou G., Sutherland W. J., Sutherland W. J., 1990, MNRAS, 246, 433

Maddox S. J., Efstathiou G., Sutherland W. J., 1996, MNRAS, 283, 1227

Madgwick D. S., Lahav O., Baldry I. K., et al. (2dFGRS team), 2002, MNRAS, 333, 133

Magorrian J., Tremaine S., Richstone D., et al., 1998, AJ, 115, 2285

Mandelbaum R., McDonald P., Seljak U., Cen R., 2003, MNRAS, 344, 776

Marconi A., Hunt L. K., 2003, ApJL, 589, L21

Martin C. L., 1999, ApJ, 513, 156

Marzke R. O., Huchra J. P., Geller M. J., 1994, ApJ, 428, 43

Mason B. S., et al. (the CBI team), 2003, ApJ, 591, 540

Mathis H., White S. D. M., 2002, MNRAS, 337, 1193

Maurogordato S., Lachieze-Rey M., 1987, ApJ, 320, 13

McGaugh S. S., Schombert J. M., Bothun G. D., de Blok W. J. G., 2000, ApJL, 533, L99

McNamara B. R., Nulsen P. E. J., Wise M. W., et al., 2005, Nature, 433, 45

McNamara B. R., Wise M., Nulsen P. E. J., et al., 2000, ApJL, 534, L135

Merloni A., 2004, MNRAS, 353, 1035

Mihos J. C., Hernquist L., 1994, ApJL, 425, L13

Mihos J. C., Hernquist L., 1996, ApJ, 464, 641

Mo H. J., White S. D. M., 1996, MNRAS, 282, 347

Mo H. J., Jing Y. P., White S. D. M., 1997, MNRAS, 284, 189

Mo H. J., Mao S., White S. D. M., 1998, MNRAS, 295, 319

Mo H. J., Yang X., van den Bosch F. C., Jing Y. P., 2004, MNRAS, 349, 205

Netterfield C. B., Ade P. A. R., Bock J. J., et al. (the BOOMERANG team), 2002, ApJ, 571, 604

Norberg P., Cole S., Baugh C. M., et al. (the 2dFGRS team), 2001, MNRAS, 328, 64

Norberg P., Baugh C. M., Hawkins E., et al. (the 2dFGRS team), 2002a, MNRAS, 332, 827

Norberg P., Baugh C. M., Hawkins E., et al. (the 2dFGRS team), 2002b, MNRAS, 336, 907

Nulsen P. E. J., 1986, MNRAS, 221, 377

Nulsen P. E. J., Fabian A. C., 2000, MNRAS, 311, 346

Olive K. A., Steigman G., Walker T. P., 2000, PhysRep, 333, 389

Omma H., Binney J., Bryan G., Slyz A., 2004, MNRAS, 348, 1105

Padilla N. D., Baugh C. M., 2003, MNRAS, 343, 796

Peacock J. A., Cole S., Norberg P., et al. (the 2dFGRS team), 2001, Nature, 410, 169

Peebles P. J. E., 1980, *The Large-Scale Structure of the Universe* (Princeton University Press)

Peebles P. J. E., 1993, *Principles of physical cosmology* (Princeton University Press)

Peebles P. J. E., 2001, ApJ, 557, 495

Percival W., Baugh C. M., Bland-Hawthorn J., et al. (the 2dFGRS team), 2001, MNRAS, 327, 1297

Percival W. J., Sutherland W., Peacock J. A., et al., 2002, MNRAS, 337, 1068

Perlmutter S., Aldering G., Goldhaber G., et al., 1999, ApJ, 517, 565

Peterson J. R., Paerels F. B. S., Kaastra J. S., et al., 2001, A&A, 365, L104

Popesso P., Biviano A., Böhringer H., Romaniello M., 2005, A&A, accepted, astro-ph/0506201

Porciani C., Giavaliso M., 2002, ApJ, 565, 24

Pounds K. A., Reeves J. N., King A. R., Page K. L., O'Brien P. T., Turner M. J. L., 2003, MNRAS, 345, 705

Press W. H., Schechter P., 1974, ApJ, 187, 425

Ratcliffe A., Shanks T., Parker Q. A., Fong R., 1998, MNRAS, 293, 197

Rees M. J., Ostriker J. P., 1977, MNRAS, 179, 541

Reeves J. N., O'Brien P. T., Ward M. J., 2003, ApJL, 593, L65

Riess A. G., et al., 1998, AJ, 116, 1009

Rojas R. R., Vogeley M. S., Hoyle F., Brinkmann J., 2004, ApJ, 617, 50

Rojas R. R., Vogeley M. S., Hoyle F., Brinkmann J., 2005, ApJ, 624, 571

Ruszkowski M., Begelman M. C., 2002, ApJ, 581, 223

Sandage A., Tammann G. A., Yahil A., 1979, ApJ, 232, 352

Sanders D. B., Mirabel I. F., 1996, ARA&A, 34, 749

Saslaw W. C., Hamilton A. J. S., 1984, ApJ, 276, 13

Saunders W., Frenk C.S., Rowan-Robinson M., Lawrence A., Efstathiou G., 1991, Nature, 349, 32

Schechter P., 1976, ApJ, 203, 297

Scoccimarro R., 2000, ApJ, 544, 597

Scoccimarro R., Sheth R., Hui L., Jain B., 2001, ApJ, 546, 20

Scoccimarro R., Sefusatti E., Zaldarriaga M., 2004, PhRvD, 69, 103513

Scott P. F., Carreira P., Cleary K., et al. (the VSA team), 2003, MNRAS, 341, 1076

Seljak U., Makarov A., McDonald P., et al., 2004, Phys Rev D, submitted, astro-ph/0407372

Seljak U., Zaldarriaga M., 1996, ApJ, 469, 437

Sersic J. L., 1968, *Atlas de Galaxias Australes*. Observatorio Astronómico, Córdoba.

Shaver P. A., Wall J. V., Kellermann K. I., Jackson C. A., Hawkins M. R. S., 1996, Nature, 384, 439

Silk J., 1977, ApJ, 211, 638

Smoot G. F., Gorenstein M. V., Muller R. A., 1977, PhRvL, 39, 898

Somerville R. S., Primack J. R., Faber S. M., 2001, MNRAS, 320, 504

Spergel D. N., Verde L., Peiris H. V., et al., 2003, ApJS, 148, 175

Springel V., Yoshida N., White S. D. M., 2001b, New Astronomy, 6, 79

Springel V., White S. D. M., Tormen G., Kauffmann G., 2001a, MNRAS, 328, 726

Springel V., Hernquist L., 2003a, MNRAS, 339, 289

Springel V., Hernquist L., 2003b, MNRAS, 339, 312

Springel V., et al., 2005, Nature, 435, 629

Springel V., 2005, MNRAS, submitted

Szapudi I., Dalton G. B., Efstathiou G., Szalay A. S., 1995, ApJ, 444, 520

Szapudi I., 1998, ApJ, 497, 16

Szapudi I., Gaztañaga E., 1998, MNRAS, 300, 493

Szapudi I., Quinn T., Stadel J., Lake G., 1999, ApJ, 517, 54

Szapudi I., Branchini E., Frenk C.S., Maddox S., Saunders W., 2000, MNRAS, 318, L45

Szapudi I., Frieman J. A., Scoccimarro R., et al. (the SDSS team) 2002, ApJ, 570, 75

Tabor G., Binney J., 1993, MNRAS, 263, 323

Tamura T., Kaastra J. S., Peterson J. R., et al., 2001, A&A, 365, L87

Tegmark M., Strauss M. A., Blanton M. R., et al. (the SDSS collaboration), 2004, PhRvD, 69, 10, 103501

Tegmark M., Blanton M. R., Strauss M. A., .et al. (the SDSS collaboration), 2004, ApJ, 606, 702

Thoul A. A., Weinberg D. H., 1995, ApJ, 442, 480

Tremonti C. A., Heckman T. M., Kauffmann G., et al., 2004, ApJ, 613, 898

Tully R. B., Somerville R. S., Trentham, N., Verheijen M. A. W., 2002, ApJ, 569, 573

van den Bergh S., 2000, *The galaxies of the Local Group* (Cambridge University Press)

Van Waerbeke L., Mellier Y., Pelló R., Pen U.-L., McCracken H. J., Jain B., 2002, A&A, 393, 369

Verde L., Heavens A. F., Percival W. J., et al. (the 2dFGRS team), 2002, MNRAS, 335, 432

Vogeley M. S., Geller M. J., Park C., Huchra J. P., 1994, ApJ, 108, 745

Weinberg D. H., Cole S., 1992, MNRAS, 259, 652

White S. D. M., Rees M. J., 1978, MNRAS, 183, 341

White S. D. M., 1979, MNRAS, 186, 145

White S. D. M., Frenk C. S., 1991, ApJ, 379, 52

White S. D. M., Navarro J. F., Evrard A. E., Frenk C. S., 1993, Nature, 366, 429

White S. D. M., 1996, in Cosmology and Large-Scale Structure, edited by R. Schaefer, J. Silk, M. Spiro, J. Zinn-Justin, Dordrecht: Elsevier, astro-ph/9410043

Wild V., Peacock J. A., Lahav O., et al. (the 2dFGRS team), 2005, MNRAS, 356, 247

Xu G., 1995, ApJS, 98, 355

Yang, X., Mo, H. J., van den Bosch, F. C., 2003, MNRAS, 339, 1057

York D. G., Adelman J., Anderson, J. E., et al. (the SDSS team), 2000, AJ, 120, 1579

Yoshida N., Stoehr F., Springel V., White S. D. M., 2002, MNRAS, 335, 762

Yu Q., Tremaine S., 2002, MNRAS, 335, 965

Zehavi I., Blanton M. R., Frieman J. A., et al. (the SDSS team), 2002, ApJ, 571, 172

Zucca E., Zamorani G., Vettolani G., et al. (ESP team), 1997, A&A, 326, 477